UNIVERSITÀ
DEGLI STUDI
DI PADOVA

Sede Amministrativa: Università degli Studi di Padova

Dipartimento di Fisica e Astronomia "Galileo Galilei"

SCUOLA DI DOTTORATO DI RICERCA IN: ASTRONOMIA
INDIRIZZO: UNICO
CICLO: XXVII

PHOTOMETRIC SEARCHES FOR EXOPLANETS AND VARIABILITY IN STAR CLUSTERS

Direttore della Scuola: Prof. Giampaolo Piotto

Supervisore: Prof. Giampaolo Piotto
Correlatore: Dr. Valerio Nascimbeni

Dottorando: Andrea Cunial

Contents

Abstract - English version

This thesis is focused on the photometric analysis of stellar light curves (LCs), to search for variable stars and transiting extrasolar planets. In particular, this study is carried out on crowded fields which include open clusters (OCs).

The context of my work is the photometric preparatory survey "The Asiago Pathfinder for HARPS-N" (APHN; PI: Bedin) aimed at characterising OCs (i.e. M44, NGC 752, M35, NGC 2158 and M67) to be observed with the High Accuracy Radial velocity Planet Searcher for the Northern hemisphere (HARPS-N), mounted at the Telescopio Nazionale Galileo (TNG). The APHN survey was also recently extended to an additional sample of OCs which were chosen as targets for the *Kepler* extended mission *K2*[1] (Howell et al. 2014), in view of creating astro-photometric master input catalogues for high-precision photometry of *Kepler* and *K2* data, following the method developed by (Libralato et al. 2015a).

We also analysed data coming from other ground-based facilities, such as the SuperWASP[2] or the STELLA1 Telescope[3].

Searches for transiting exoplanets within OCs, while challenging (van Saders & Gaudi 2011), are particularly useful to constrain the properties of both the host star and planet, and to unveil the planetary formation and evolution mechanisms (Janes 1996; Fischer & Valenti 2005).

The first part of the thesis reviews the different photometric techniques so far developed and present in the literature to search for exoplanets and, in general, for stellar variability studies (chapter 1). A short review of the principal ground and space-based projects is also given at the end of this chapter.

Chapter 2 describes the origin of systematics errors ("red noise") and gives a description of the methods developed to correct the LCs before the search for variability. A description of the different type of stellar variability and of the algorithms used to search for periodical signals is given in chapter 3.

My original analysis of the OCs data is described in the last four chapters, starting from M44 in chapter 4. There, after a description of the observational setup, I discuss the detrending algorithms, the procedure to detect periodic signal, and my results in terms of newly discovered variables, including a study of the gyrochronological period versus colour relation. The following chapters are organised in a similar way, but covering NGC 752 (chapter 5), M35 & NGC 2158 (chapter 6) and M67 (chapter 7), respectively.

[1] http://keplerscience.arc.nasa.gov/K2/
[2] http://www.superwasp.org/
[3] http://www.aip.de/en/research/facilities/stella/

Abstract - Italian version

Questa tesi è incentrata sull'analisi fotometrica delle curve di luce stellari (LCs), per ricercare stelle variabili e pianeti extrasolari in transito. In particolare, questo studio viene condotto su campi affollati che includono ammassi aperti.

Il contesto del mio lavoro è la mappatura fotometrica preparatoria "The Asiago Pathfinder for HARPS-N" (APHN; PI: Bedin), finalizzata alla caratterizzazione degli ammassi aperti (ad esempio M44, NGC 752, M35, NGC 2158 and M67), al fine di essere impiegata allo spettrografo HARPS-N (acronimo per *High Accuracy Radial velocity Planet Searcher for the Northern hemisphere*) installato al Telescopio Nazionale Galileo (TNG). Recentemente, la mappatura APHN è stata estesa ad un campionamento addizionale di ammassi aperti che sono stati scelti quali obiettivi per la missione *K2*[4], prolungamento della missione *Kepler* (Howell et al. 2014), allo scopo di creare un catalogo astro-fotometrico di base delle componenti che verranno analizzate con i set di dati delle missioni *Kepler* e *K2* (Libralato et al. 2015a).

Altre strumentazioni sono state coinvolte, come ad esempio quelle del progetto SuperWASP[5] oppure quelle del telescopio STELLA1[6], i cui dati sono stati analizzati in questa tesi.

Le ricerche di esopianeti in transito all'interno di ammassi aperti, benchè ardue (van Saders & Gaudi 2011), sono particolarmente utili per limitare le proprietà sia della stella ospitante, sia del pianeta e di svelare il meccanismo di formazione ed evoluzione planetaria (Janes 1996; Fischer & Valenti 2005).

La prima parte della tesi è una recensione delle differenti tecniche fotometriche adottate dalla comunità scientifica nella ricerca di esopianeti e, più in generale, della variabilità stellare (capitolo 1), focalizzandosi sulle mappature fotometriche degli ammassi aperti. Una breve recensione sui principali progetti da terra e da spazio viene data alla fine di questo capitolo.

Il capitolo 2 analizza le cause degli errori sistematici ("red noise") e descrive i metodi sviluppati per correggere le curve di luce prima della ricerca di variabilità. Una descrizione delle differenti tipologie di variabilità stellare e degli algoritmi usati per la ricerca di segnali periodici viene data nel capitolo 3.

La mia analisi degli ammassi aperti sopra citati è descritta negli ultimi quattro capitoli, partendo da M44 nel capitolo 4. Qui, dopo una descrizione delle attrezzature per le osservazioni, tratto degli algoritmi per la correzione da errori sistematici, della procedura per individuare segnali periodici e dei miei risultati in termini di variabili appena scoperte, includendo uno studio della relazione girocronologica fra la periodicità e il colore della stella. I capitoli seguenti sono organizzati in maniera simile, ma trattano, rispettivamente, di NGC 752 (capitolo 5), di M35 & NGC 2158 (capitolo 6) e di M67 (capitolo 7).

[4]http://keplerscience.arc.nasa.gov/K2/
[5]http://www.superwasp.org/
[6]http://www.aip.de/en/research/facilities/stella/

Chapter 1

Introduction and thesis overview

The search for exoplanets is a recent and rapidly evolving research field, with enormous potentialities, also thanks the huge amount of developed projects, and the consequent investment in terms of both human and technological resources. Officially, the first exoplanets was announced in 1995 by Mayor & Queloz (1995). It was quite an unusual object (today we call it an "hot Jupiter"): a Jupiter mass planet, orbiting around the star 51 Peg with a very short period. Since the beginning of the fascinating adventure, it was clear the Solar System planets can not be consider as a typical example of planets. 51 Peg b was discovered with the so called radial velocity (RV) method, which soon became one of the best available techniques to discover exoplanets, potentially able to discover planets with masses close to Earth mass.

Though the discovery of 51 Peg b can be considered as a sort of starting point of this research field, it was not really the first exoplanet discovered. We must at least mention the discovery of HD 114762 b by Latham et al., again using the RV technique, in 1989, though, at that time the object was considered as a brown dwarf, and the planetary system around the pulsar PSR 1257+12 pulsar (Wolszczan & Frail 1992), identified with the so called pulsar timing methods (see below).

Since then, many different observational approaches have been developed for the search of exoplanets, and many both ground and space-based instruments have been built, and are presently running.

In the following, we will describe the main exoplanet search methods and some of the most relevant projects and instruments.

1.1 Methods for exoplanet search

In the following, I will describe the main methods that are used to search for exoplanets.

As this thesis is based on photometric analysis of light curves, I will first describe (1.1.1) the techniques based on the analysis of photometric sequences.

1.1.1 Light curves and planetary research

The methods based on photometry are:

- Transits;
- Transit Time Variations (TTV) and Transit Duration Variations (TDV);

- Pulsar timing;
- Gravitational lensing.

Planetary transits

Already proposed by Struve (1952), this method has produced the highest number of planets and candidate planets available so far. The method is based on the dimming of the stellar light curve when a planet crosses the stellar disk (Perryman 2000).

Once the hosting star radius is known, the transit allows to measure the planet radius. Transit parameters also allow to measure the inclination of the orbit and its period. The radius of the planet (R_p) is obtainable using the percentage of the flux dimming, knowing the radius of the star ($R_\star$) from evolutionary models, following this expression (Doyle 2008):

$$\frac{\triangle L}{L} \propto \left(\frac{R_p}{R_\star}\right)^2 \tag{1.1}$$

From the observations of more that one transit, it is possible to evaluate the period of the planetary orbit (P). Knowing also the star mass ($M_\star$, from spectral type or from models), it is possible to define the semimajor axis (a_p) of the orbit, using the 3$^{\rm rd}$ Kepler's law:

$$\left(\frac{P}{yr}\right) = \left(\frac{a_p}{1\mathrm{AU}}\right)^{3/2} \left(\frac{M_\star}{M_\odot}\right)^{-1/2} \tag{1.2}$$

where $M_\odot$ is the mass of the Sun. Using the transit duration ($\triangle T_{tran}$), it is possible to estimate the inclination of the orbit with respect to the line of sight of the observer. In fact, we have (Deeg 1998; Perryman 2000):

$$\triangle T_{tran} = \frac{P}{\pi}\left(\frac{R_\star \cos\delta + R_p}{a}\right) \simeq 13 \left(\frac{M_\star}{M_\odot}\right)^{-1/2} \left(\frac{1}{1AU}\right)^{1/2} \left(\frac{R_\star}{R_\odot}\right) hours \tag{1.3}$$

where δ is the latitude of the planetary transit on the stellar disk and $\triangle T_{tran}$ is expressed in hours. Knowing all the other parameters in 1.3, we can calculate the latitude δ, and, from it, to obtain the orbital inclination (i_p) from the following equation (Perryman 2000):

$$\cos i_p = \frac{R_\star \sin\delta}{a_p} \tag{1.4}$$

using the convention that $i_p = 90^\circ$ when the orbit is prograde and the orbital plane is "edge-on" with respect to the observer.

The possibility to observe a planet in transit is given by the geometry of the orbit and by the orientation of the planetary system with respect to the observer line of sight (Brown 2008). Of course, the orbital plane has to be (almost) edge-on. In order to have a transit, the further the planet orbital plane is from edge-on configuration, the closer the planet has to be to its hosting star (i.e. short period, or in a equivalent way, small orbit semi-major axis).

The probability to observe a planet in transit is given by the following equation (Perryman 2000):

$$p = \frac{R_\star}{a_p} = \cos(i_{\min}) \tag{1.5}$$

where $i_{\min}$ is the minimum inclination with respect to the observer that the orbital plane can have to generate a transit. In other words, to observe a planet in transit, the following relation must be satisfied (Brown 2008):

$$a\cos(i_{min}) \leq (R_p + R_\star) \tag{1.6}$$

The measurement of planetary transit parameters are be affected by many observational errors. For example, in ground-based observatory, the presence of the Earth atmosphere creates scintillation or stellar flux extinction. Also the stellar limb-darkening or intrinsic stellar variability can affect the evaluation of the instants of the beginning and end of a transit event. Most of these uncertainties can be accounted for during the analysis of the light curve.

At 29/01/2016, the number of planets discovered with planetary transit observations are 1285[1]. Many of these were discovered by Kepler mission (Borucki et al. 2010; Koch et al. 2010).

Transit Time Variations (TTV) and Transit Duration Variations (TDV)

Exoplanet transits allow the measurement of the timing (ingress, egress, etc.) of the transit. Transit Time Variation (TTV; Holman & Murray 2005; Agol et al. 2005) is a potentially powerful technique, to identify the presence of perturbers of the orbit of the transiting planet. Collecting many transits of the same planet, this technique verifies the regularity in the transit frequency. In principle, the presence of other planets (not necessarily transiting, but members of the same planetary system) could influence the transiting timing. In this case, the transiting planet should not pass through the stellar disk at regular intervals, varying the measured transit timings, with respect to the expected Keplerian orbit (Holman & Murray 2005). The TTV can be used to set masses and orbit parameters of the perturbing planet(s). Holman & Murray (2005) defined the typical variation of the interval between a transit and the following one, computing the integration of Lagrange's equations of planetary motion (Murray & Dermott 1999). The timing variation can be described by the following equation (Holman & Murray 2005):

$$\Delta t \simeq \frac{45\pi}{16}\left(\frac{M_2}{M_\star}\right) P_1 \alpha_e^3 \left(1 - \sqrt{2}\alpha_e^{3/2}\right)^{-2} \tag{1.7}$$

where M_2 and $M_\star$ are the masses of the second planet not in transit and of the parent star, respectively, P_1 is the orbital period of the transiting planet, and $\alpha_e = \{(a_1)\,/\,[a_2 \cdot (1 - e_2)]\}$, where a_1 and a_2 (with $a_2 > a_1$) are the semimajor axis of the orbits of transiting planet and of the planet not in transit, respectively, and e_2 the eccentricity of the perturber planet orbit. The value of e_2 could be evaluated using the relative magnitudes of the variations $\Delta t_{max}/\Delta t_{min}$ (Holman & Murray 2005). Considering the period of the perturber planet much greater than the period of the transiting planet, the factor α_e can be ignored. In this way, from equation 1.7 it is possible to obtain the value of the mass of the perturber planet (Holman & Murray 2005):

$$M_2 \simeq \frac{16}{45\pi} M_\star \frac{\Delta t_{max}}{P_1}\left(\frac{P_2}{P_1}\right)^2 (1 - e_2)^3 \tag{1.8}$$

where P_2 is the period of the perturber planet orbit.

As we can see, the further the transiting planet is from the parent star (or the smaller the parent star mass), the higher the probability is to detect the perturber planet.

Another technique that can be used when we have a transiting planet is the Transit Duration Variation (TDV; Kipping 2009). In this case we need to monitor the time interval between the

[1] http://exoplanet.eu/catalog/?f=%22transit%22+IN+detection

beginning and the end of a transit. The basic idea is that the transiting planet orbital period could be gravitationally affected by an exomoon (Kipping 2009).

At 29/01/2016, five exoplanets have been discovered with the TTV indirect method[2]. No TDV detection is present in the literature.

Pulsar timing

This technique takes into account the light curves of pulsating variable stars. This kind of stars have a periodical signal, which is constant when the star is unperturbed. If there is a planet orbiting around this kind of variable, the pulsating star also have an orbit around the barycentre star-planet. In such case, the light, that comes from the star, has to travel different distances from the observer. For this reason, the flux pulse from the star can be either anticipated or delayed with respect to the normal periodicity. The signal delay is maximum when the planet is in inferior conjunction, whereas the signal is in maximum advance when the planet is in superior conjunction. The amplitude between the advance and the delay of the signal impulse from the star is given by the following equation (Doyle 2008):

$$\tau = \sin i \frac{d_p}{c} \frac{M_p}{M_\star} \tag{1.9}$$

where d_p is the distance of the planet from the system barycentre, M_p and $M_\star$ are the planet and the star masses respectively, c the light velocity and i the inclination of the planet orbit (that is 90°, with the usual convention that the plane is "edge-on" respect to the observer).

This method is very powerful and allows detection of Earth size planets. This is the consequence of the extreme precision in the periodicity of the flux signal of this kind of variable stars. But the scientific interest on this method is quite low, because the parent stars are very different from a Solar type star and planets orbiting around these stars are obviously inhospitable to life.

At 29/01/2016, the number of planets discovered with pulsar timing variations are 23[3].

Gravitational lensing

Gravitational lensing allows to discover exoplanets taking advantage of the deflection of light by massive objects, as predicted by general relativity laws. These relativistic effects happen when a star hosting planets transits in front of a field star. When the transit happens, the light of the field star is magnified. If there is a planet orbiting around the transiting (foreground) star, and also this planet transits in front of the background star, an additional magnification happens. The magnification is characterised by a factor $Q(t)$, given by the following expression (Doyle 2008):

$$Q(t) = \frac{u^2(t) + 2}{u(t)(u^2(t) + 4)^{1/2}} \tag{1.10}$$

where $u(t)$ is the projected distance between the "lens" star or the "lens" planet and the field star of which the flux is magnified. The value $u(t)$ is expressed in Einstein radii (R_E; Perryman 2000), which in turn are expressed in Astronomical Units (AU):

$$R_E = \left[\frac{4GM_L}{c^2}\frac{(D_S - D_L)D_L}{D_S}\right]^{1/2} = 8.1\left(\frac{M_L}{M_\odot}\right)^{1/2}\left(\frac{D_S}{8kpc}\right)^{1/2}[(1-d)d]^{1/2}\text{AU} \tag{1.11}$$

where D_L and D_S are the distances (in kpc) of the lensing image from gravitational lens and from the source, respectively, whereas $d = D_L/D_S$ is the distances ratio. If the planet that

[2]http://exoplanet.eu/catalog/?f=%22TTV%22+IN+detection

[3]http://exoplanet.eu/catalog/?f=%22pulsar%22+IN+detection

orbits around the "lens" star transits in front of the star, the magnification created by the planet could be up to 5% higher than the magnification due to the parent star. The probability that the planet orbiting around a "lens" star transits in front of the field star is equal to 1 : 5 (Doyle 2008). The duration of the microlensing event due to the planet is given by (Doyle 2008):

$$t_E = \sqrt{\frac{4GM_p dV}{c^2}} \tag{1.12}$$

where d is the distance (in parsecs) of the "lens" star from the observer and V is the orbital velocity of the planet.

This method is of particular interest for extended surveys of large field of views (large number of stars). The OGLE survey (Udalski et al. 1992) e MOA (Hearnshaw et al. 2006) represent an example of this kind of surveys. The main limit of this method is the lack of repetitiveness of the events, and the difficulties to characterise the source of the lens effect.

The first planet discovered with this method was OGLE235-MOA53 b (Bond et al. 2004). At 29/01/2016, the number of planets discovered with this method is 43[4].

1.1.2 Other methods for planetary research

In addition to the photometric methods, based on light curves analysis for the discovery of new extrasolar planets, there are methods based on the motion of the hosting star induced by the presence of a planet, in particular spectroscopic observations for the measurement of the radial velocity change of the hosting star along the line of sight, or the astrometric method, searching for the motion of the hosting star projected on the sky. Direct imaging of exoplanets has also been developed, and, in practice, this represents the only one direct method for the extrasolar planet discovery. There are other secondary methods used to detect the extrasolar planets, but at the moment none planet was discovered with these. In the following sections, I am going to explain only the three methods above mentioned:

- Radial velocity;
- Astrometry;
- Direct imaging.

Radial velocity

The radial velocity was one of the first indirect methods used for the search for extrasolar planets. This method, based on spectroscopic observations, measures the motion along the line of sight of the parent star around the barycentre of the star-planet system. The RV variation (K) is given by the following equation (Perryman 2000; Doyle 2008):

$$K = \left(\frac{2\pi G}{P}\right)^{1/3} \cdot \frac{M_p \sin i}{(M_p + M_\star)^{2/3}} \cdot \frac{1}{(1-e^2)^{1/2}} \tag{1.13}$$

where P is the orbital period of the planet, M_p and $M_\star$ the masses of the planet and of the star, respectively, $M_p \sin i$ is the minimum mass of the planet and e and i are the eccentricity and the inclination of the orbit of the planet. Using the measurements of the spectral line shifts, it is possible to define the eccentricity and the period of the orbit. Knowing the star mass from models and the amplitude K of the orbital velocity variation from spectral observations, it is

[4] http://exoplanet.eu/catalog/?f=%22microlensing%22+IN+detection

possible to define the minimum mass of the planet, being the inclination of the planetary orbit plane unknown (from the spectroscopic observations). Once the orbit inclination is measured (for example using planetary transit method, see section 1.1.1), the real mass of the planet is defined. Most importantly, transit observations also provide the planet radius (see section 1.1.1), and therefore for a transit planet also identified with the RV method we have the mean density. In general, following the 3rd Kepler's law (1.2), knowing the period of the orbit and the mass of the star, the semi-major axis of the orbit can be defined.

Mainly because of the effects of stellar activity, the RV method can not be more accurate than 1 m/s (Doyle 2008). This limit prevents the identification of an Earth-like planet, orbiting around a Sun-like star in habitable zone, at least around active stars. Indeed, the radial velocity variation induced on a Sun-like star by an Earth mass planet at 1 AU is 0.09 cm/s. A Jovian planet is easier to detect: for example, the RV variation induced by Jupiter on the Sun is 13 m/s. Recently, with second-generation spectrographs, such as HARPS-N that reaches measurement precision of 0.3 m/s (Cosentino et al. 2014), new observation strategies (which accounts for the activity effects) and new reduction methods allow us to reduce the intrinsic stellar activity effects on radial velocity measurements (Dumusque et al. 2015), and Earth-size planets are in principle becoming detectable also with the radial velocity method.

At 29/01/2016, the planets discovered with the method of the radial velocity are 632[5].

Astrometry

Astrometry is based on imaging of the target star for an extended temporal interval for the measurement of proper motions. Once natural proper motion of the star and parallax effect are removed, any residual motion is due to the is gravitational affected by other bodies, like orbiting planets. In this case, the residual motion is an elliptical orbit of the star around the barycentre of the star-planet system. The ellipse of the star motion around the barycentre is described, in arcseconds, by the following equation (Doyle 2008):

$$\alpha = \frac{M_p}{M_\star}\frac{a_p}{d} \tag{1.14}$$

where d is the distance of the observer from the planetary system in parsecs, whereas a_p is the semimajor axis of the planetary orbit in Astronomical Units (AU).

At 29/01/2016, with this method, only 1 planet was discovered[6] (HD 176051 b; Muterspaugh et al. 2010). This paucity of planetary discoveries is due to the required high precision measurements in astrometry, very difficult with ground-based observatories, due to atmosphere presence. But GAIA mission (de Bruijne 2012) and other spaced astrometric observations shall overcome this problem. In effect, around FGK stars ∼20000 planets are expected, with 25-40 planets in transit (Perryman et al. 2014), whereas around M stars ∼10 transiting systems are expected (Sozzetti 2013).

Direct Imaging

The direct imaging is a method of search for extrasolar planets that can be applied only in particular cases. The method is limited by the parent star luminosity flux. The amount of flux from the planet depends on different parameters, such as the distance of the planet from the parent star, the size of the planetary disk, and the nature of the planet atmosphere, that influences the geometrical albedo of the planet. Hot planets can emit flux in the near infrared.

[5]http://exoplanet.eu/catalog/?f=%22radial%22+IN+detection
[6]http://exoplanet.eu/catalog/?f=%22astrometry%22+IN+detection

In the optical bands, the ratio between the luminosity flux of the parent star and the reflected luminosity flux of the planet is very important to define the possibility to directly image the planet. This luminosity ratio is given by the following equation (Doyle 2008):

$$\frac{L_p}{L_\star} = A \cdot p(\varphi(t)) \left(\frac{R_p}{a_p}\right)^2 \tag{1.15}$$

where A is the geometrical albedo of the planet, $p(\varphi(t))$ is the function of the orbital phase, that defines the quantity of the reflected stellar luminosity according to the geometry of the system, R_p and a_p are the radius and the orbit semimajor axis of the planet. The higher the luminosity ratio is in the equation 1.15, the higher the possibility is to detect the planet with a direct imaging observation.

In addition to the direct imaging in visual band, it is possible to directly observe the planet in infrared band. In fact, in the case of a warm or hot planets, in addition to the reflected component of the light, there is a intrinsic component emitted by the planet itself in the thermal infrared band. In this way, the ratio of equation 1.15 will be higher, increasing the possibility to directly detect the planet.

The first planet detected with direct imaging was 2M1207 b (Chauvin et al. 2004). This discovery shows that the method is good mainly for planets distant from the parent star ($a_p = 46 \pm 5$AU at the distance of 52.4 ± 1.1pc from the Sun; Song et al. 2006), with an elevated mass ($M_p = 4 \pm 1 M_J$; Ducourant et al. 2008), orbiting around a small star (a M8 spectral type star with a mass of $\sim 25 M_J$; Chauvin et al. 2004).

At 29/01/2016, with the direct imaging, 65 planets were discovered[7].

1.2 Search for planetary systems: the projects

In the last 20 years or so, an increasing number of projects, specifically dedicated to the search for exoplanets, were developed. In the following, I describe a few of the most productive on them, though my list can not be considered as a complete overview of the ongoing efforts. My presentation will first present some ground-based programs, and then will describe space-based projects.

1.2.1 Ground-based projects

Ground-based programs are mainly using small telescopes for large field surveys of bright stars. In this way, a high number of stars can be photometrically followed, in order to detect intrinsic activity or transiting phenomena. These programs need the support of larger facilities for follow-up observations (for planet candidate confirmation).

SuperWASP

The *Super Wide Angle Search for Planets*[8] (SuperWASP; Pollacco et al. 2006; Butters et al. 2010) is a international collaboration which uses two different facilities, one in northern hemisphere, one in southern hemisphere. The northern observatory is located in La Palma Isle, at Roque de los Muchachos Observatory. The southern observatory is located in South Africa, at the South African Astronomical Observatory (SAAO). The observations are carried out with

[7] http://exoplanet.eu/catalog/?f=%22imaging%22+IN+detection
[8] http://www.superwasp.org/

robotic facilities. There are eight wide-field cameras deployed on equatorial mount. The cameras are arranged into a 2×4 arrays. Each camera has a CCD detector manufactured by Andor Technology. It consists of 2048×2048 pixels, each 13.5 μm in size (Pollacco et al. 2006). Each camera use a Canon 200 mm, f/1.8 telephoto lens. The angular resolution is 13.7"pixel^{-1}, with a field of view of $\sim$64 deg^{-1} for each camera. The total field of view of one single camera sets is $\sim$482 deg^{-1} (Pollacco et al. 2006).

The first light was at the SuperWASP-N observatory at Roque de los Muchachos, on the 2004, May 2$^{\rm nd}$. The southern observatory has the first light on the 2006, February 13$^{\rm th}$ (Butters et al. 2010). During 2004 SuperWASP-N worked unfiltered, whereas, since 2006 on, both observatories worked with a visual broadband filter, with a pass-band from 400 to 700 nm (Butters et al. 2010). The observation strategy is to point 6-8 fields per night, at similar declination and displaced by one hour in right ascension. Each field is sampled by the telescope every 9-12 minutes, with 30sec exposure time per image (Butters et al. 2010).

Several planets were discovered by SuperWASP. More than 100 planets, between discoveries and follow-ups, are tied to this project, with 2 multiple systems.

HATNet and HATSouth

The *Hungarian Automated Telescope Network*[9] (HATNet; Bakos et al. 2004, 2007) is a network of six identical small telescopes, four in Fred Lawrence Whipple Observatory (FLWO) at Mount Hopkins in Arizona, USA, and two in Mauna Kea Observatory in Hawaii, USA (Bakos et al. 2009). Each telescope is a 11cm diameter f/1.8 Canon lens. Starting the observations between 2003 and 2005 (Bakos et al. 2004), initially the telescopes had 2K×2K front-illuminated Apogee AP10 CCD, with resolution of 14"pixel^{-1} and a field of view of 8° × 8°. Cousin I-band filters were used (Bakos et al. 2009). From 2007, new Apogee U16m 4K×4K detectors were installed at all telescopes. These CCDs have a resolution of 9"pixel^{-1} and a field of view of 10.6° × 10.6°. Sloan r filters were used (Bakos et al. 2009).

Only one field is covered for each observation set, followed from sun-set to dawn, with a short cadence photometric series of 5-minutes exposures (Bakos et al. 2009).

A seventh telescope, named TopHAT, installed in Fred Lawrence Whipple Observatory (FLWO), is used for photometric follow-ups (Bakos et al. 2009). An eighth telescope, very similar to the other six telescopes in Arizona and in Hawaii, is located at Wise Observatory, Israel.

The planets discovered by HATNet project are 56.

A similar project was created in southern hemisphere, named *Hungarian Automated Telescope Network-South*[10] (HATSouth; Mancini 2013). This project uses other six identical, fully automated wide field telescopes, located at three sites (Chile: Las Campanas, Australia: Siding Springs, and Namibia: HESS site). There are two telescopes per site. Each telescope has four 0.18m f/2.8 Takahashi hyperbolic astrographs, with Apogee U16m 4K×4K detectors per each astrograph. Each astrograph spans a field of view of 4° × 4°, with a resolution of 3.7"pixel^{-1}. Sloan r filters were used (Mancini 2013).

This second project, started in 2013, already collected 15 new detected planet.

HARPS and HARPS-N

The *High Accuracy Radial velocity Planetary Search*[11] (HARPS; Pepe et al. 2002; Mayor et al. 2003) is a high resolution spectrograph, managed by Geneva Observatory, specifically developed for the search for extrasolar planets, using the radial velocity method. A fibre-fed, cross-dispersed

[9] http://hatnet.org/
[10] http://hatsouth.org/
[11] http://obswww.unige.ch/Instruments/HARPS/Welcome.html

echelle spectrograph is used (Mayor et al. 2003), named HARPS. The covered spectral range is between 380 nm and 690 nm, with a spectral resolution of 115000 (Mayor et al. 2003). The first spectrograph was mounted at the ESO's 3.6m telescope at La Silla Observatory, in Chile. This spectrograph, during measurements of radial velocity, can reach a precision less than 1 m/s (Mayor et al. 2003). At the precision level, the observed spectrum is dominated by stellar "noise" created by mode amplitudes of oscillation at the stellar surface (see section 1.1.2). Depending on the kind of observation strategy applied, this stellar "noise" can be attenuated (e.g. extending the exposure time, in order to avoid mode amplitude periods of the stellar surface).

The HARPS spectrograph became operative on 2003, October 1st (Mayor et al. 2003). HARPS allowed the discovery of sub-Neptune or super-Earth planets (e.g. Díaz et al. 2015; Mortier et al. 2015). Two planets in two different open clusters (OCs) were discovered using HARPS spectrograph (Lovis & Mayor 2007), together with Coralie spectrograph (another spectrograph dedicated to the search for extrasolar planets with radial velocity method; Queloz et al. 2000) at the Swiss-1.2m Euler telescope at La Silla Observatory. After this work, Brucalassi et al. (2014) identified 3 planets inside the OC M67, using data obtained by Lovis & Mayor (2007) with Coralie spectrograph (Queloz et al. 2000) and observing the OC targets with HARPS, together with SOPHIE spectrograph, mounted at the OHP 1.93m telescope (Bouchy & Sophie Team 2006), and HRS spectrograph, mounted at the Hobby Eberly Telescope (Tull 1998) (see section 1.2.3).

After the success of HARPS, a second instrument named *High Accuracy Radial velocity Planetary Search for the Northern hemisphere*[12] (HARPS-N; Cosentino et al. 2012) was conceived. Based on the design of HARPS at the ESO's 3.6m telescope, HARPS-N is mounted at the Telescopio Nazionale Galileo (TNG), at Roque de los Muchachos Observatory, in Canaries La Palma Island. It is a fiber-fed, cross-dispersed echelle spectrograph and, thanks to the ultra-stable environment, in a temperature-controlled vacuum chamber, high precision in radial velocity measurements can be reached with HARPS-N, keeping the RV error below 1m/s. In this way, with HARPS-N rocky, Earth-like planets can be detected, too. As for HARPS, also for HARPS-N the stellar "noise" created by mode amplitudes on the stellar surface can be attenuated (Dumusque et al. 2015).

HARPS-N spectrograph became operative on April 2012 (Cosentino et al. 2012). Since its first light, HARPS-N was used for the *Global Architecture of Planetary Systems* programme[13] (GAPS; Covino et al. 2013). The principal aim of this programme is the characterisation of the architecture of planetary systems as function of the parent star properties (mass, metallicity) and of the environment in which the planetary system is located. Different planets were characterised in follow-ups (mainly of Kepler and K2 planet candidates) or were discovered. In particular, considering OC environment, Malavolta et al. (2016) discovered the second planet of the first multiple planetary system in the OC M44.

OGLE and MOA

The *Optical Gravitational Lensing Experiment*[14] (OGLE Udalski, Szymański & Szymański 2015) is a long-term project, devoted to create a large-scale photometric sky survey focused on sky variability. The project, managed by University of Warsaw, is presently running in its forth phase. In the first phase, it used the non dedicated 1.0-m Swope telescope at Las Campanas Observatory, in Chile. In this phase, first microlensing events and several variables were discovered (e.g. Udalski et al. 1993, 1994). In the second phase, a dedicated telescope was installed at Las Campanas

[12] https://plone.unige.ch/HARPS-N
[13] http://www.oact.inaf.it/exoit/EXO-IT/Projects/Entries/2011/12/27_GAPS.html
[14] http://ogle.astrouw.edu.pl/

Observatory: the 1.3m Warsaw telescope, a f/9.2 Ritchey-Crétien telescope with three-lens field corrector with a 1.5 degree diameter field of view (Udalski, Szymański & Szymański 2015), had the first light on 1996, February 9$^{\text{th}}$. The second phase of OGLE stared on January 1997 and ended on December 2000. In this phase, the number of microlensing phenomena and, in general, variables exponentially increased. The first OGLE maps of non-variable stars (Udalski et al. 1998) was also created. The third phase started on 2001, June 12$^{\text{th}}$, with a new eight detector mosaic camera installed on Warsaw telescope. In this phase, the first extrasolar planet was discovered with both transit and microlensing techniques (Bond et al. 2004). The largest sample of variables was created (Soszyński et al. 2014, and references inside). After 2009, the forth phase started with the installation of 32 science grade CCDs of 2048×4102 pixel size mosaic, that fills the entire 1.5 square diameter field of view of the Warsaw telescope (Udalski, Szymański & Szymański 2015).

Nowadays, 31 planets were discovered by OGLE; 2 planetary systems with multiple planets: 23 planets were detected with microlensing, whereas 8 planets were detected with the planetary transit technique.

With similar goals as the OGLE project, the *Microlensing Observations in Astrophysics*[15] (MOA Bond et al. 2001; Sumi et al. 2003) is a programme born by a collaboration between New Zealand and Japan. It had a progression in two different phases. In the first one, from 1995 to 2002, the facilities used was a modified 0.6-m Boller & Chivens telescope at the Mt John University Observatory, in New Zealand. This telescope has a f/6.25 Cassegrain focus, with a field of view of $1.3^\circ \times 1.3^\circ$ (Sako et al. 2008). Until 1998, the camera was a nine-CCD mosaic camera (MOA-cam1), each chip having 1k×1k pixels. Since 1998, the mounted camera became MOA-cam2 which consists of three 2k×4k CCD SITe ST-002A chips (Sako et al. 2008). In 2002, a dedicated 1.8m telescope at My John University Observatory was installed (Hearnshaw et al. 2006; Sako et al. 2008). At this telescope, with f/3 prime focus and a field of view of $2.18^\circ \times 2.18^\circ$ (Hearnshaw et al. 2006), a ten-CCD mosaic with a 0.57"pixel^{-1} of scale at focal plane was installed.

The MOA programme discovered 19 planets, all based on microlensing. Other 2 planets were discovered in parallel with the OGLE programme.

1.2.2 Space-based projects

The presence of atmosphere could limit the precision in measurements from ground-based facilities. A substantial improvement is achievable with space-based observatories.

Some examples of space-based projects are explained in the following section.

CoRoT

The *COnvection ROtation and planetary Transits*[16] (CoRoT; Auvergne et al. 2009) was a space mission supported by the French Space Agency (CNES) in conjunction with the European Space Agency (ESA) and other international partners. The principal aims were the asteroseismology and the search for extrasolar planets using photometric observations.

CoRoT was launched in December 2006 and on 2007, January 18$^{\text{th}}$ there was the first light. COROT used an afocal 27cm telescope with a wide field of view ($2.7^\circ \times 3.05^\circ$). The mission was scheduled to end after 2.5 years, but it was prolonged until 2014, June 17$^{\text{th}}$ (Moutou & Deleuil 2015). During the mission, CoRoT maintained a circular polar orbit, at an height of 900 km.

[15] http://www.phys.canterbury.ac.nz/moa/
[16] https://corot.cnes.fr/en/COROT/index.htm

The strategy of the mission was to observe the same field non-stop, for a maximum of 150 days, limited by the Earth orbit around the Sun. The planets discovered by CoRoT programme are 32: 31 planets were detected with planetary transit technique, one was detected with a radial velocity follow-up (Queloz et al. 2009). Two planetary systems are multiple. With this mission, the first two rocky planets, orbiting a main sequence star, were discovered (CoRoT-7 b and c; Léger et al. 2009; Queloz et al. 2009).

Kepler

Kepler[17] mission (Borucki et al. 2004, 2010; Koch et al. 2010; Brown et al. 2011) was the most fruitful project for the search for extrasolar planets. The mission was designed and realised by NASA agency (Borucki et al. 2004). Principal aim was to define the frequency of rocky planets in Habitable Zone, orbiting Solar-like stars, and the terrestrial planet frequency in planetary systems (Borucki et al. 2008, 2010), defining orbital and physical properties. Asteroseismology was also an important by-product of Kepler, in particular for dwarf stars. In general, statistical issues on the architecture and frequency of multiple planetary systems was approached.

The spacecraft was launched on 2009, March 6^{th}, starting science operation on 2009, May 13^{th} (Koch et al. 2010). The final position of the spacecraft was in a heliocentric orbit, at 1 AU from the Sun, following the Earth with an orbit of 372.5 days. The telescope on board is a 0.95cm Schmidt. The focal plane allocates 42 CCDs in a mosaic arrangement. Each CCD has a 2200×1024 pixels, with a resolution of 4"pixel^{-1}. The total field of view of this detector mosaic is 105 deg^2.

The strategy of the project was to photometrically monitor the same field for all the duration of the mission, nominally for 3.5 years (Borucki et al. 2008), but extended until May 2013, when failures of the second of the four reaction wheels, essential to maintain the telescope pointing, happened. Hundreds of thousands of stars were monitored during the mission, using short-cadence photometry technique. Very stable photometry was necessary to detect Earth-like planets, at 1 AU from Sun-like star. The observations had to reach very low errors in differential photometry, in order to detect typical Earth-like planet transit, which produces a light curve dimming of 84 parts per million (ppm) (Koch et al. 2010). To confirm the detection of an Earth like transiting planet, at least 3 years and half were necessary, because at least 3 transits are necessary, also to describe planetary orbit.

The sky field in Cygnus-Lyra region was chosen because just above Galactic plane. The region includes a large sample of dwarf stars. In addition, this region could be continuously observed along the year. According to the official data of the mission website, 1030 planets were discovered and confirmed in more than 440 planetary systems, mostly with planetary transit method. Some planets were discovered with the technique of TTV. Moreover 2165 eclipsing binaries were discovered and 4696 candidates planets are waiting to be confirmed.

Kepler-66 b and Kepler-67 b (Meibom & Kepler Team 2013, see table 1.1) are the only confirmed extrasolar planets discovered in OC with the planetary transit technique.

K2

After the failure of Kepler second reaction wheel, the project had to develop a new observing strategy, because the stable pointing of the Cygnus-Lyra field became impossible. NASA scientists chose to continue to make photometric series, changing the targets of the mission. Despite the problem with the reaction wheels, tests proved that photometric performances would remain better than what obtainable with ground-based observatories.

[17] See http://kepler.nasa.gov/

K2[18] phase (Howell et al. 2014) is the "second life" of Kepler mission. In this phase, the principal aim became the creation of photometric surveys of different fields around the ecliptic plane. Different observing campaigns were developed. Each campaign consists in approximately 75 days of non-stop observations of the same field of view. Like Kepler, the K2 mission provides long-baseline, high-cadence, high-precision photometry, for stars in a large field of view (same size of the original Kepler field).

At the moment, 13 campaigns are programmed: the observation of the eighth campaign were completed in January 2016. Other 5 campaigns are proposed for the future (period 2017 - 2018). This project had already observed different OCs (such as M35, NGC2158, Pleiades, Hyades, M44, M67 and Ruprecht 147) and other ones will be observed in the future.

So far, the discovered and confirmed planets by K2 phase are 28. Hundreds of candidates are waiting to be confirmed.

TESS

The *Transiting Exoplanet Survey Satellite*[19] (TESS; Ricker et al. 2014) will be the future NASA space mission, oriented to the search for exoplanets. In particular, through photometric observations, the space-based observatory will have, as principal aim, to monitor at least 200,000 main-sequence dwarf stars with a magnitude of $I_C \leq 13$ for temporary drops in brightness caused by planetary transits (Ricker et al. 2014). It will be an all-sky survey mission, in order to search for planets transiting bright and nearby stars, that are nearly evenly distributed over the entire sky (Ricker et al. 2014). The choice to monitor especially bright stars is due to the correlated goal of characterise the planets and their atmosphere. The brightest stars are exactly the targets that could be aim of spectroscopic and photometric follow-up with other facilities, such as the future *James Webb Space Telescope* (JWST).

The spacecraft will be launched in 2017 and will reach the final position into a highly elliptical 13.7-day orbit around the Earth (Ricker et al. 2014). Here, the observation strategy will be concentrated on main-sequence dwarfs with spectral types F5 to M5.

The telescope will be constituted by 4 cameras, that will be lenses in a f/1.4 custom design, with aperture of 10.5cm and a CCD detector with a $24° \times 24°$ unvignetted image. The created mosaic will be a 1×4 array of CCD fields of view (FoVs), otherwise a total of $24° \times 96°$ FoV ($\sim$400 times the FoV of Kepler). The observation strategy will be to orient the mosaic FoV along the ecliptic longitudes, from 6° in ecliptic latitude (both north and south) to the ecliptic pole. Both the hemispheres will be shared into 13 partially overlapping pointings. Each pointing will be constantly followed for at least 27 days. Considering the scheduled mission duration of 2 years, after accomplishing all the 26 pointings, close to the ecliptic poles, approximately 2800 square degrees will be observed for more than 80 days. Surrounding the ecliptic poles, approximately 900 square degrees will be observed for more than 300 days: these will be the two region that the JWST could observe at any time. Two different observation methods will be applied: a 2 minute cadence photometric series for the 200000 preselected bright stars and a 30 minute cadence photometric series for full frame observations, in order to discover new transiting planets around fainter stars. A pass-band from 600 to 1000 nm will be used.

After simulations, TESS is expected to find thousands of planets smaller than Neptune, including hundreds of super-Earths (1.25 - 2 $R_\oplus$) and tens of planets comparable in size to Earth (Ricker et al. 2014).

[18] http://keplerscience.arc.nasa.gov/
[19] http://tess.gsfc.nasa.gov/

CHEOPS

The *CHaracterising ExOPlanet Satellite*[20] (CHEOPS; Broeg et al. 2013; Fortier et al. 2014) will be the future European Space Agency (ESA) mission, oriented to measure transits of exoplanets. In particular, the principal aim of the project is to monitor a preselected list of bright and nearby stars, in order to characterise the structure of hosted exoplanets smaller than Saturn (Fortier et al. 2014). The targets of CHEOPS will be mainly two: (very) bright stars with a known planet from RV searches, and bright stars with a known transit from ground-based transit searches (Broeg et al. 2013). New constraints on the planetary interior structure and hence on the formation and evolution of planets, knowing masses and radii data, could be reached by this project (Fortier et al. 2014). Also, orbital dynamics and exomoons detection could be obtained. In this sense, the CHEOPS mission will be considered a photometric follow-up mission.

The spacecraft will be launched in 2017 and will reach the final position into a Sun Synchronous Low Earth Orbit (LEO) having a local time of ascending node (LTAN) of 6 am and an altitude in the range of 620 to 800 km (Broeg et al. 2013). This is required in order to have thermal stability of the instrument and straylight suppression from the Earth, to obtain high photometric stability.

The facilities on board of the spacecraft will be a 30cm effective aperture reflecting telescope to observe individual target star (Broeg et al. 2013), with an e2v CCD47-20 (13-μm pixel 1k $\times$ 1k , AIMO) as detector selected (Fortier et al. 2014). Approximately 500 targets of interest in its 3.5 year mission will be observed. The observations will have to not saturate star with magnitude $V \simeq 6.5$. On average, each planetary targets from RV searches will be observed for a total time of at least 50 minutes, whereas each planetary targets from ground-based transit searches will be observed for a total time of at least 80 minutes.

PLATO

The *PLAnetary Transits and Oscillation of stars*[21] (PLATO Rauer et al. 2014) will be the future third medium-class mission in European Space Agency (ESA) Cosmic Vision programme, studied for the research of extrasolar planets in transits. Different aims were studied for this mission. In particular, the most relevant goals will be the detection of new planetary systems, with photometric observations, linked with the creation of a statistical evaluation of the planetary parameters (mass, radius, mean density, age), the relation of the planetary type with host star and planetary system parameters (i.e. metallicity and spectral type of the host star, orbital distance of the planet from host stars, etc.), and the evolution of planetary system (Rauer et al. 2014). This search will be emphasised on terrestrial planets and on habitable zone around Solar-like host stars. In addition to these aims, other aims could be pursued. For example, the asteroseismology could be carrying on, in order to study stellar structure and evolution. At least, complementary goals could reach using the PLATO observations, such as the analysis of the accretion physics near compact objects or stellar activity and variability.

To obtain all these aims, the mission will must observe a huge number of stars, sampling all the stellar type and environments. Respect to the previous mission of CoRoT and Kepler, with defined number of targets or relative observed small fields, the PLATO mission will cover a huge sky surface, taking advantage of the kind of facilities on the spacecraft. In fact, PLATO will have available an array of 34 telescopes: 32 telescopes will be dedicated to normal observations in white light (with a large photometric dynamic range, between 4 and 16 mag), in order to obtain photometric series; the last 2 telescopes will be used to provide colour information in stellar analysis (Rauer et al. 2014). Each telescope will have a wide FoV of 1100 deg^2 and a

[20] http://cheops.unibe.ch/
[21] http://sci.esa.int/plato/

pupil diameter of 120 mm. Also, on the focal plane of each telescope is present an array of 2×2 CCDs: each CCD will have a 4510^2 of 18 μm pixel surface. The 32 "normal" telescopes will be assemble in group of 8 telescopes; all 8 telescopes have the same pointing direction, and each group have an offset in their pointing by 9.2° from the payload z-axis of the spacecraft. In this way, the total field of view of the PLATO facilities will be further increased until ∼2250 square degrees per pointing (see figure 1.1).

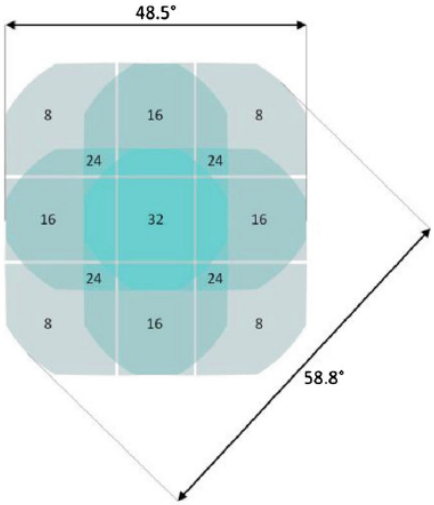

Figure 1.1: The total field of view coverage of PLATO facilities, with indicate the number of telescopes that cover the different sky regions (Rauer et al. 2014).

The spacecraft will be launched in 2022 and will reach the final position into the L2 lagrangian point. Here, the expected total mission lifetime will be of 6 years, with 2 of further extension. In these years, 2 observing strategies will be combined: the first one consists of 2 pointings will be chosen as long target field pointings (for 2 - 3 years each pointing); the second one consists of other pointings that will be done for a step-and-stare phase, otherwise shorter-period observations of several sky fields which will last 1 - 2 years total, in which a field will be observed for at least 2 months, up to a maximum of 5 months (Rauer et al. 2014).

This mission could increase significantly the number of planets discovered. In particular, the number of Earth-like and Super Earth-like planets could increase by a factor of ∼10 above Kepler and ∼1000 above TESS for planets with orbital period between 90 days and 500 days, whereas the increase could be by a factor of ∼10 - 20 above Kepler and TESS for planets up to 50 days orbital period (Rauer et al. 2014).

1.2.3 Research of planets inside open clusters

One important aim in the analysis of extrasolar planets is to define links between host star and planet or to define planetary formation and evolution theories (Janes 1996; Fischer & Valenti 2005). In this sense, the photometric analysis of components in stellar cluster, especially open cluster (OC), for the research of extrasolar planet is particular interesting because it is easier, in this crowded environment, to define the characteristics of the host stars and a relationship between planets and host stars can be obtained (Janes 1996).

In fact, the stars in OC are components of a uniform and easily characterising population and its parameters (i.e. age, metallicity, distance, etc.) are easier to be determine. OCs are important testbeds in which define the planetary formation and evolution theories. Moreover, using different OCs, therefore different stellar populations, theoretical relationships (i.e. fraction of planets and metallicity of host stars) can be defined (Fischer & Valenti 2005).

In conflict with these ideas there is the evaluation of a low percentage of success in detection of planets inside OCs (van Saders & Gaudi 2011). This lack will be due to low metallicities, that may have prevented planet formation, or to high rates of close stellar encounters in these clusters, that may have influenced the formation and subsequent evolution of planetary systems inside crowded environment (Chatterjee et al. 2012), or simply to a low number of sampled stars in cluster, that could not create a good statistics (van Saders & Gaudi 2011).
For example, we can consider only short-period planets, because it is thinkable, inside crowded environment such as OCs, that the number of long-period planets that survive at closed encounters phenomena is very low. In this case, the frequency of short-period planets is typically $\sim$1% (Cumming et al. 2008). Considering also transiting phenomena, the geometric probability that such a planet transits is only $\sim$10%. Then, 1 star out of 1000 could show a planet in transit (van Saders & Gaudi 2011). But this result will be obtained in ideal case where photometry and excellent temporal coverage are reached in any transit search. Considering different observation problems (i.e. low signal-to-noise ratio in some observation run, atmospheric or instrumental problems that prevent a perfect temporal coverage, etc.), the number of stars, in which at least one planet will be discovered, could increase even of a factor of 10 (van Saders & Gaudi 2011). Considering that the richest OCs contain a few thousand stars at best, the statistics of detection of planets could be not satisfied (van Saders & Gaudi 2011).

Despite this low percentage of success in planetary detection inside OC, different photometric analyses of all components of different OCs were done with the same surveys created for the research of exoplanets, in order to characterise stellar population. These analysis will be also useful in view of characterise possible detected transiting planets. An example of photometric analysis is Kovács et al. (2014) that studied HATNet dataset of Praesepe members, in order to discover variability and gyrochronological relation.

Furthermore, despite the bad statistics in planetary detection, a limited number of planets inside OC was detected (see table 1.1). At the moment, 12 planets were found inside six OCs: 10 of them were found using radial velocity method (Sato et al. 2007; Lovis & Mayor 2007; Quinn et al. 2012; Brucalassi et al. 2014; Quinn et al. 2014; Malavolta et al. 2016), whereas the other 2 were detected by photometric observations and analysis of transits in light curves (Meibom & Kepler Team 2013, see table 1.1). Among these discoveries, 5 planets were discovered using HARPS (Lovis & Mayor 2007; Brucalassi et al. 2014). Another one was found within the GAPS project, that uses HARPS-N facilities (Malavolta et al. 2016). The only two planets discovered with photometric observations were detected by Kepler mission (Meibom & Kepler Team 2013).

In table 1.1 all the planets inside OCs are reported.

Open Clusters	Planet	Spec. Type	$R_\star$ ($R_\odot$)	$M_\star$ ($M_\odot$)	$M_p \cdot \sin i$ (M_{Jup})	M_p (M_{Jup})	R_p (R_{Jup})	e	Orbital Period (days)	Disc. Met.	Ref.
Hyades	ϵ Tau b	K0 III	$13.70^{+0.06}_{-0.06}$	$2.7^{+0.1}_{-0.1}$	$7.6^{+0.2}_{-0.2}$	-	-	$0.15^{+0.02}_{-0.02}$	$594.9^{+5.3}_{-5.3}$	[1]	[S07]
Hyades	HD 285507 b	K4.5	$0.650^{+0.054}_{-0.054}$	$0.730^{+0.034}_{-0.034}$	$0.910^{+0.033}_{-0.033}$	-	-	$0.08^{-0.01}_{-0.01}$	$6.0881^{+0.0018}_{-0.0018}$	[1]	[Q14]
NGC 2423	No. 3 b	G IV/V	-	$2.4^{+0.2}_{-0.2}$	10.6	-	-	$0.21^{-0.07}_{-0.07}$	$714.3^{+5.3}_{-5.3}$	[1]	[L07]
NGC 4349	No. 127 b	K III	-	$3.9^{+0.3}_{-0.3}$	19.8	-	-	$0.19^{-0.07}_{-0.07}$	$677.8^{+6.2}_{-6.2}$	[1]	[L07]
M44	Pr0201 b	F7.5	$1.160^{+0.121}_{-0.121}$	$1.230^{+0.034}_{-0.034}$	$0.540^{+0.039}_{-0.039}$	-	-	0	$4.4264^{+0.0070}_{-0.0070}$	[1]	[Q12]
M44	Pr0211 b	G9 V	$0.860^{+0.078}_{-0.078}$	$0.95^{+0.04}_{-0.04}$	$1.840^{+0.064}_{-0.064}$	-	-	0	$2.1451^{-0.0012}_{-0.0012}$	[1]	[Q12]
M44	Pr0211 c	G9 V	$0.820^{+0.012}_{-0.012}$	$0.920^{+0.013}_{-0.013}$	$7.75^{+0.03}_{-0.03}$	$7.95^{+1.10}_{-0.50}$	-	$0.71^{-0.11}_{-0.11}$	4850^{+4560}_{-1750}	[1]	[M15]
M67	YBP 1194 b	G5 V	$0.99^{+0.02}_{-0.02}$	$1.01^{+0.02}_{-0.02}$	$0.34^{+0.05}_{-0.05}$	-	-	$0.24^{-0.08}_{-0.08}$	$6.958^{+0.001}_{-0.001}$	[1]	[B14]
M67	YBP 1514 b	G5 V	$0.89^{+0.02}_{-0.02}$	$0.96^{+0.01}_{-0.01}$	$0.40^{+0.11}_{-0.11}$	-	-	$0.39^{-0.17}_{-0.17}$	$5.118^{+0.001}_{-0.001}$	[1]	[B14]
M67	SAND 364 b	K3 III	$21.8^{+0.7}_{-0.7}$	$1.35^{+0.05}_{-0.05}$	$1.54^{+0.24}_{-0.24}$	-	-	$0.35^{-0.08}_{-0.08}$	$121.710^{+0.305}_{-0.305}$	[1]	[B14]
NGC 6811	Kepler-66 b	G0 V	$0.960^{+0.042}_{-0.042}$	$1.030^{+0.044}_{-0.044}$	-	-	$0.250^{+0.014}_{-0.014}$	-	$17.815815^{+0.000075}_{-0.000075}$	[2]	[M13]
NGC 6811	Kepler-67 b	G9 V	$0.770^{+0.031}_{-0.031}$	$0.860^{+0.034}_{-0.034}$	-	-	$0.262^{+0.014}_{-0.014}$	-	$15.7259^{+0.0011}_{-0.0011}$	[2]	[M13]

Table 1.1: Extrasolar planets found inside OCs. There are indicates the radius and the mass of the parent star ($R_\star$ and $M_\star$) in Solar units, the minimum mass and the real mass of the planet ($M_p \cdot \sin i$ and M_p) in Jupiter units, the radius of the planet (M_p) in Jupiter units, the eccentricity (e) and the period (in days) of the planetary orbit. The discovery method applied are: [1] Radial Velocity; [2] Photometric Transit. The references are: [S07] Sato et al. (2007); [Q14] Quinn et al. (2014); [L07] Lovis & Mayor (2007); [Q12] Quinn et al. (2012); [M15] Malavolta et al. (2016); [B14] Brucalassi et al. (2014); [M13] Meibom & Kepler Team (2013).

Chapter 2

Detrend of light curves

The variability search, explained in this thesis, was done using only photometric data. The data were obtained either through our photometric observations, or using data archives. In both of these cases, long term photometric series were carried out.

The analysed raw light curves were extracted from this kind of data set. Two kind of photometry were mostly followed: aperture photometry and PSF photometry. Both of these methods were applied on images prereducted with flat, bias and, when necessary, dark images. In some cases, a subtraction of the neighbour stars of each stellar target was also applied, using PSF modelling, to avoid flux contamination.

Before starting to make photometric variability analysis, the light curves taken into account have to be corrected from trends, that are not tied with the intrinsic nature of the star observed. Different procedures are followed for the correction of the raw light curves.

In this chapter, I will describe the origins of the trends that will be removed from the light curves and the problems that they could create in the research for variability. After that, I will describe the 3 methods that I used for the detrend.

2.1 Origin of systematics

Before analysis, light curves need to be corrected for systematics. These problems, that generate red noise, are in general not negligible (Pont, Zucker & Queloz 2006). Systematics could modify the signals inside the light curves and give detections that are not intrinsic to the stellar source. The origin of these systematics could have different nature and they are ascribable to facilities efficiency or at atmospheric extinction and observational conditions changes.

For example, instrumental or observational changes between the epochs could generate a change of the flux quantity from each source (Kovács, Bakos & Noyes 2005; Bakos et al. 2004). This variation in flux could be a constant shift in magnitude for narrow-fields surveys. Instead, in wide-field surveys, the variation in flux could become more complex, depending on the positions of the field and creating a smooth function of fitting parameters, such as the time and the coordinates.

General or local flux variation could have different kind of causes. They can be classified in this way:

- *Changes of atmospheric conditions.* These create a temporal dependence of PSF characteristics (Kovács, Bakos & Noyes 2005), shapes and widths, that could generate merging between flux contributions of two nearby stars. An important parameter that defines these

condition changes is the differential extinction, due to different atmospheric layers crossed in different epochs of the observational series. It is evaluated using airmass parameter. It changes during a long term photometric series, due to the variation height of the observed field on the horizon or due to the variation of the sky transparency, because of variation of weather conditions. These systematics could increase the background luminosity, damaging the detection of faint stars, that could be immersed into the noise.

- *Type of observed field.* The distribution and the type of stars neighbourhood, together with the density of objects inside a field, could create light contamination in the measurement of the flux of a given target star. These effects are strongly linked with the atmospheric conditions. In fact, in crowded field or with nearby bright stars, that are near the saturation limit, the target star flux could be significantly affected by nearby star flux. This effect increases more and more with the deterioration of the atmospheric conditions.

- *Instrumental effects.* The most important effect, due to used instrument, emerges during the motions of the stars across pixels with different quantum efficiency, due to hot-pixels or bad columns or due to the presence of gate structure of front-illuminated pixels. These effects create fake variations in stellar flux. The same kind of flux variations will be due to an imperfectly corrected pixels during the pre-reductions operations. Also, during observation series that cover more than one night, the geometrical distortion of the optics could create periodic effects inside light signals.

- *Periodic external events.* Phenomenons such as the 29 days period of the Moon cycle or the sidereal day period can change the background luminosity, then the noise into which the stars are immersed. These effects could create a periodic signal that could be measured inside stellar flux detection.

Removing the signals given by systematics could help to improve the signal to noise inside the light curve, in order to detect lower and lower amplitude magnitude variations that will belong to faint signals, such as ones of rocky planets in transit.

2.2 Correction using method SYSREM

One method, used to correct the light curves from systematics, is grounded on the SYSREM algorithm (Tamuz, Mazeh & Zucker 2005). This method considers that all light curves could have a common trend, due to external effects, such as the changing of the altitude of the observed stellar field, or the mechanical deflections during the tracking of the telescope along the night, or the weather variation during a long observation series.

These effects are evaluated with parameters that are not directly linked with the light curves. These parameters, such as airmass, are used to create a general trend, that will be subtracted to all light curves of the field of view.

The general trend will be weighed out with colour-dependent parameters or, in general, with parameters that are intrinsically linked to stellar properties. These parameters will be, for example, the colour itself of the star or the coordinates of the position on the CCD. In this way, the different behaviour of each kind of star with the changes of the surrounding conditions will be taken into account.

Given parameters that are dependent on image surrounding conditions or dependent of stellar intrinsic characteristics, SYSREM method makes “criss-cross” iterations (Tamuz, Mazeh & Zucker 2005) to create the most suitable sets of values of airmass for each image and of extinction coefficient for each light curve. Following the Bouguer’s law, the SYSREM method has to

minimise the global expression (following the symbolism of Tamuz, Mazeh & Zucker 2005):

$$S^2 = \sum_{ij} \frac{\left(r_{ij} - c_i a_j\right)^2}{\sigma_{ij}^2} \tag{2.1}$$

where $\{a_j;\ j = 1, ..., M\}$ is the airmass-like parameter of the j^{th} image, $\{c_i;\ i = 1, ..., N\}$ is the colour-like parameter of the i^{th} star, r_{ij} is the residual of each observation point, that is the the stellar magnitude after subtracting the average magnitude of the i^{th} star in the j^{th} image, and σ_{ij}^2 is the uncertainty of the measurement of the i^{th} star magnitude at the j^{th} temporal instant. To minimise S^2, if an initial set of airmass-like parameters $\{a_j\}$ is given, the method finds the set of colour-like parameters $\{c_i\}$, using the following expression, extracted from eq. (2.1):

$$c_i = \frac{\sum_j r_{ij} a_j / \sigma_{ij}^2}{\sum_j a_j^2 / \sigma_{ij}^2} \tag{2.2}$$

Vice-versa, if an initial set of colour-like parameters $\{c_i\}$ is given, the method finds the set of airmass-like parameters $\{a_j\}$ with the following expression:

$$a_j = \frac{\sum_i r_{ij} c_i / \sigma_{ij}^2}{\sum_i c_i^2 / \sigma_{ij}^2} \tag{2.3}$$

To minimise S^2, the equations (2.2) and (2.3) have to be used iteratively, until the best-fitting coefficients $\{^{(k)}\bar{c}_i\}$ and $\{^{(k)}\bar{a}_j\}$ are achieved for each k^{th} initial set of airmass-like or colour-like parameters, that is given to SYSREM to create the general trend.

These operations are done for all initial sets of parameters. Because of possible different systematic effects, depending on the initial kind of set of parameters used, after obtained a best-fitting coefficients and before to start with the other iterations with the following initial set of parameters, a new set of residuals are required to remove the difference due to different systematics. The new residuals are given by the following expression:

$$^{(k)}r_{ij} = ^{(k-1)}r_{ij} - ^{(k)}\bar{c}_i \, ^{(k)}\bar{a}_j \tag{2.4}$$

This new set of residuals enters in equation (2.1) and a new iteration could starts.

The combination of all sets of parameters $\{^{(k)}\bar{c}_i\}$ and $\{^{(k)}\bar{a}_j\}$ gives the j^{th} trend, created by systematics. It will be subtracted to the j^{th} raw light curve, obtaining a corrected light curve.

2.3 Correction using method TFA

Another method for the correction of the light curves is the Trend Filtering Algorithm (TFA; Kovács, Bakos & Noyes 2005). This method is based on the confirmation that in a large photometric data base, a lot of stars have light curves with similar features, ascribable to the same systematic effects. The TFA assumes that various systematics could be present inside different object light curves, but, with a large number of object inside the field of view, it is possible to describe all the systematics and eliminate them from stellar light curves.

The template set of light curves, to be used for the correction, will be constituted by the stablest star light curves, spread inside the field of view of the detector and covering the range of magnitude and colour of all the stars analysed, to create an empirical model for each single star in the sample (the methods for the selections are explained inside chapters 4 and 5, regarding data analysis). The choices for the light curve selection are done with the lack of a priori information

on the type of systematics influencing the targets (Kovács, Bakos & Noyes 2005). Anyway, light curves with low number of data points, low brightness and high standard deviations are typically rejected (Kovács, Bakos & Noyes 2005), in order to avoid any chance of biasing in target light curves.

Once obtained the sample of reference light curves, because no a priori knowledge about functional form of the systematics is given, the TFA method chooses to represent the filter function, to be used in the detrend of the target light curves, as a linear combination of the reference light curves contributions. This combination is explained in the following expression (following the symbolism of Kovács, Bakos & Noyes 2005):

$$F(i) = \sum_{j=1}^{M} c_j X_j(i) \tag{2.5}$$

where $\{F(i);\ i = 1, 2, ..., N\}$ is the filter function evaluated at the i^{th} of N instants of the common time-base, created by the merging of references and targets time-series, and $\{X_j(i);\ i = 1, 2, ..., N;\ j = 1, 2, ..., M\}$ is the template time-series of the M reference light curves preselected. In expression (2.5), it is assumed that the template time-series are zero-averaged (i.e., $\sum_{i=1}^{N} X_j(i) = 0$ for all j). The coefficients $\{c_j\}$ of the linear combination will be obtained minimising the following expression:

$$\mathcal{D} = \sum_{i=1}^{N} [Y(i) - A(i) - F(i)]^2 \tag{2.6}$$

where $\{Y(i);\ i = 1, 2, ..., N\}$ is the target time-series that will be filtered and $\{A(i);\ i = 1, 2, ..., N\}$ is the current best estimate of the detrended light curve. Without information about real periodic or aperiodic signal in the target light curve, $\{A(i)\}$ is set, before iterations, equal to the average of the target time-series ($A(i) = \langle Y \rangle$). With the iteration procedure on the equation (2.6) to obtain the best set of coefficients $\{c_j\}$ (until some convergence criterion is satisfied), the corrected time-series will be obtained in this expression:

$$\hat{Y}(i) = Y(i) - \sum_{k=1}^{M} c_j X_j(i) \tag{2.7}$$

This method uses weights for the reference light curves considering only the variations. Indeed, assuming that reference light curve variation is caused only by systematics (Kovács, Bakos & Noyes 2005), a simple least-squares criterion for the residuals, given by observed values minus filter prediction, will be a good solution, because most of the selected reference stars are non-variable. However, if variable stars enter wrongly inside the reference star list, the contribution in filter creation given by their light curves is lower than the contribution given by non-variable star ones. This is due to the preponderance of the presence of non-variable stars (Pojmański 2003): using a linear combination to create the filter of the detrend, this preponderance of non-variable stars is expressed in a nearly null contribution of variable stars during filter creation.

2.4 Another new method for the detrend: DeTrendy

In addition to the methods previously explained, our group developed another detrend method, explained in Nascimbeni et al. (2014). As done in TFA method, a set of light curves of the

stablest stars are used to create a synthetic trend. The selection of this sample will be done in the same way in which the template of light curves was obtained for TFA method, searching an uniform coverage in coordinates, in magnitudes and in colour (the methods for the selections are explained inside chapter 4, regarding data analysis).

After defining the sample of reference stars, 2 different methods are followed: a global differential photometry, for a global zero point correction, and a local differential photometry, for a weighted local zero point correction.

First of all the global zero point correction are applied. All the stars, with a extracted light curve in the field of view, are used for the creation of a global trend to be subtracted to each target light curve. Considering the set of M reference stars, the trend, created over each t^{th} temporal instant, is given by:

$$\tau_{\text{t}} = \left\langle m_{\text{t,j}} - \langle m_{\text{t,j}} \rangle_{\text{t}} \right\rangle_{\text{j}} \qquad j = 1, 2, ..., M; \qquad t = 1, 2, ..., N \tag{2.8}$$

where $\langle m_{\text{t,j}} \rangle_{\text{t}}$ is the median magnitude of the j^{th} reference light curve. So, each t^{th} point of the trend (τ_{t}), generated over each t^{th} temporal instant, is the median of all reference light curve magnitudes, beforehand normalised by the own light curve median magnitude. The global zero point corrected light curve for the i^{th} target star is simply given by:

$$m_{\text{t,i}}^{\text{GZP}} = m_{\text{t,i}} - \tau_{\text{t}} \tag{2.9}$$

where τ_{t} is the global trend given in equation (2.8).

The local zero point correction, instead, was done as follows. For each target in the field, a set of reference stars is created, grounding the selection on the following three parameters: the 68.27^{th} percentile of the residual distribution of the differential light curves, the distance over the field of view of the detector and the difference in magnitude between a given i^{th} target star and each j^{th} reference star. The weights given at each parameter are respectively:

$$R_{\text{ij}} = 1/\sigma_{\text{ij}}^2 \tag{2.10}$$

$$D_{\text{ij}} = \begin{cases} 0 & \text{if } r_{\text{ij}} < r_{\text{I}} \\ 1 & \text{if } r_{\text{I}} \leq r_{\text{ij}} < r_{\text{S}} \\ \exp\left[-\left(\frac{r_{\text{ij}} - r_{\text{S}}}{r_{\text{E}} - r_{\text{S}}} \right)^2 \right] & \text{if } r_{\text{ij}} \geq r_{\text{S}} \end{cases} \tag{2.11}$$

$$M_{\text{ij}} = \begin{cases} 1 & \text{if } m_{\text{ij}} < m_{\text{S}} \\ \exp\left[-\left(\frac{m_{\text{ij}} - m_{\text{S}}}{m_{\text{E}} - m_{\text{S}}} \right)^2 \right] & \text{if } m_{\text{ij}} \geq m_{\text{S}} \end{cases} \tag{2.12}$$

where σ_{ij} is the 68.27^{th} percentile of the residual distribution and r_{ij} and m_{ij} are, respectively, the distance over the field of view and the modulus of the difference in magnitude between the i^{th} target star and each j^{th} reference star. The values r_{I}, r_{S} and m_{S} are, respectively, the lower and the upper limit values in distance over the field of view and the upper limit value in magnitude difference, that define the stars with unitary weight factor in distance over the field of view and in magnitude difference. A null factor is given for r_{ij} less than r_{I}, to avoid to use reference stars too close to the target and with the flux affected by the target star flux. Instead, r_{E} and m_{E} are the scale radius, for distance over the field of view and magnitude difference between target and reference, in which the factors D_{ij} and M_{ij}, respectively, are $1/\text{e}$.
Using the weights given in equations (2.10), (2.11) and (2.12), we obtain the general weight for each couple of target and reference stars:

$$W_{\text{ij}} = R_{\text{ij}} \cdot D_{\text{ij}} \cdot M_{\text{ij}} \tag{2.13}$$

The local zero point corrected light curve for the $i^{\rm th}$ target star is given by:

$$m^{\rm LZP}_{\rm t,i} = m_{\rm t,i} - \tau_{\rm t,i} \tag{2.14}$$

where the local trend is given by:

$$\tau_{\rm t,i} = \frac{\sum_{\hat{j}=1}^{N_{\rm i\hat{j}}} W_{\rm i\hat{j}} \cdot \left(m_{\rm t,\hat{j}} - \left\langle m_{\rm t,\hat{j}} \right\rangle_{\rm t} \right)}{\sum_{\hat{j}=1}^{N_{\rm i\hat{j}}} W_{\rm i\hat{j}}} \tag{2.15}$$

where the index $\hat{j}$ points out the reference stars with the weight $W_{\rm ij}$ sorted in decreasing way. $N_{\rm i\hat{j}}$ is the maximum number of the reference light curves used for the local zero point correction and with the highest weights. Typically, in our analysis, $N_{\rm i\hat{j}}$ was put equal to 50.

After applying both of the methods above explained, the corrected light curve with the best rms will be used in following analysis (see chapter 4 for the application of this method).

Chapter 3

Searching for variability in light curves: methods

The light curves corrected from all the different kind of systematics could be considered such as the true relation of the light intensity of the respective star in function of the time. This means that, if the star is a structure with no kind of variation in the own characteristics, the light curve would be a constant in magnitude along all the temporal coverage, for less than white noise that produces a random distribution of the points around the mean magnitude value.

Sometimes stellar structure could be characterised by intrinsic variability, that would be either periodic or not. This variability could be due to different stellar peculiarity. In general, following the *General Catalogue of Variable Stars*[1] (Kholopov et al. 1985a,b, 1987, 1990; Samus, Durlevich & et al. 2009), the stellar variability could be classified in 6 classes (Sterken & Jaschek 2005):

- *Eruptive variables*: they are stars that vary their brightness because of violent processes and flares inside chromospheres and coronae;
- *Pulsating variables*: they are stars that vary their brightness because of periodic expansions and contractions of their surface layers, both in radial and in non-radial directions;
- *Rotating variables*: they are stars with ellipsoidal shape or with non-uniform surface brightness, due to presence of spots or some thermal or chemical inhomogeneity of stellar atmospheres caused by magnetic field; the stellar axial rotational motion, in combination with the causes previously quoted, produce the brightness variability;
- *Cataclysmic (explosive and nova-like) variables*: they are stars with outbursts caused by thermonuclear burst processes in their surface layers (Novae) or deep in their interiors (Supernovae);
- *Eclipsing variables*: they are systems of binary stars that, due to the mutual orbits, produce eclipse phenomena;
- *X-ray sources*: they are particular cases of close binary systems, that produce a strong variability in X-ray radiation.

[1] http://www.sai.msu.ru/gcvs/gcvs/index.htm

Besides all the intrinsic stellar variability previously described, the stars could have a planetary system around itself and the stellar system components, such as planets, could change star brightness due to transit phenomena, like eclipsing binary cases. In this case, part of the stellar disk is hidden by the planet, that shades part of the stellar flux to the observer. Moreover, in the case of non periodic phenomena, it could happen that a star, with planets orbiting around it, transits in front of other farther stars, producing the gravitational lensing phenomenon, with a brightness amplification for the field stars. The "transit" of the exoplanet with the parent star in front of field stars could further magnify the brightness.

Each of these kind of variability produce a particular shape inside the light curve. Different methods are developed for the search of variability inside photometric and spectroscopic data. In this chapter, I explain the methods that I used for the search of periodic variability inside light curves, extracted from photometric data. With the different methods used, I explain how demonstrate the goodness of a variability detection.

3.1 Preliminary selections of possible variable light curves: parameters

After the correction from systematics and first of any kind of variability research, a good procedure is to clip the light curves from the outliers, to remove the unreliable measurements. Following a procedure that is quite similar to the one described in Hartman et al. (2008), two cleaning passages will be done.
The first one, in the case of light curves with few points strewn in the temporal coverage, is to compute the median for each single light curve and to clip all the points out of $m\sigma$ over the residual distribution. The value of m will be decided according to the kind of variability that we want to search and according to the number of σ that could be observed in literature in the different variability. In the case of high cadence temporal sampling light curves, before the clip, each data point is substituted with a median of n nearest points in temporal coverage, creating a median model to subtract to the real light curve. The residuals, obtained from the subtraction between real light curve and the "median" synthetic light curve, are evaluated like previously described, computing the median and clipping all the points out of $m\sigma$. This is done to remove transient phenomena that are not intrinsic to the star, such as cosmic ray or satellite tracks.
The second one is to normalise all the light curves to the corresponding median and to create a general trend of all the light curves, computing medians of all the normalised light curve data points for each temporal instant. Then, from this general trend, the temporal instants with points out of 3 σ over the residual distribution are rejected. In this way, I can reject those instants, in which a large number of light curves have outliers, probably due to systematic problems. These cleaned light curves are then useful to search for periodicity signals.

At this point, the light curves will be preselected, using some parameters that could help in the variability research.
First of all, the median magnitude, the number of data points and the 68.27^{th} percentile of each light curve will be good preselection parameters. Indeed, star light curves with median magnitude that exceeds or is near to the limit of saturation could have variability signals that could be created by problems linked with saturation of the star itself in some or in all the images. Detection of false variability will be obtained also with faintest stars, because of lack of flux information in some images. Instead, light curves with greater and greater 68.27^{th} percentile values could indicate stars that will be more and more probably variable.

These three parameters could be used in the following way. The bright magnitude limit is used to select all the stars that are saturated in a percentage of the images larger than a given

limit, that depends on total temporal coverage and on characteristics (e.g. data points density or sampling), and that are not good for analysis of variability. Also, using the same magnitude limit, all the data points with magnitude that exceeds this limit are clipped. After that, a limit in number of data points (weighted with the temporal dispersion or median temporal density) will be used to exclude the light curves that have a number of points too low in order to define if the star itself is variable or not. At the end, a 68.27^{th} percentile distribution of residuals of the light curves in function of the median magnitude will be created. In this distribution, the light curves with a 68.27^{th} percentile less then one sigma of the distribution were not studied for periodicity.

After these clippings, it is time to make selections using the production of the methods to search for periodical variability.
Before analysing variability and running the different algorithms, it is a good practice, if it is not already done, a conversion of the temporal axis for all the light curves to Barycentric Julian Date (BJD) in Barycentric Dynamical Time (TDB) standard, providing, with this standard, consistency and reliability, in particular on long temporal baselines (Eastman, Siverd & Gaudi 2010).
Different methods were created in the past, to search for variability signals with different peculiarity. Despite the different theories behind each method, similar parameters for the estimate of variability detection are produced. In particular, depending on the cases and the data characteristics, for each method a False Alarm Probability (from here on FAP) parameter could be estimated. The idea is to use a preliminary limit in FAP to exclude all the periodicity that has low probability to be a real variable signal.
After this first cut, a second selection will be done over the variability periods. In particular, using the histogram of periodicity of light curves, all the bins that exceed a limit in counts of light curves with about the same period will be left out of the pool of final light curves with a possible real variability. The goal is to exclude those signals that are created by common effects in different light curves. These effects can be due to the sampling of the observations or by periodical effects on the facilities and that are not be totally corrected with the detrend operations. Between these last light curves excluded from the histogram, it is possible that someone could be reintegrate in the final group. Considering the group of these last light curves, a second FAP limit is applied. This limit is stricter than the previous one. Typically, I use a limit 5 times greater than the previous one. If the light curves, excluded from the histogram, have a FAP greater than the second stricter limit, they are reintegrated inside the final group of light curves with good probability to have real periodic variability signals. This last reintegration is done to take into account those light curves that, despite the signal that has a periodicity alike to one of many other light curves, have an high probability to show a real intrinsic variability.

After these last selection, we obtain a good set of light curves that could be valiant variables. Only a last visual check over the shape of phased light curves could give the certainty, although subjective in some cases, that a light curve belongs to a variable star.

3.2 Lomb Scargle and Generalised Lomb Scargle Methods

This is one of the first methods created for the analysis of the periodicity (Lomb 1976; Scargle 1982; Horne & Baliunas 1986; Press & Rybicki 1989; Press et al. 1992). It searches for a detection of periodical variability in light curves, that could be fitted by sinusoidal function.

This method was improved in particular for non-uniformly spaced data. Indeed, in ground based astronomical long term observations, it is impossible to obtain uniform temporal spacing data. In this situation, previous developed standard methods, such as Fast Fourier Transform

(FFT) algorithm, could be no more suitable (Lomb 1976).

The Lomb Scargle method (from here on LS) is based on periodogram analysis that, with least squares methods, could ignore the non-equal spacing data. Periodogram analysis is based on the Discrete Fourier Transform (DFT). Following this basic tool (Scargle 1982), with a sampled data set $\{X(t_i),\, i = 1, ..., N_0\}$, the periodogram is conventionally described with this equation:

$$\begin{aligned} P_X(\omega) &= \frac{1}{N_0} \left| FT_X(\omega) \right|^2 \\ &= \frac{1}{N_0} \left| \sum_{j=1}^{N_0} X(t_j) \exp\left(-i\omega t_j\right) \right|^2 \\ &= \frac{1}{N_0} \left[\left(\sum_j X(t_j) \cos\left(\omega t_j\right) \right)^2 + \left(\sum_j X(t_j) \sin\left(\omega t_j\right) \right)^2 \right] \end{aligned} \tag{3.1}$$

where $TF_X(\omega) = \sum_{j=1}^{N_0} X(t_j) \exp\left(-i\omega t_j\right)$ is the expression of the Discrete Fourier Transform spectral analysis (Deeming 1975), with ω frequency variable and t_j the *sampling* observation time instants of the data set $X(t_j)$.

Scargle (1982) introduced, in the place of equation (3.1), a slightly different expression, redefining the periodogram in this way:

$$\begin{aligned} P_X(\omega) = \frac{1}{2} \Bigg\{ & \frac{\left[\sum_{j=1}^{N_0} X(t_j) \cos\left(\omega\left(t_j - \tau\right)\right) \right]^2}{\sum_{j=1}^{N_0} \cos^2\left(\omega\left(t_j - \tau\right)\right)} + \\ & + \frac{\left[\sum_{j=1}^{N_0} X(t_j) \sin\left(\omega\left(t_j - \tau\right)\right) \right]^2}{\sum_{j=1}^{N_0} \sin^2\left(\omega\left(t_j - \tau\right)\right)} \Bigg\} \end{aligned} \tag{3.2}$$

where the τ value is expressed in this way:

$$\tan\left(2\omega\tau\right) = \left(\sum_{j=1}^{N_0} \sin\left(2\omega t_j\right) \right) \Big/ \left(\sum_{j=1}^{N_0} \cos\left(2\omega t_j\right) \right) \tag{3.3}$$

The equation (3.2) was created for three reasons. First of all, it has a simple statistical behaviour (Scargle 1982). Indeed, $P_X(\omega)$ is defined in a way in which $X(t_j)$ is purely noise: in this sense, the power in $P_X(\omega)$ follows an exponential probability distribution (Horne & Baliunas 1986), useful for the computation of the False Alarm Probability. Second, the equation (3.2) makes the periodogram analysis equivalent to the least-squares fitting analysis to the data, using a sinusoidal function (Scargle 1982; Horne & Baliunas 1986). Moreover, introducing the τ term, it was possible to make the periodogram invariant to a shift of the origin of time, despite the uneven temporal sample.

In the particular case in which temporal sample is evenly taken ($\Delta t = 1$ and $t_j = j$), equations (3.1) and (3.2) are both simplified in this expression (Scargle 1982):

$$P_X(\omega) = \frac{1}{N_0} \left| \sum_{j=1}^{N_0} X(t_j) \exp\left(-ij\omega\right) \right|^2 \tag{3.4}$$

expression typically evaluated in the particular set of N evenly spaced frequencies, where $N = N_0/2$. This set is useful to sample the frequency range distribution of the periodogram from the fundamental frequency ($\omega_1 = 2\pi/T$), given by a sine wave with a period equal to the whole temporal interval T in which observations are done, and the Nyquist frequency, given by $\omega_N = \frac{1}{2}(2\pi/\Delta t) = \pi N_0/T = 2\pi N/T$, where $\Delta t = T/N_0$. In the case of uneven data sample, the fundamental frequency could be maintained the same to the even sample case. As regards the case of the Nyquist frequency, it is more complicated, because of an ambiguous definition (Δt will be the minimum difference between two consecutive temporal instants, otherwise an average value, or even other definitions). In this case, the spectral window function (Deeming 1975; Lomb 1976; Scargle 1982) will become useful to choose the natural N frequencies to take into account during the periodogram analysis.

Given a set of natural frequencies, to define the probability that a variability detection is real or false, a good parameter to use will be the False Alarm Probability (FAP). In particular, in LS method, the FAP has an exponential distribution. This kind of distribution is created after the normalisation of the $P(\omega)$ periodogram power. To obtain an exponential distribution, the correct normalisation to apply will be made dividing the $P(\omega)$ by the total variance σ^2 of the data (Horne & Baliunas 1986):

$$P_N(\omega) = \frac{P_X(\omega)}{\sigma^2} = \frac{e^{-z/\sigma^2}}{\sigma^2} \tag{3.5}$$

Assuming that in equation (3.2) $X(t_j)$ is pure independently and normally (Gaussian) distributed noise, with zero mean and constant variance, $P_X(\omega)$ is equal to a Γ distribution (Horne & Baliunas 1986). In this way, the periodogram has the desired e^{-z} probability distribution.
With this probability distribution, at a given frequency ω_0, the probability that $P_N(\omega_0)$ is of height z or higher is $Pr[P_N(\omega_0) \geq z] = e^{-z}$. Supposing that z is the highest peak value of the periodogram, composed by a sample of N_i independent frequencies, the probability that each independent frequency has a smaller power than z is $1 - e^{-z}$. The probability that all the independent frequencies have a smaller power than z is $[1 - e^{-z}]^{N_i}$. So, the probability that the data contain a signal at given frequency is given by:

$$Pr = 1 - F = \left[1 - e^{-z}\right]^2 \tag{3.6}$$

where $F = 1 - [1 - e^{-z}]^2$ is the False Alarm Probability, that describes that some peak is of height or higher than peak with z power.
The FAP described above is correct for even sample. For uneven sample, considering N_i, number of independent frequencies, given by Nyquist frequency, the FAP is overestimated. In these cases, a series of simulations could give a correct estimate of FAP value.

Zechmeister & Kürster (2009) improved later the Lomb Scargle method. In particular, two shortcomings are overcome: the weighing out of the error measurements inside data, already resolved by Gilliland & Baliunas (1987) and Irwin et al. (1989), and the assumption that the mean of the data, that is subtracted during the analysis, is the same at the mean of the fitting sine function, overcome with the assumption of an offset c in the sine wave fitting function:

$$y = a\cos(\omega t) + b\sin(\omega t) + c \tag{3.7}$$

This new algorithm, defined generalised Lomb-Scargle (GLS), is less susceptible to aliasing and provides more accurate frequencies than LS.

3.3 Method of Analysis of Variance

The method of the Analysis of Variance (from here on AoV) was implemented by Schwarzenberg-Czerny (1989) and developed by Devor (2005). It is sensitive to periodic features, without assuming particular fitting function.

The AoV is based on folded and binned data in trial phases. The algorithm tries to find the best fitting trend on the binned points in the phased data set. This is useful in particular for the search for sharp periodic signal, such as narrow pulses, that with a sinusoidal profile (i.e., given by LS or GLS method; see section 3.2) becomes impossible to be fitted in a good way, rendering them less detectable (Schwarzenberg-Czerny 1989). The number of bins is arbitrary and it is defined depending on the kind of variability signal we want to find. When a non-specific variability shape is researched, a typical value of number of bins is eight (Devor 2005).

The FAP parameter for this method, to emphasise the likely real variability, is based on the standard AoV test statistic parameter Θ_{AoV} (Schwarzenberg-Czerny 1989). This parameter is explained below.

We define the following statistics:

$$\begin{aligned}(r-1)s_1^2 &= \sum_{i=1}^{r} n_i(\bar{x}_i - \bar{x})^2 \\ (n-r)s_2^2 &= \sum_{i=1}^{r}\sum_{j=1}^{n_i}(x_{ij} - \bar{x}_i)^2 \qquad (3.8)\\ (n-1)s_0^2 &= \sum_{i=1}^{r}\sum_{j=1}^{n_i}(x_{ij} - \bar{x})^2 \\ (n-1)s_0^2 &= (r-1)s_1^2 + (n-r)s_2^2 \qquad (3.9)\end{aligned}$$

where n is the total number of observations and $\bar{x}$ their average, r is the number of bins, n_i is the total number of observations inside the i^{th} bin and $\bar{x}_i$ their average and $x_{ij} = x(t_{ij})$ is the individual j^{th} element inside the i^{th} bin, obtained at temporal instant t_{ij}.
Considering the case of pure noise signal (Schwarzenberg-Czerny 1989), where observations are Gaussian white noise, with zero mean and unitary variance, $(n-1)s_0^2$, $(r-1)s_1^2$ and $(n-r)s_2^2$ become χ^2 with $r-1$, $n-r$ and $n-1$ degrees of freedom. In particular, s_1^2 and s_2^2 are independent. To confirm this hypothesis, it is used the parameter $\Theta_{AoV} = s_1^2/s_2^2$. It is a ratio between independent χ^2 random variables: this is a Fisher-Snedecor F distribution with $r-1$ and $n-r$ degrees of freedom. It is possible to obtain the mean and the variance of Θ_{AoV} in the following expressions:

$$E[\Theta_{AoV}] = \frac{n-r}{n-r-2} \qquad (3.10)$$

$$Var[\Theta_{AoV}] = \frac{2(n-r)^2(n-3)}{(r-1)(n-r-2)^2(n-r-4)} \qquad (3.11)$$

Considering the asymptotic case in which $n \to \infty$ $r \to \infty$ and $r/n \to 0$, we obtain the expressions for expected value and variance of Θ_{AoV}:

$$E[\Theta_{AoV}] = 1 \qquad (3.12)$$

$$Var[\Theta_{AoV}] = \frac{2(n-1)}{(r-1)(n-r)} \qquad (3.13)$$

In the case in which are present noise and periodic signal inside data set, the data elements become $x_{ij} = a_{ij} + Af_{ij}$, where a_{ij} is Gaussian white noise, with zero mean and unitary variance, and f is an arbitrary periodic function, with period P_0 and unitary amplitude. The periodic signal in the data set x_{ij} has A amplitude and P period. Statistics inside equations (3.8) have the following average values:

$$\begin{aligned} E[s_1^2] &= 1 + A^2F_1^2 = 1 + A^2\frac{1}{r-1}\sum_{i=1}^{r} n_i(\bar{f}_i - \bar{f})^2 \\ E[s_2^2] &= 1 + A^2F_2^2 = 1 + A^2\frac{1}{n-r}\sum_{i=1}^{r}\sum_{j=1}^{n_i}(f_{ij} - \bar{f}_i)^2 \\ E[s_0^2] &= 1 + A^2F_0^2 = 1 + A^2\frac{1}{n-1}\sum_{i=1}^{r}\sum_{j=1}^{n_i}(f_{ij} - \bar{f})^2 \end{aligned} \tag{3.14}$$

Considering the asymptotic case in which $n \to \infty$ $r \to \infty$ and $r/n \to 0$, we obtain the expressions for expected value and variance of Θ_{AoV}:

$$E[\Theta_{AoV}] = 1 + A^2(F_1^2 - F_2^2) + \mathcal{O}(A^4) = 1 + A^2(F_0^2 - F_2^2)\frac{n-1}{r-1} + \mathcal{O}(A^4) \tag{3.15}$$

otherwise, the expression of the FAP for the AoV method.

3.4 Method Box-fitting Least Square algorithm

The Box-fitting Least Square algorithm (from here on BLS; Kovács, Zucker & Mazeh 2002) fits a boxy function on phased light curves, finding periodical signals produced, for example, by transiting planets or eclipsing binaries. The method is based on direct Least Squares method. The method fits different trial step functions to sample different possible signals. Each signal fitted corresponds to a trial period. BLS, fitting all the trial step functions, tries to find the best fitting function and the best variability period.

The algorithm (Kovács, Zucker & Mazeh 2002) takes into account a function with two constant value H and L, where $H > L$. It tries to fit the data with the best function of this type, otherwise to find the best model, estimating the five following parameters: L and H, lower and greater constant values of the fitting function, P_0 period of the entire variability, q fraction of the function that have value L and t_0 central temporal instant of the fraction q of the fitting function, that is the epoch of the transit.
To do that, the algorithm uses the data set $\{x_i,\, i = 1, ..., n\}$, where each x_i has an additive zero-mean Gaussian noise, with σ_i standard deviation, and a weight given by the expression:

$$w_i = \sigma_i^{-2}\left[\sum_{j=1}^{n}\sigma_j^{-2}\right]^{-1} \tag{3.16}$$

The data set $\{w_i x_i\}$ is assumed have a zero arithmetic average (Kovács, Zucker & Mazeh 2002).

The data set is put in trial phases, given resorted folded data set $\{\tilde{x}_i\}$ with corresponding weights $\{\tilde{w}_i\}$. A step function is fitted over the folded time series, having $\hat{L}$, where $i_1 \leq i \leq i_2$, and $\hat{H}$, where $i < i_1$ or $i > i_2$, like trial constants of the fitting function. Using all the combinations

of the parameters (i_1, i_2), the algorithm tries to minimise the expression:

$$\begin{aligned}\mathcal{D} &= \sum_{i=1}^{i_1-1} \tilde{w}_i \left(\tilde{x}_i - \hat{H}\right)^2 + \sum_{i=i_2+1}^{n} \tilde{w}_i \left(\tilde{x}_i - \hat{H}\right)^2 + \sum_{i=i_1}^{i_2} \tilde{w}_i \left(\tilde{x}_i - \hat{L}\right)^2 \\ &= \sum_{i=1}^{n} \tilde{w}_i \tilde{x}_i^2 - \frac{s^2}{r(1-r)} \end{aligned} \tag{3.17}$$

where there are:

$$r = \textstyle\sum_{i=i_1}^{i_2} \tilde{w}_i \tag{3.18}$$

$$s = \textstyle\sum_{i=i_1}^{i_2} \tilde{w}_i \tilde{x}_i \tag{3.19}$$

$$\hat{L} = s/r \tag{3.20}$$

$$\hat{H} = -s/(1-r) \tag{3.21}$$

Minimising the equation (3.17), we obtain the best value for L, H, P_0, q and t_0 and the best fit boxy function.

The first term in last right hand side in (3.17) does not depend on the trial period, so only the second characterises the quality of the fit. Indeed, we could define the BLS frequency spectrum using the Signal Residue (SR) computed over each given trial period (Kovács, Zucker & Mazeh 2002):

$$SR = \text{MAX}\left\{ \left[\frac{s^2(i_1, i_2)}{r(i_1, i_2)[1 - r(i_1, i_2)]} \right]^{\frac{1}{2}} \right\} \tag{3.22}$$

where the maximisation is done over $i_1 = 1, 2, ..., n^\star$ and i_2 follows the inequality $\Delta i_{\min} < i_2 - i_1 < \Delta i_{\max}$, where $\Delta i_{\min/\max}$ are the minimum/maximum of the range of fractional transit length (i.e., q parameter), suspected to be present in the signal and explored in equation (3.17). Parameter $n^\star$ depends on $i_2 - i_1$ subtraction and covers the range of $[n - \Delta i_{\max}, n - \Delta i_{\min}]$. SR is directly proportional to $\delta \equiv H - L$, otherwise the depth of the transit signal. Indeed, using equations (3.20) and (3.21), we obtain in the best fitting function:

$$SR = \hat{\delta}\sqrt{r(1-r)} \tag{3.23}$$

Typically, the BLS method evaluates SR dividing the folded time series into m bins and using these binned values in place of the points of the unbinned light curves.

To indicate the probability that a signal given by the BLS method is a real transit or a false signal, a good FAP parameter to use, following the example of Hartman et al. (2008, 2009), is the signal-to-pink-noise. This parameter is given by the following expression (Pont, Zucker & Queloz 2006):

$$(S/N)^2 = \frac{\delta^2}{\sigma_w^2/n_t + \sigma_r^2/N_t} \tag{3.24}$$

where δ is the depth of the eclipse, n_t is the number of points in the eclipse, N_t is the number of distinct eclipses sampled, σ_w is the white noise, and σ_r is the red noise at the timescale of the eclipse.

Another parameter will be the Signal Detection Efficiency (SDE), that could be written in this way:

$$SDE = \frac{SR_{\text{peak}} - \langle SR \rangle}{sd\langle SR \rangle} \tag{3.25}$$

where $SR_{\rm peak}$ is the SR at the highest peak, $\langle SR \rangle$ is the average of SR parameter and $sd\langle SR \rangle$ is its standard deviation. This parameter, however, depends on the time spanned by the data and on the lengths and position of the frequency band of the analysis. If all these listed parameters are maintained constant in all the light curves, SDE parameter will be useful to evaluate the FAP.
Other parameter could be the $\Delta\chi^2$, otherwise the reduction of the χ^2 after the subtraction of the model given by the boxy function, as the best fit of the data. A last parameter, at least, will be the signal-to-noise estimated from the data sets inside each bin of the time series. This binning of the light curves is typically done for the estimate of the SR parameter, given by equation (3.22).

Chapter 4

Stellar variability of M44 (Praesepe, NGC 2632) field stars

The Praesepe open cluster (M44; l,b = 205.9195°, +32.4843°; α,δ = 08^h 40^m 24^s, +19° 40' 00"; Kharchenko et al. 2013) lies at (181.5 ± 6.0) pc from the Sun and is ∼800 Myr old (van Leeuwen 2009). Its half-mass radius is 3.9 pc (Khalaj & Baumgardt 2013) and its core radius is 0.8 pc (Piskunov et al. 2007). Other authors already studied this open cluster (OC), finding several variable stars (see Mermilliod, Mayor & Udry 2009; Delorme et al. 2011; Kovács et al. 2014, and references therein). Also, two planets were discovered inside this OC (Pr 211 b and Pr 201 b Quinn et al. 2012) and the first multiple planetary system belonging to star clusters was discovered by Malavolta et al. (2016, with the discovery of Pr 211 c). In order to analyse this OC, I exploited public data from the SuperWASP project and proprietary data from our campaign at the STELLA 1 Telescope.

4.1 Observations

4.1.1 SuperWASP - Facilities and observations

The *Super Wide Angle Search for Planets*[1] (SuperWASP) project is based on two arrays of eight telescopes each, one located at the Roque de los Muchachos observatory, on La Palma (Canary islands), and one at the South African Astronomical Observatory (SAAO), near Sutherland (South Africa) (Pollacco et al. 2006; Butters et al. 2010). Each SuperWASP camera is equipped with a 2048×2048-pixel Andor CCD, with a 13.7 arcsec/px pixel scale and a (7.8 × 7.8) deg^2 field of view. The observing cadence is short, with an exposure time of 30 sec. The main scientific aim of the project is to find transits of extrasolar planets on stars bright enough to perform spectroscopic follow-up observations. The project started in 2004 and it is still active. The public archive[2] covers a period from 2004, May 2^{nd} to 2008, October 9^{th}. In 2004, the observations were performed without any filter (Butters et al. 2010; Smith & WASP Consortium 2014); from 2006 a wide-band filter (400 - 700 nm) was installed.

The SuperWASP public observations of M44 spans ∼3,5 years, between 2004, September 13^{th} and 2008, April 18^{th} (see figure 4.4 at page 42). I selected the M44 member stars by cross-matching the SuperWASP public archive with the catalogue of Kraus & Hillenbrand (2007). I

[1] http://www.superwasp.org/

[2] http://exoplanetarchive.ipac.caltech.edu/docs/-SuperWASPMission.html

also selected all the stars within 6.5° from the cluster centre. The cut in declination at +20° is a limitation of the public SuperWASP archive, which released only stars between +20° and +65.86° in declination. Overall, 27872 field stars and 133 M44 members were detrended and analysed.

The light curves (LCs) were grouped according to the different cameras and filters used. My field is covered by 2 unfiltered cameras and by 7 visual band cameras. The LCs were extracted by SuperWASP team using an aperture photometry algorithm (Butters et al. 2010; Kane et al. 2004). Overall, my initial sample is made of 91905 LCs (see table 4.1).

Camera ID	Number of stars		Number of data points		Filter
	All	M44	All	M44	
#103	3472	0	8	0	None
#104	13367	19	143	119	None
#141	25534	131	3558	3552	Visual
#142	24371	130	7492	3763	Visual
#143	2548	0	133	0	Visual
#144	7145	1	3146	27	Visual
#146	7033	5	6967	6235	Visual
#147	6051	106	3871	2626	Visual
#148	2384	88	46	46	Visual
Total	27872	133	10284	-	

Table 4.1: Summary of my input stellar sample. The columns give: the number of field stars and M44 members, the number of data points, and the filter. The total number of selected stars is indicated in the last row of the table, both from entire field of view and from M44 selection (following Kraus & Hillenbrand 2007). Also the total number of data points is indicated.

4.1.2 STELLA 1 - Facilities and observations

M44 was also observed by the STELLA robotic telescope at the Teide Observatory[3] (Tenerife). STELLA is composed of two fully automatic altazimuth 1.2m telescopes (STELLA 1 and STELLA 2) and its original focus was on STELLar Activity (whence the acronym STELLA; Korhonen et al. 2007; Weber, Granzer & Strassmeier 2012), i.e. to monitor the stellar activity with simultaneous photometry and spectroscopy. My group was awarded of STELLA observing time for 3 years consecutively, from 2013, March 12$^{\text{th}}$ to 2013, April 17$^{\text{st}}$, from 2014, March 20$^{\text{th}}$ to 2014, May 31$^{\text{st}}$ and from 2015, February 11$^{\text{th}}$ to 2015, March 5$^{\text{st}}$.

Our observing setup involved the Wide Field STELLA Imaging Photometer (WiFSIP), a ITL camera with 4096×4096 back-illuminated thinned CCD, with 15μm pixels, mounted at STELLA 1. The field of view is 22×22 arcmin with a 0.32 arcsec/px pixel scale. We cycled our pointings through different fields: in the 2013 and 2015 campaigns the fields observed were 4, whereas in 2014 campaign the fields observed were 6. Each of them was observed in B Johnson filter and in r Sloan filter. The exposure time was different in each campaign: 3×80s $B + 3 \times 80$s R (2013), 3×20s $B + 3 \times 180$s $B + 3 \times 120$s R (2014), and 3×90s $B + 3 \times 30$s R (2015). In table 4.2 I show the number of images taken in the different campaigns, per filter and exposure time. The number of LCs extracted from our three campaigns is summarised in table 4.3.

[3] http://www.aip.de/en/research/facilities/stella/

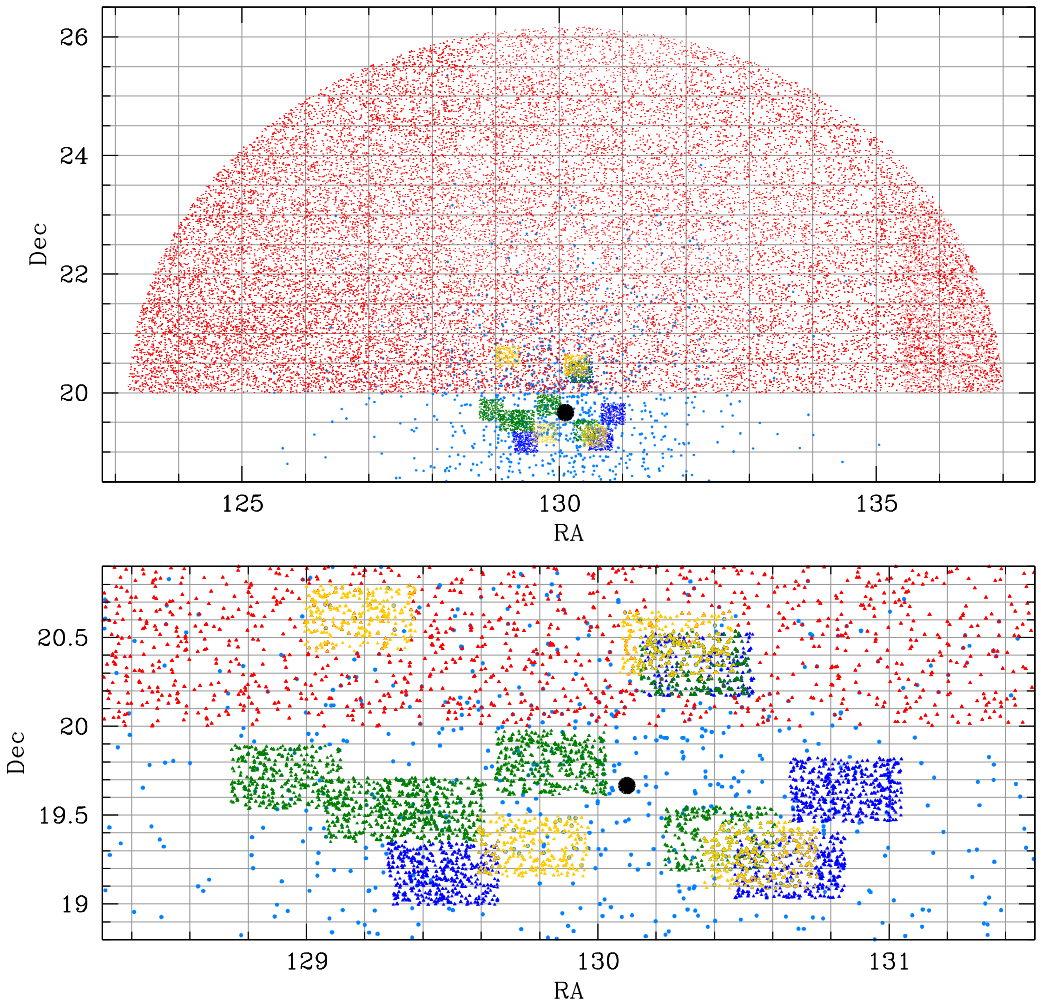

Figure 4.1: *Top panel*: the M44 fields. Stars observed by SuperWASP are plotted in red. Stars observed by 2013, 2014, and 2015 STELLA1 campaigns are plotted in blue, green, and yellow respectively. The black dot marks the centre of M44, whereas light blue points mark M44 members (according Kraus & Hillenbrand 2007).
Bottom panel: the field around the STELLA1 pointings is zoomed.

		N° of images						
		B Johnson				*r′* Cousin		
Year	Field	20s	80s	90s	180s	30s	80s	120s
2013	#1	-	169	-	-	-	169	-
	#2	-	174	-	-	-	174	-
	#3	-	173	-	-	-	170	-
	#4	-	174	-	-	-	174	-
2014	#1	78	-	-	78	-	-	78
	#2	78	-	-	78	-	-	78
	#3	78	-	-	78	-	-	78
	#4	57	-	-	57	-	-	57
	#5	54	-	-	54	-	-	54
	#6	54	-	-	54	-	-	54
2015	#1	-	-	88	-	85	-	-
	#2	-	-	61	-	61	-	-
	#3	-	-	61	-	63	-	-
	#4	-	-	66	-	63	-	-

Table 4.2: Number of images collected from STELLA 1, sorted by filter and exposure time.

		N° of LCs						
		B Johnson				*r′* Cousin		
Year	Field	20s	80s	90s	180s	30s	80s	120s
2013	#1	-	288	-	-	-	444	-
	#2	-	255	-	-	-	426	-
	#3	-	303	-	-	-	476	-
	#4	-	269	-	-	-	432	-
2014	#1	115	-	-	210	-	-	299
	#2	116	-	-	219	-	-	303
	#3	139	-	-	240	-	-	368
	#4	137	-	-	258	-	-	340
	#5	126	-	-	256	-	-	344
	#6	140	-	-	231	-	-	327
2015	#1	-	-	233	-	284	-	-
	#2	-	-	196	-	262	-	-
	#3	-	-	229	-	264	-	-
	#4	-	-	199	-	263	-	-

Table 4.3: Number of LCs extracted from STELLA 1, sorted by filter and exposure time.

The scientific images were corrected by bias, sky flat and dark images by the pipeline of STELLA project (Weber, Granzer & Strassmeier 2012). Then, I extracted the LCs of all the stars inside the field of view, using the `SExtractor` software (Bertin & Arnouts 1996), based on aperture photometry. The photometric apertures were 25" wide.

4.2 Data analysis

The raw LCs were corrected for systematic errors ("detrending") before any further analysis. These systematics are also known as "red noise" (Pont, Zucker & Queloz 2006). I applied three different detrending algorithms: SYSREM (Tamuz, Mazeh & Zucker 2005), and Trend Filtering Algorithm (TFA; Kovács, Bakos & Noyes 2005) for the SuperWASP dataset, and the algorithm described by Nascimbeni et al. (2014) for the STELLA dataset.

4.2.1 SYSREM

The SYSREM algorithm was adopted by the SuperWASP team from the beginning (Collier Cameron et al. 2007). This method identifies the general trend inside LCs as a function of external parameters, such as airmass (Tamuz, Mazeh & Zucker 2005). SYSREM subtracts this trend from the LCs, after weighting it with colour-dependent parameters (see section 2.2).

During the SYSREM detrending in SuperWASP LCs, the operation failed in some data points, due to absence of good measurements of external parameters. I clipped these uncorrected points from the LCs before following variability analysis. After this operations, cameras 103, 143 and 148 were ignored, because of insufficient temporal sample for the following variability search.

4.2.2 Trend Filtering Algorithm (TFA)

The TFA algorithm (Kovács, Bakos & Noyes 2005) is based on a set of stable reference stars in the field of view of the detector. These stars must cover as better as possible the range of magnitude of all the analysed stars, to build an empirical model of the systematic trend for each single star in the sample. This empirical model is assemble as a linear combination of the reference LCs contributions (see section 2.3).

In the following analysis, I implemented two type of TFA variants: a "global" TFA method (in other words, the standard TFA method, following Kovács, Bakos & Noyes (2005)) and a "local" TFA method (that I hereafter call Local Trend Filtering Algorithm, LTFA).

Standard TFA

In the standard TFA framework, I selected a common set of reference LCs for each camera, by analysing the distribution of the rms of the LCs in function of the instrumental magnitude (see figure 4.2).
First I selected only LCs with a temporal coverage more than 95% of the total observation baseline coverage of each camera. Then, I further restricted the sample by selecting 50 LCs below the 20^{th} percentile of the rms distribution as a function of the mean magnitude. The selection of only 50 LCs is required to avoid an over-fit, i.e., to avoid suppressing a real astrophysical signal (Kovács, Bakos & Noyes 2005).

In most cases, after the standard TFA correction, the LCs with too few data points were flattened. The cause is the small temporal range covered by the camera (e.g. camera 103 or camera 148, with a few tens of points per night), that does not allow me to recover a general trend to subtract to each target LCs. For this reason, all the LCs with less than 100 points were

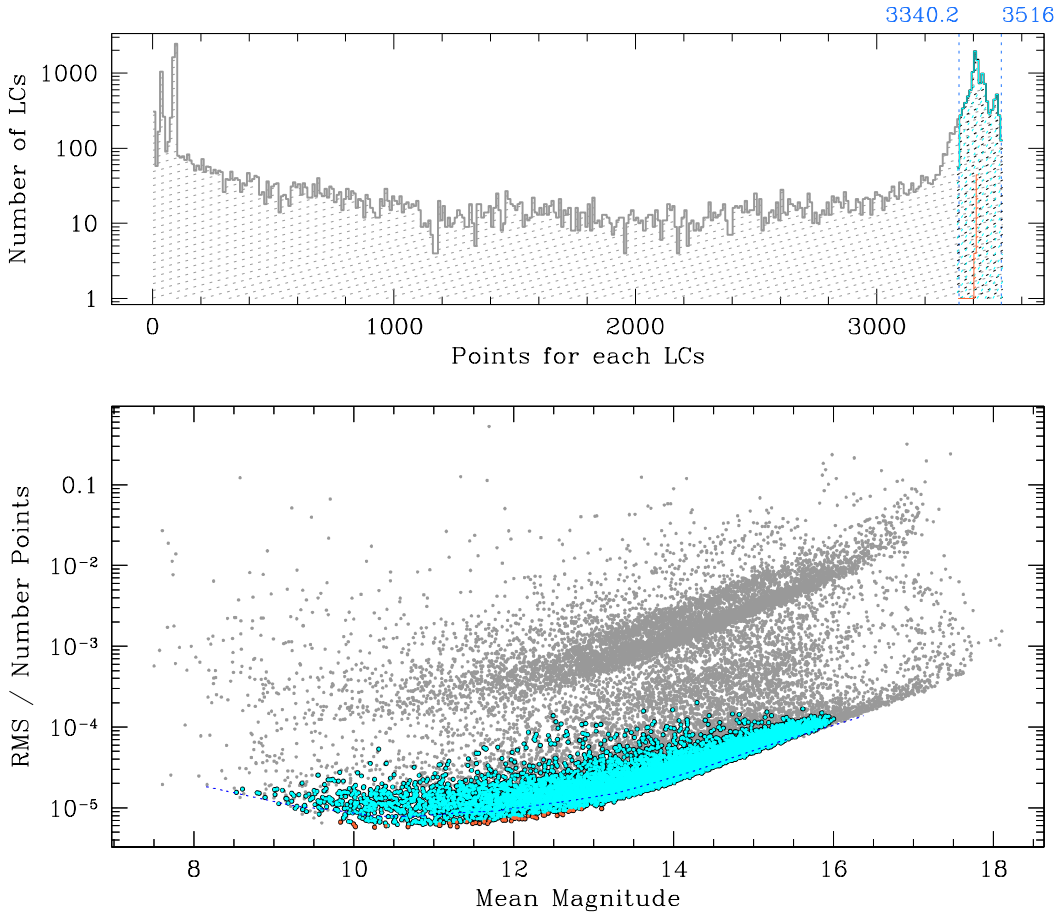

Figure 4.2: *Upper panel* histogram of number of data points per LC. I marked with a vertical line at 3340 (95^{th} percentile) the threshold set to select the reference LCs.
Bottom plot: the distribution of the rms as a function of the mean magnitude, used to select the 50 best stars as references. The blue dotted line marks the 20^{th} percentile of the rms distribution when considering only LCs with an high temporal coverage. Cyan points are all the LCs with at least 95% of the observation temporal range covered. Orange points are the 50 selected reference LCs with the best rms values.

discarded before the following analysis. In this sense, I clipped all the data points from camera 103, 143 and 148.

Local Trend Filtering Algorithm (LTFA)

In this second step, all the LCs corrected by the standard TFA method and with a rms less then the 68th percentile of the rms distribution were put inside the reference set. The only requirement was that the selected LCs cover at least 50% of the total observation baseline of each camera (see figure 4.3).

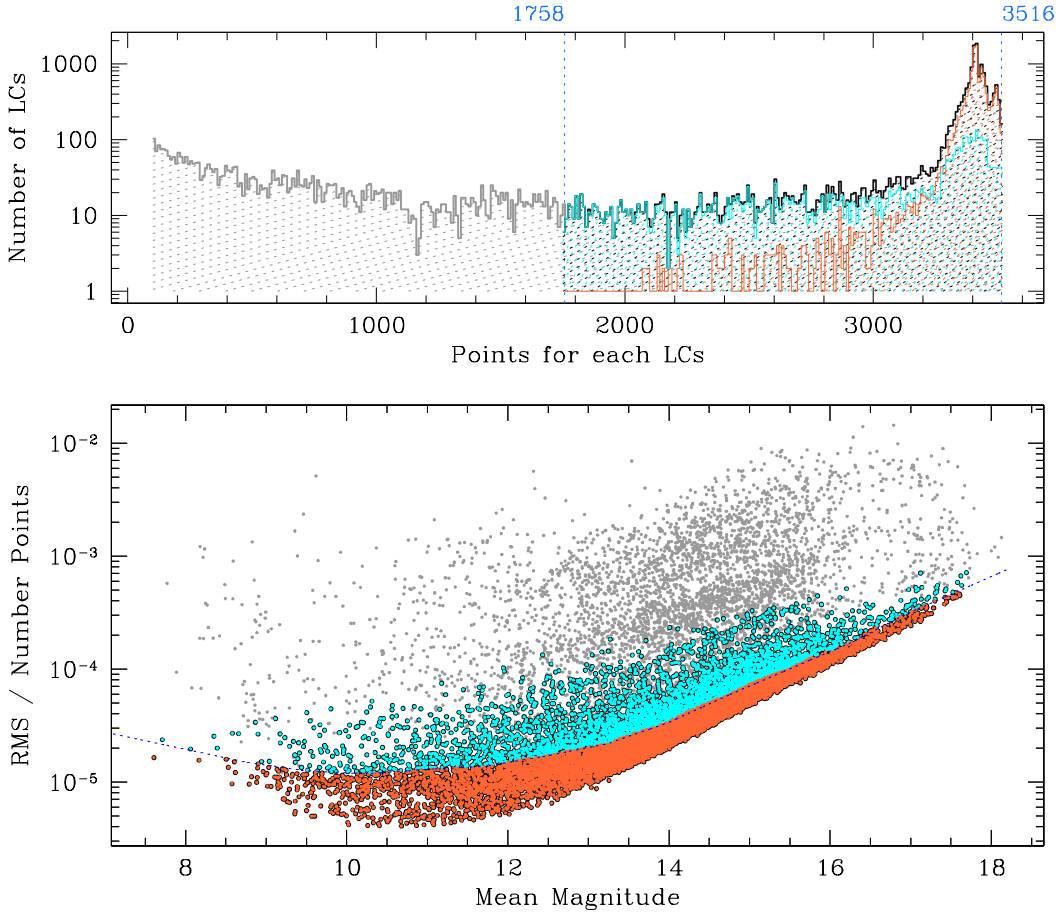

Figure 4.3: *Upper panel*: histogram of number of data points per LC. I marked with a vertical line at 1756 (50th percentile) the threshold set to select the reference LCs. The black histogram stresses the LCs taken into account in temporal coverage selection.
Bottom plot: the distribution of the rms as a function of the mean magnitude. The blue dotted line marks the 68.27th percentile of the rms distribution when considering only LCs with a good temporal coverage. All the LCs with at least 50% of the observation temporal range covered, but not selected as references, are indicated in cyan colour. The selected reference LCs are indicated in orange colour.

From this initial reference set of LCs was selected different subsets tailored on each target. I

applied a weighting scheme, following partially the approach of Nascimbeni et al. (2014):

$$D_{\rm ij} = \begin{cases} 0 & \text{if } r_{\rm ij} < r_{\rm I} \\ 1 & \text{if } r_{\rm I} \leq r_{\rm ij} < r_{\rm S} \\ \exp\left[-\left(\frac{r_{\rm ij}-r_{\rm S}}{r_{\rm E}-r_{\rm S}}\right)^2\right] & \text{if } r_{\rm ij} \geq r_{\rm S} \end{cases} \tag{4.1}$$

$$M_{\rm ij} = \begin{cases} 1 & \text{if } m_{\rm ij} < m_{\rm S} \\ \exp\left[-\left(\frac{m_{\rm ij}-m_{\rm S}}{m_{\rm E}-m_{\rm S}}\right)^2\right] & \text{if } m_{\rm ij} \geq m_{\rm S} \end{cases} \tag{4.2}$$

$$T_{\rm ij} = \begin{cases} 0 & \text{if } N_{\rm ij}^{time} < N_{\rm I}^{time} \\ 1 & \text{if } N_{\rm ij}^{time} \geq N_{\rm I}^{time} \end{cases} \tag{4.3}$$

where (4.1) is the weight based on the distance on the sky between the $j^{\rm th}$ reference and $i^{\rm th}$ target star, (4.2) is the weight based on the difference in magnitude between the $j^{\rm th}$ reference and $i^{\rm th}$ target star, and (4.3) is the weight based on the temporal coverage of the $j^{\rm th}$ reference LC with respect to the temporal coverage of each $i^{\rm th}$ target LC. The parameters $r_{\rm ij}$ and $m_{\rm ij}$ are, respectively, the distance on the sky and the modulus of the difference in magnitude between the $i^{\rm th}$ target star and the $j^{\rm th}$ reference star. The values $r_{\rm I}$, $r_{\rm S}$ and $m_{\rm S}$ are, free parameters to be set empirically. A null factor is given for $r_{\rm ij}$ less than $r_{\rm I}$, to avoid to use reference stars too close to the target, i.e. stars which could contaminate the target flux. $r_{\rm E}$ and $m_{\rm E}$ are the radii which define the scale distance for the $D_{\rm ij}$ and $M_{\rm ij}$ weights, respectively. Unlike Nascimbeni et al. (2014, see section 2.4), the match between the temporal coverage of the reference LCs and the temporal coverage of each target LC is taken into account. The weight $T_{\rm ij}$ depend on parameter $N_{\rm I}^{time}$, giving unitary weight for the $j^{\rm th}$ reference LCs that covers more than $N_{\rm I}^{time}$ data points of $i^{\rm th}$ target star, and zero otherwise.
These weights are combined to obtain the overall weight for each pair of target and reference stars:

$$W_{\rm ij} = D_{\rm ij} \cdot M_{\rm ij} \cdot T_{\rm ij} \tag{4.4}$$

The rms of the residual distribution of the differential LCs is not taken into account in the LTFA method as a separate weight, because the TFA method already weights the different reference LC contributions into the reference trend used to detrend target LCs.

For each $i^{\rm th}$ target star, the 50 reference LCs with the highest $W_{\rm ij}$ form the reference subsample to be used for the TFA correction. In other words, the LTFA is a particular application of the TFA method, that exploits the best subsample of reference LCs to detrend each target LC.

In the case of M44, from SuperWASP, I found that the parameters that gave the best local detrend with the LTFA method are $r_{\rm I} = 4.56$ arcmin (~ 20 px), $r_{\rm S} = 45.6$ arcmin (~ 200 px), $r_{\rm E} = 114,18$ arcmin (~ 500 px), $m_{\rm S} = 1$ mag, $m_{\rm E} = 1.75$ mag, and $N_{\rm I}^{time} = 100$ pts.

4.2.3 DeTrendy

To detrend the STELLA 1 dataset, which consists of a small number of photometric measures spread over large temporal ranges, I applied the algorithm described in Nascimbeni et al. (2014) and here called "DeTrendy". As already explained in section 2.4, this method first considers a global zero point approach, using the same sample of reference stars to correct all the LCs, and then an additional local zero point detrend.

At the global detrend stage, all the LCs are normalised and combined through a median to build a general trend, to be subtracted from each extracted LC (see equation 2.8).

At the local detrend stage, only a subset of the best reference stars is selected, based on three separate weights: the 68.27^{th} percentile of the residual distribution of the differential LCs, the distance over the field of view, and the difference in magnitude between the i^{th} target star and j^{th} reference star (see equation 2.13). The 68.27^{th} percentile is computed on the global corrected LCs. Only the 50 LCs with the highest weight were included in the subsample of reference LCs. In the local zero point approach, after some iterations, I set $r_{\text{I}} = 20$ px, $r_{\text{S}} = 200$ px, $r_{\text{E}} = 500$ px, $m_{\text{S}} = 1$, and $m_{\text{E}} = 1.75$. The local trend is a weighted mean, for each temporal instant, of the 50 best reference LC magnitudes, after being normalised by their own LC median magnitude (see equation 2.15).

During the following search for variability, the global and local zero point detrend were compared: the best correction between the two was adopted for the analysis.

4.3 Analysis of variability

The analysis of variability is divided into three main steps: preliminary conditioning, search for variability and selection of the LCs with the highest probability of being genuine variable stars.

4.3.1 Preliminary conditioning

After the systematic correction, the detrended LCs, still show outliers which could harm the variability search and must be clipped. Following a procedure that is similar to that described in Hartman et al. (2008), two cleaning passages were done. First I computed the median of each LC and I clipped all the points that were 10 σ outliers. This is to remove transient phenomena that are not intrinsic to the star, such as cosmic rays or satellite tracks. In a second step, I normalised all the LCs to their median magnitude. For each temporal instant, I computed the median of all the residuals, deriving a general trend from all the LCs, from which the 3 σ outliers were rejected. These instants were rejected because when common outliers are shared by different LCs, this is usually due to systematic errors not completely corrected.
After these two passages, I changed the errors which are lower than 10^{-4} with the 68.27^{th} percentile of the LC error distribution. This procedure was done to not assign an excessive weight to these points in the variability analysis. Secondly, I clipped all the points with errors 10 σ larger than the median one, usually due to bad weather or instrumental problems.
After all these clipping procedures, only LCs with at least 20 points were kept for the following analysis.

Next I split the LCs into different seasons, having a gap between them of at least $\sim$100 days. This resulted in six separate seasons for SuperWASP (see figure 4.4), whereas there are already three different campaigns for STELLA1. The individual season were analysed to search for short-term variability, which can change phase or amplitude from one season to the next; the full LCs were also analysed to search for long-term variability.
Again I kept only the LCs with at least 20 points on each individual season.

Before the next stage, I converted the time of all the LCs from Julian Date (JD) in Coordinated Universal Time (UTC) standard to Barycentric Julian Date (BJD) in Barycentric Dynamical Time (TDB) standard, to provide consistency and reliability over long temporal baselines (Eastman, Siverd & Gaudi 2010).

4.3.2 Search for variability

Three methods were used to search for variability: the Generalised Lomb Scargle algorithm (GLS), an improvement of the Lomb Scargle method (Lomb 1976; Scargle 1982), produced by

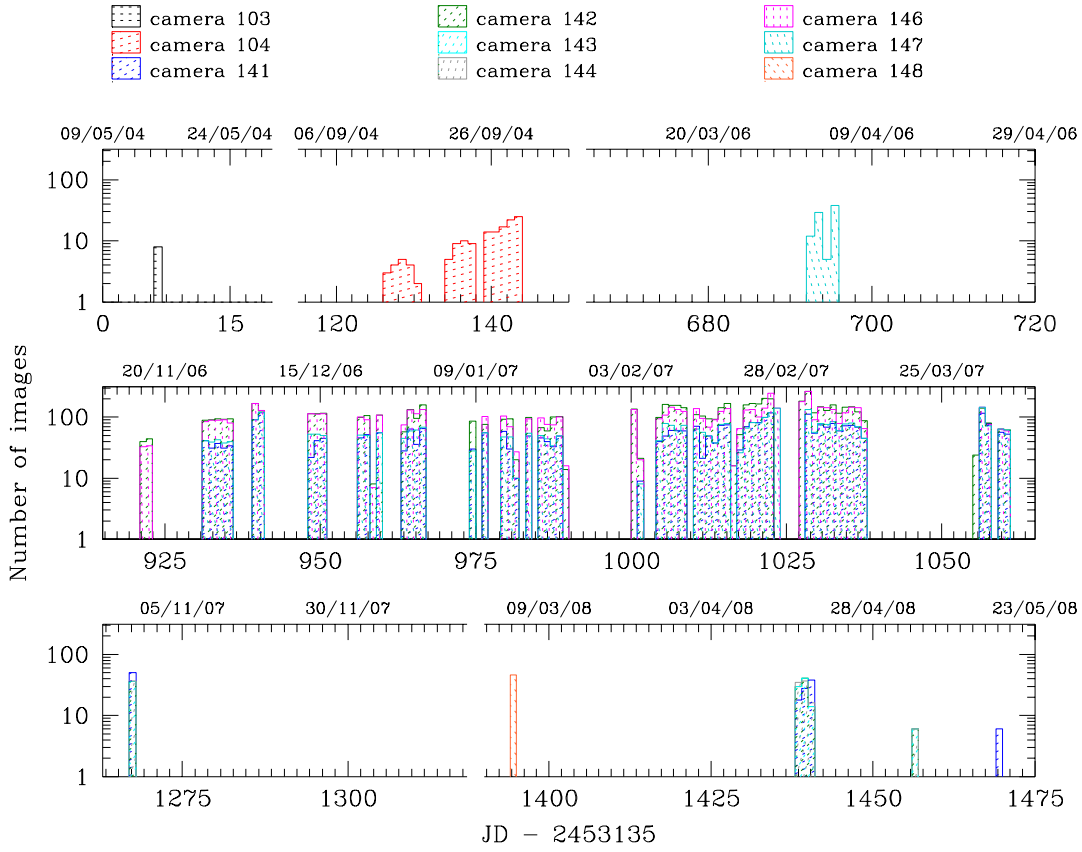

Figure 4.4: Histograms of the number of images per day taken by each SuperWASP camera. The IDs of the corresponding SuperWASP camera are colour-coded.

Zechmeister & Kürster (2009), effective to search for sinusoidal variability (for more information, see section 3.2); the Analysis of Variance (AoV) algorithm implemented by Schwarzenberg-Czerny (1989) and further developed by Devor (2005), sensitive to generic periodic features, without assuming a particular waveform (for more information, see section 3.3); the Box-fitting Least Squares algorithm (BLS), implemented by Kovács, Zucker & Mazeh (2002), which fits boxy functions on periodic eclipses, such as planetary transits (for more information, see section 3.4).

The temporal range analysed spans from 0.1 days up to the maximum temporal coverage of give dataset. In the case of SuperWASP, I separately analysed each camera/season combination or just only camera combination, while for STELLA1 I did not split the campaigns.

When applying GLS, two different procedures were used. In both of them, the temporal frequency resolution is given by the Nyquist frequency, computed from the mean of sampling frequencies of the non-uniform temporal sampling of the observations. The choice of this temporal frequency resolution aims at perfectly reconstructing a periodical signal: the Nyquist-Shannon sampling theorem says that a band-limited signal can be perfectly reconstructed from its non-uniform sampling if the average sampling rate satisfies the Nyquist condition (Marvasti 2001). In the first procedure, I split the temporal range analysed into subranges, one per order of

magnitude, multiplying the temporal frequency resolution by the same order of magnitude in each temporal subrange. In this way, it is possible to better sample the GLS periodogram at lower frequencies. Within each temporal subrange, the method finds the 5 highest peaks in the periodogram.
In the second procedure, I analysed the all temporal range, without splitting into subranges, using the temporal frequency resolution as defined previously. I searched for the first 5 peaks, whitening the LC at each peak period and recomputing the periodogram before searching for the next peak, in order to search for additional signals hidden by stronger periodic signals.

I applied the same two procedures also using the AoV algorithm. This method of analysis splits the phased LCs into equal bins. For each sampled period, AoV computes the probability that the phased LC represents a variable. I set 8 as the default number of bins, as suggested by Devor (2005).
While applying the AoV algorithm, the temporal frequency resolution selected is the same as for GLS. Also, on each periodogram peak, AoV refines the result by scanning at a temporal frequency resolution 100 times finer than the previous scan.

During the BLS scan, I searched for the 5 highest peaks of BLS periodogram in SuperWASP, and the 2 highest peaks in STELLA1. I searched for boxy signal which spans 1% to 10% of the entire phased LCs. The periodogram was sampled on $7 \cdot 10^4$ frequencies. Each phased LC is split in 200 bins during the BLS search.

The SuperWASP LCs were analysed both as a whole time series, as splitted in seasons, while each season of the STELLA1 data were analysed separately.

4.3.3 Selection of the best candidates

A subset of LCs were preselected as candidate variable stars before the final visual classification.

First of all, on the GLS and AoV results, I discarded stars with a scatter smaller than 68.27^{th} percentile of the corresponding magnitude bin, in order to remove LCs with weak periodic signal. Also, all the LCs of saturated stars were clipped from the final set. A further clipping was done to discard the LCs with less than 100 points, in the case of SuperWASP, or less than 20 points, in the case of STELLA1. These last selections were needed because a sparse temporal sampling can introduce spurious periodic signals.

On the BLS results, instead, I discarded saturated stars and LCs with less than a minimum number of data points, but did not apply any clip on the error distribution, because transits are usually recorded on a small number of points, which are fragile against data clipping.

After the selections in error distribution, magnitude and number of data points, further selections of good candidates were done depending on the algorithm applied. A formal False Alarm Probability (from here on FAP) value was evaluated to select candidate variable stars. For the AoV method, the FAP value is given by the Θ metric, described by Schwarzenberg-Czerny (1989) and explained in section 3.3: the higher the Θ metric, the higher the probability of having found a genuine variable. For the GLS, instead, the probability is expressed by log(FAP), the logarithm of the formal FAP defined in Horne & Baliunas (1986, see section 3.2): again, the smaller the log(FAP), the higher the probability. Finally, for the BLS method, the FAP value is given by a signal-to-pink-noise diagnostic, following the definition of Hartman et al. (2008, 2009, see section 3.4): the higher the signal-to-pink-noise, the higher the probability.

The actual selection was done as follows. A first constrain on the FAP values was given by selecting stars over the 97^{th} percentile of the FAP distribution (the limit is indicated with the label [1] in figure 4.6). All the detected periods with FAP lower (in modulus) than this limit were rejected from the final sample.
A second constrain on FAP values was applied on the histogram of the detected periods (the limit

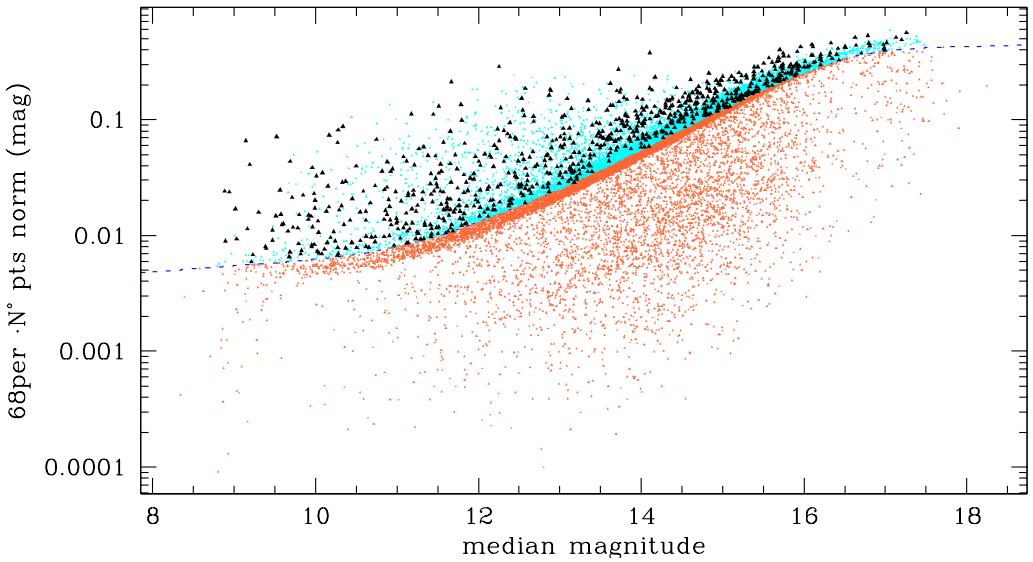

Figure 4.5: Selection of light curves according to their photometric scatter, as a function of median magnitude (GLS and AoV). Cyan points are all the LCs with a standard deviation over the 68.27$^{\text{th}}$ percentile threshold. Orange points are the discarded LCs. Black points are the final LCs kept as candidate variable stars, after the additional selection FAP (see figure 4.6).

is indicated with the label [2] in figure 4.6). I discarded all the light curves within period bins whose frequency exceeds by 5σ or more the local value, estimated as the median over the 100 bins centred on the given period. In this way, recurrent periods due to atmospheric or instrumental effects (such as the 0.997-day sideral period) are discarded.
The previous cut is not applied when the FAP of a given LC is more than 10 times over the value at the 97$^{\text{th}}$ percentile (the limit is indicated with the label [3] in figure 4.6). This is to preserve genuine, high-confidence variables which by chance could be misidentified as false positives.

After having selected the final sample of good candidate variables, I performed a visual check. To pinpoint if a LC was variable or not, I examined the 68.27$^{\text{th}}$ percentile of the data points as a benchmark: if the best-fit model had a Δmag between minimum and maximum equal to $\sim$1.5 times the σ dispersion, then this LC is considered a genuine variable. Only after a visual check of the phased LC, it was possible to say if the dispersion was due to real variability or to noise.

Selected all the LCs with variability signals, I analysed the position of each variable in the field of view. If one variable star were near other variables, I checked the variability periods of nearby stars. If the periodicity of close stars was approximately equal or a multiple of the target periodicity, then I selected only one star as real variable, throw out of the final list the other close stars. The selected star was either that one with the highest probability to be variable (following FAP values) or, when the FAPs are approximately the same, the brightest one.

4.4 Results

Considering both STELLA1 campaigns and SuperWASP database, I analysed a catalogue of 31604 stars. Of this sample, 27872 stars were observed in the analysed 6 cameras of SuperWASP

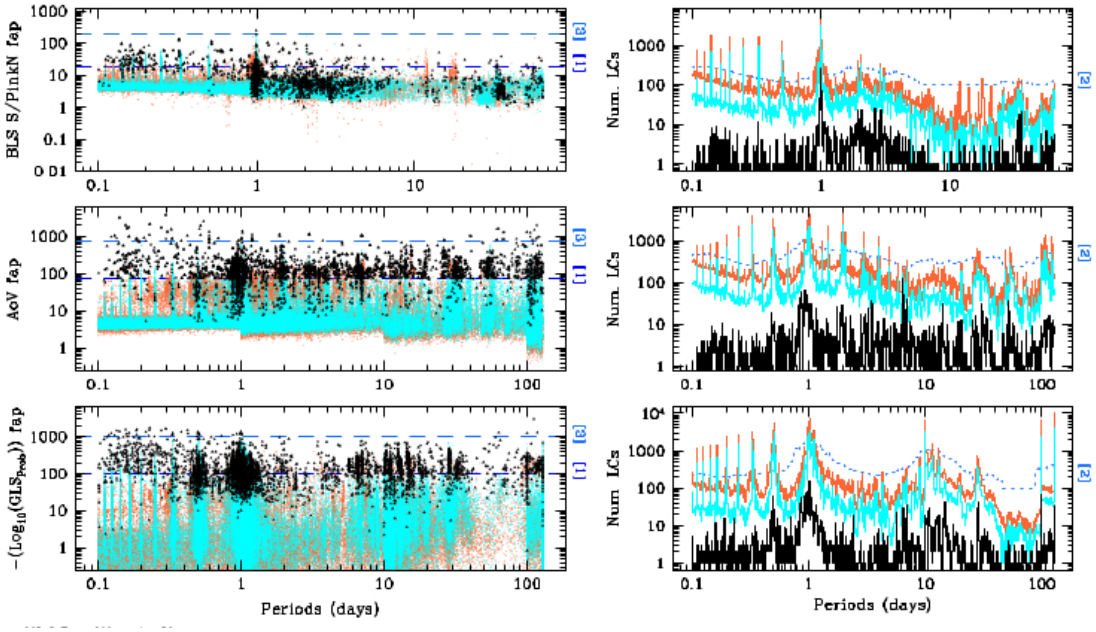

Figure 4.6: *Left panels*: FAP distributions for each variability search method (BLS, AoV and GLS, from the top to the bottom).
Right panels: histograms of detected period. The labels [1] [2] and [3] indicates the 1st, 2nd and 3rd criteria applied to select the best candidates. The colours are the same of those in figure 4.5.

(ID 104, ID 141, ID 142, ID 144, ID 146, ID 147), 3858 stars were followed in at least one of the three campaigns carried out at STELLA1 telescope, and 126 were detected in both of the facilities. The number of detected variable stars from this work were 484. Considering all the variables already discovered in literature, according to the catalogues of Agüeros et al. (2011), Delorme et al. (2011), Douglas et al. (2014), *General Catalogue of Variable Stars* (GCVS; Samus, Durlevich & et al. 2009), Kovács et al. (2014), Mermilliod, Mayor & Udry (2009), *New Suspected Variables* (NVS; Samus, Durlevich & et al. 2009), Pepper et al. (2008), Scholz et al. (2011), and *AAVSO International Variable Star Index* (VSX; Watson 2006), I found that 185 are already discovered variables, whereas 299 are new. Other variables from the literature were not detected by my analysis, due to a too low number of data points per some LCs, or being stars too bright or too faint for the SuperWASP/STELLA dynamic range. In figure 4.7 the CMD of the studied stellar field is shown.

Among the different detected variables, many eclipsing binary and rotational variables were detected. In table 4.4 I show the exact numbers of each kind of detected variable.

4.4.1 M44 members

According to the catalogue of Kraus & Hillenbrand (2007), the number of M44 stars in common with my master catalogue are 137. The detected variable stars inside M44 were, instead, 61. All these variable stars were already discovered in previous articles or projects. Some examples are shown in figure 4.8.

In particular, by measuring the rotational modulation of M44 stars, Delorme et al. (2011)

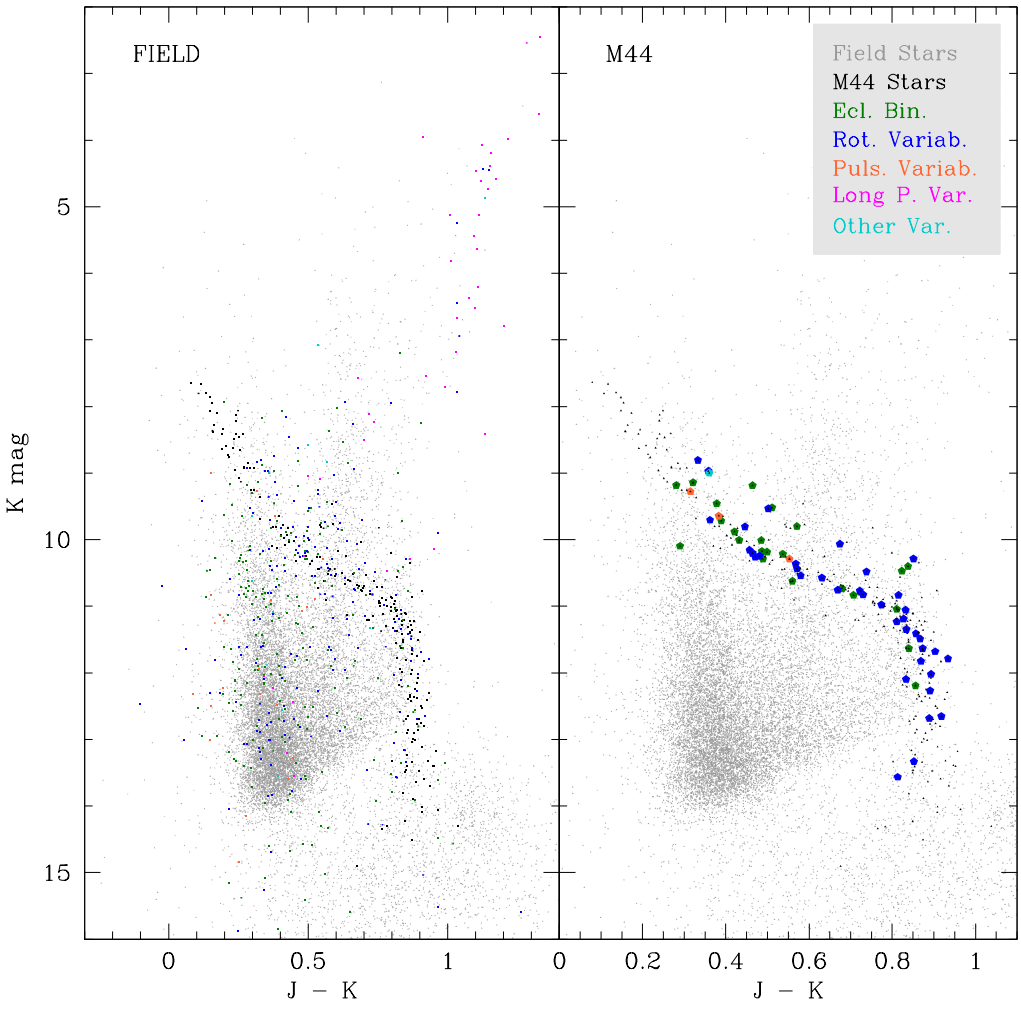

Figure 4.7: *Left panels*: Colour Magnitude Diagram (CMD) with all the stars in the different FoVs of STELLA1 and SuperWASP.
Right panels: zoomed CMD on stars in M44. Variable stars in this panel are only M44 members (following catalogue of Kraus & Hillenbrand 2007).
All the colours are explained in the legend inside second panel. There are eclipsing binaries (in green), rotational variables (in blue), pulsating variables, considering δScuti, RR Lyrae and β Chephei variables (in orange), long periodic variables (in magenta), and other kinds of variability (in marine).

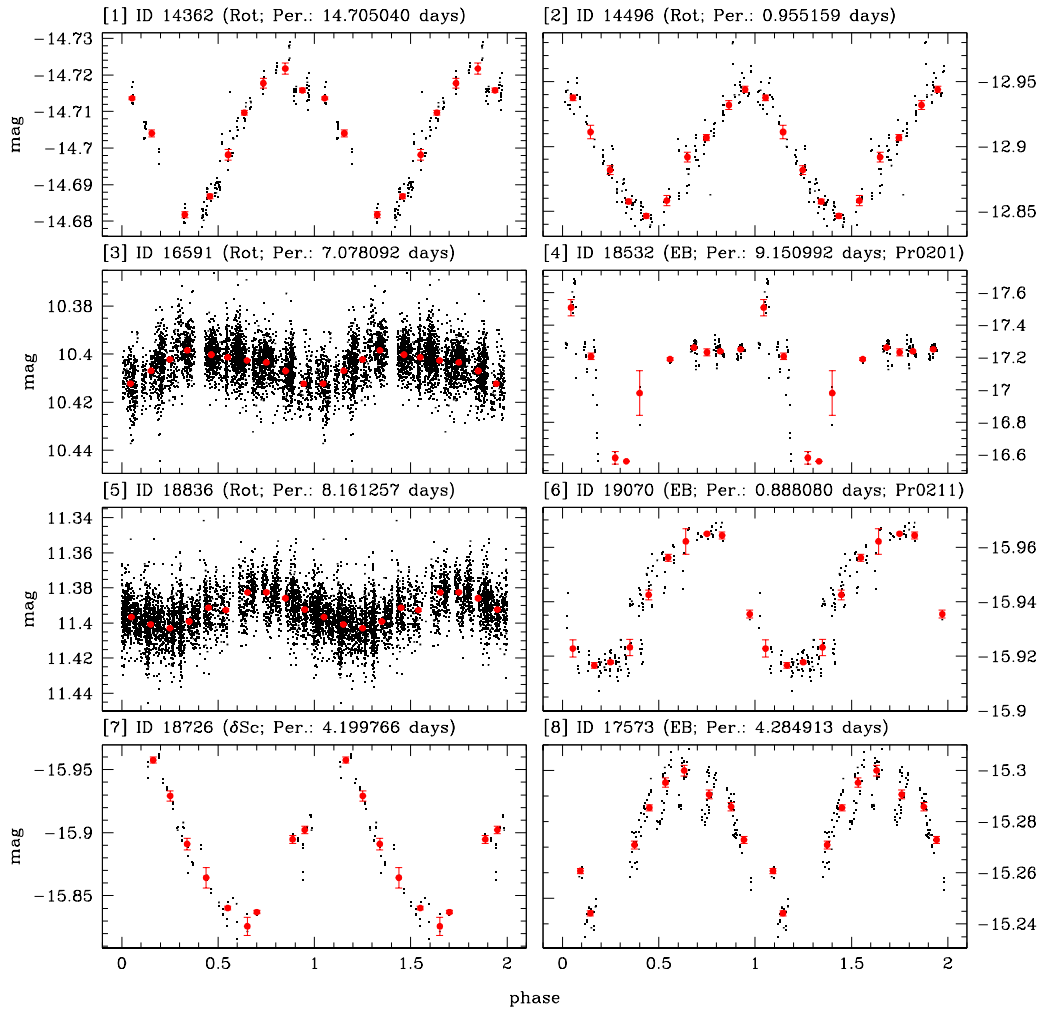

Figure 4.8: Phased LCs of some variable stars, known members of M44. Light curves [3] and [5] are from SuperWASP, the remaining LCs are from STELLA1. The variability type and detected period are plotted. Light curves [4] and [6] are from the two stars having detected planets in M44 (Quinn et al. 2012; Malavolta et al. 2016)

Type of variable	All variables	M44 variables	New variables
Eclipsing Binary	212	20	123
Rotational Var.	193	37	129
δScuti	17	3	12
RR Lyrae	4	0	1
β Chephei	3	0	1
Long Period Var.	43	0	23
Other Variables	12	1	10
Total Variables	484	61	299

Table 4.4: Summary of the detected variable stars, splitted in the different kind of variability that I identified during variable analysis by eye. The M44 members are identified according to the catalogue of Kraus & Hillenbrand (2007). The new variables are not members of M44. Also the total number of variables is indicated.

had analysed the gyrochronological relation between the period of these particular variable stars and their colour (blue dots in figure 4.9). I also tried to reconstruct the relation obtained by Delorme et al. (2011). The principal problem is the estimate of the corrected LC periodicity, that could be a multiple of the detected period. Anyway, there is a good agreement between my distribution and Delorme et al. distribution (indicated with open black circle in figure 4.9).

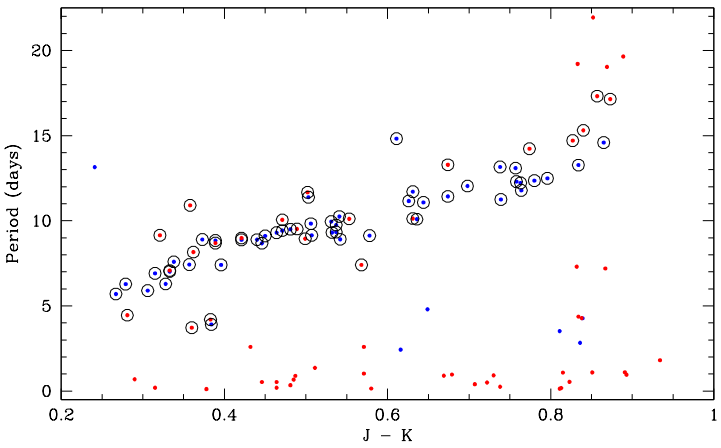

Figure 4.9: Period vs. (J - K) colour (from 2MASS) gyrochronological relation from Delorme et al. (2011) (blue dots) and from the present work (red dots). The two data sets are in good agreement. Data points are selected according to the procedure explained in Delorme et al. (2011).

4.4.2 Field stars

Despite the lack of new variable detection inside M44 members, I detected 299 new variables inside the huge field of view used in this analysis. Some examples of new variable detections are

shown in figure 4.10.

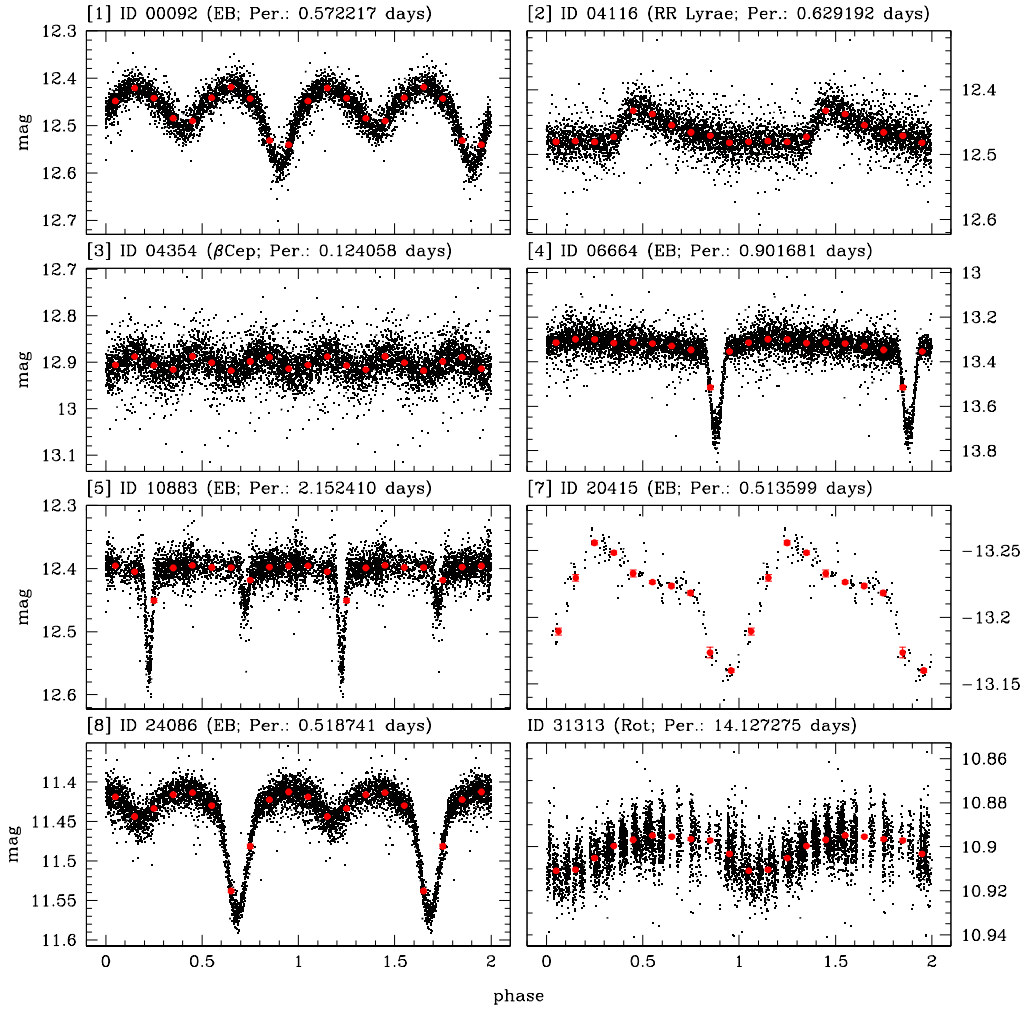

Figure 4.10: LCs in phase of some variable stars, not members of M44 and new variability detection.

4.5 Conclusions

A photometric variability study of M44 was carried out using two different facilities: SuperWASP and STELLA1. A total of 31604 stars were analysed, using more than 100,000 light curves extracted with aperture photometry algorithms. I used different algorithms to detrend the LCs, using already published ones (SYSREM and TFA) and implementing a new one (LTFA). The LTFA performed better on most light curves.

After the detrend, I used three algorithms for the search for variability and transient: the Generalised Lomb Scargle (GLS), the Analysis of Variance (AoV) and the Box-fitting Least Squares (BLS) algorithms. Matching the results from both facilities, I detected 484 variables: 185 are already discovered variables, the remaining 299 are previously unpublished variables. I detect 61 variables among the M44 members (all already in literature), and a comparison with the period vs. colour relation of Delorme et al. (2011) was done. All the new variables are not members of M44. Overall, I detected: 212 eclipsing binary (123 are new), 193 rotational variables (129 are new), 17 δScuti variables (12 are new), 4 RR Lyrae (1 is new), 3 β Chephei (1 is new), 43 long period variables (23 are new), and 12 other kind of variables (10 are new).

Chapter 5

Photometric observations in Open Cluster NGC 752

The open cluster NGC 752 (l,b = 137.1251°, −23.2542°; α,δ = 01^h 57^m 41^s, +37° 47' 06"; Kharchenko et al. 2013), is at ∼458 pc from the Sun and is ∼1.38 Gyr old (Kharchenko et al. 2013). The size of its core radius is 1.7 pc (Piskunov et al. 2007). Only a few works were published about stellar variability within this open cluster (OC), mainly spectroscopically (see Pribulla et al. 2009; Mermilliod, Mayor & Udry 2009, and references within). In order to study this OC, I analysed the data taken from the SuperWASP public archive.

5.1 SuperWASP - observations

For a detailed description of the observing setup of SuperWASP project, see paragraph 4.1.1.

The observations of NGC 752 span ∼3.5 years, between 2004, June 26^{th} and 2008, July 23^{th}. The NGC 752 stars were selected from the SuperWASP public archive according to the catalogues of Daniel et al. (1994), Mermilliod, Mayor & Udry (2009) and Bartašiūtė et al. (2011), and including all the stars with a high membership probability, evaluated from proper motions. I also selected all the field stars within 1° from the cluster centre: the input sample is made of 2546 stars, of which 154 are cluster members identified as above. The light curves (LCs) were grouped according to the camera and the filter used. I obtained LCs from 1 camera without filters and from 6 cameras in the visual passband. Overall, I analysed 16304 LCs (see table 5.1).

5.2 Data reduction

The raw LCs were detrended before any kind of periodicity analysis, to eliminate the red noise, that is, in general, not negligible (Pont, Zucker & Queloz 2006). As already done in detrend phase of M44 LCs (see section 4.2), two different methods of detrending were applied: one based on the SYSREM algorithm (Tamuz, Mazeh & Zucker 2005), the other on the Trend Filtering Algorithm (TFA; Kovács, Bakos & Noyes 2005).

5.2.1 SYSREM

First of the two detrend methods used during the analysis of SuperWASP LCs, the SYSREM algorithm was adopted by the research team of SuperWASP project from the beginning (Collier

Camera ID	Number of stars		Number of data points		Filter
	All	NGC 752	All	NGC 752	
#105	2419	172	2334	2334	None
#141	2452	173	3707	3699	Visual
#142	2101	167	3794	3794	Visual
#145	2343	171	2739	2739	Visual
#146	2215	164	3350	3290	Visual
#147	2318	172	3416	3402	Visual
#148	2456	173	3084	3084	Visual
Total Stars	2456	173	11367	11362	

Table 5.1: Summary of my input stellar sample. The columns give: the number of field stars and NGC 752 members, the number of data points, and the filter. The total number of selected stars is indicated in the last row of the table, both from entire field of view and from NGC 752 selection (following Daniel et al. 1994).

Cameron et al. 2007). This method analyses the general trend inside LCs and generated by external parameters, such as airmass (Tamuz, Mazeh & Zucker 2005). SYSREM subtracts this trend from all the LCs, weighting out the trend with colour-dependent parameters, such as the colour itself of the star (see section 2.2). With these operations, the star LCs are cleaned by magnitude variations created by external phenomena, such as, for example, variation of altitude of the field observed or variation of weather conditions, with consequent variation of depth of atmospheric layers and a variation of absorption of the star light.

In this detrend operation in SuperWASP LCs, it was impossible to cover all the temporal coverage of the LCs and in some points the SYSREM correction was not done. I clipped those points from all the LCs before following variability analysis. Despite M44, in NGC 752 no camera was clipped, because the number of points, after the clip of uncorrected one, was maintained good.

5.2.2 Trend Filtering Algorithm (TFA)

The Trend Filtering Algorithm (TFA; Kovács, Bakos & Noyes 2005) was the second method that I used for the detrend of LCs of SuperWASP archive. This algorithm uses a set of stablest star LCs in the field of view of the detector. These stars have to cover as better as possible the range of magnitude of all the stars analysed, to create an empirical model for each single star in the sample. This empirical model is created by a linear combination of the reference LCs contributions (see section 2.3).

During the analysis of SuperWASP LCs, as done in M44 case, also in NGC 752 case the "global" TFA (in other words, the standard application of the TFA method, following Kovács, Bakos & Noyes (2005)) and the Local Trend Filtering Algorithm (LTFA) methods were used.

Standard TFA

In the TFA correction, I selected a common set of reference LCs for each camera, using the distribution of the rms of the LCs in function of the mean magnitude.
The procedure is the same used in M44 case (see section 4.2.2). Each LC rms was weighted on the number of points collected in given LC. Only LCs with a temporal coverage more than 95%

of the total observation time coverage of each camera were taken into account for final selection. In this set of LCs, the best 50 LCs created the set of reference LCs for detrend operation. These reference LCs had the best rms value respect to the 20^{th} percentile of the rms distribution in function of the mean magnitude.

With a reference set of the best 50 LCs for each camera, I corrected all the LCs. In most cases, after this TFA correction, the LCs with a number too low of points were flattened. The cause would be the small temporal range covered by the camera, that does not allow to find a general trend to subtract to each target LCs, producing a trend that totally destroys any kind of signal. For this reason, all the LCs with less than 100 points were thrown out in the following operations.

Local Trend Filtering Algorithm (LTFA)

The corrected LCs, generated by TFA algorithm used in "global" mode, were taken into account to recreate a new set of reference LCs, to use with the LTFA method. Again, the rms distribution in function of the mean magnitude was used in this selection. In this case, all the LCs corrected by TFA method and with a rms less then the 68^{th} percentile of the rms distribution were put inside the reference set. The only imposed limitation was that the LCs selected covered at least 50% of the total observation coverage of each camera.

From this reference set of LCs was selected different subsets of reference LCs, one for each target. The creation of these subsamples of references was done using different weights, following partially the idea of Nascimbeni et al. (2014). The weights considered are generated by:

- the distance over the field of view between a j^{th} reference and the i^{th} target stars (see equation 4.1 in section 4.2.2);
- the difference in magnitude between a j^{th} reference and the i^{th} target stars (see equation 4.2 in section 4.2.2);
- the temporal coverage of a j^{th} reference LC respect to temporal coverage of the given i^{th} target LC (see equation 4.3 in section 4.2.2).

and the combination of these weights was used to select the best 50 reference LCs (see equation 4.4). This subsample was used for the creation of the empirical trend that was subtracted from the relative target LC.

In the case of NGC 752 dataset, obtained from SuperWASP archive, I used the same parameters in weight equations already used in case of M44 dataset: $r_{\text{I}} = 4.56$ arcmin (equal to ~ 20 px), $r_{\text{S}} = 45.6$ arcmin (equal to ~ 200 px), $r_{\text{E}} = 114,18$ arcmin (equal to ~ 500 px), $m_{\text{S}} = 1$ mag, $m_{\text{E}} = 1.75$ mag, and $N_{\text{I}}^{time} = 100$ pts.

5.3 Analysis of Variability

The analysis of variability followed the same steps of the M44 LCs analysis (see section 4.3). They are three in whole: preliminary processes to obtain a good LC dataset to analyse, the research of variability signals inside these LCs and the selection of the LCs with the highest probability to have real variability signals.

5.3.1 Preliminary processes

After the correction processes, the detrended LCs were subdued to different clipping operations, to remove unreliable measurements. Two clipping procedures were done on magnitude values and two on the magnitude errors (see section 4.3.1 for more information).

The first two clipping limits were at 10 σ from median magnitude of the singular LC and at 3 σ in normalised trend, given by median of the residuals of all the LCs. The first clip was done to remove transient phenomena, not intrinsic to the star. The second clip was done to reject outliers, due to systematic problems not completely corrected in detrend phases.
The other operations concerned error values under 10^{-4}, that is the order of the significant digit, and error values beyond 10 σ. The too low errors were changed with the 68.27^{th} percentile of the LC error distribution. The points with too high errors were clipped, because they were points bad measured.
After all these clipping operations, only the LCs with at least 20 points were kept in following operations.

Following procedure was to split the LCs into different campaigns, with a temporal gap from one campaign to another one of at least $\sim$100 days. At the end, 5 campaigns were selected. This splitting of the LCs was done to study kind of variability, such as rotational ones, that could vary in intensity in timescale of order of months or years. Anyway, the not splitted LC were also analysed, to search for long period variability.
After the splitting operations in different observation campaigns, only the LCs with at least 20 points were kept in following operations.

Before analysing variability and running the different algorithms, I converted the time of all the LCs from Julian Date (JD) in Coordinated Universal Time (UTC) standard to Barycentric Julian Date (BJD) in Barycentric Dynamical Time (TDB) standard, providing, with this standard, consistency and reliability on long temporal baselines (Eastman, Siverd & Gaudi 2010).

5.3.2 Research of variability

The LCs obtained from the preliminary processes of clipping and temporal splitting were analysed to search for variability. Following the procedure used in M44 case (see section 4.3.2), three methods were used for this research: the Generalised Lomb Scargle algorithm (GLS; Zechmeister & Kürster 2009; Lomb 1976; Scargle 1982, for more information, see section 3.2), the Analysis of Variance (AoV; Schwarzenberg-Czerny 1989; Devor 2005, for more information, see section 3.3) and the Box-fitting Least Squares algorithm (BLS; Kovács, Zucker & Mazeh 2002, for more information, see section 3.4).

The temporal range analysed was from 0.1 days until the maximum temporal coverage of give dataset of LCs. Each dataset analysed was created both per camera and per campaign or only per camera (without campaign splitting).

Using GLS algorithm, two different procedures were used. In both of these procedures, the temporal frequency resolution in which the variability was analysed is given by the Nyquist frequency, computed from mean of sampling frequencies of the non-uniform temporal sampling of the observations (following Nyquist-Shannon sampling theorem; Marvasti 2001).
In the first procedure, I divided the temporal range analysed into subranges, one per order of magnitude, multiplying the temporal frequency resolution by the same order of magnitude in each temporal subrange. In this way, it is possible to sample better the GLS periodogram at lower frequencies. In each temporal subrange, the method researches for the 5 highest peaks in the periodogram.
In the second procedure, I analysed all the temporal range, without splitting into subranges, using the temporal frequency resolution defined previously. I researched for the first 5 peaks,

whitening the LC at each peak period and recomputing the periodogram before searching for the next peak period, in order to search for signals hidden by stronger periodic signals.

I applied the same two different procedures also using AoV algorithm. This method of variability research requires a number of bins in which to divide the phased LCs. For each sampled period, a binned phased LC is created and the probability that the phased LC represents a variable is computed. I used the default number of 8 bins, considered a good value (Devor 2005).
In the application of the AoV algorithm, the temporal frequency resolution selected is the same already described in GLS. Also, around each periodogram peak, a fine-tuning with a temporal frequency resolution 100 times bigger than previous one is operated.

Using BLS algorithm, instead, I applied only one procedure: I analysed all the temporal range, researching the 5 highest peaks of BLS periodogram in SuperWASP datasets and the 2 highest peaks of BLS periodogram in STELLA 1 dataset. I researched for boxy signal that covers a portion included from 1% to 10% of the entire phased LCs. The periodogram was sampled into $(7 \cdot 10^4)$ frequencies. Each evaluated phased LC is divided in 200 bins, in order to sampled as better as possible even the searched minimum coverage for the boxy signal.

The three algorithms were run for all the datasets. Each camera set of LCs, splitted or not in campaigns, were analysed separately.

5.3.3 Selection of the best periodical LCs

After running the three algorithm for the variability research and before to begin with a periodicity evaluation, the star LCs were preselected for the visual final analysis.

Following the same line of reasoning used in M44 case (for more information, see section 4.3.3), the principal parameters taken into account for the preselection are:

- The LC standard deviation on the median magnitude (only for GLS and AoV algorithm);
- The saturation magnitude;
- The number of instant points in the LCs;
- The false alarm probability (FAP) of each variability research algorithm;
- The number of LCs in a histogram in function of the periodicity.

For GLS and AoV algorithms, the lower limitation in the standard deviation distribution in function of the median magnitude was due to the kind of variability researched (such as eruptive, pulsating or rotating variables, see introduction to chapter 3). As done in M44 case, also here the limit was at one sigma of the distribution. The limit in saturated magnitude was used to not analyse star LC that lose flux information during the monitoring. The limit in number of instant points (that was 100, like M44 case in SuperWASP) was used to exclude LC with a lacking temporal sampling, not useful to identify correctly a real variability signal.

For BLS algorithm, only limitations in saturation magnitude and in number of monitored instants were taken into account. No limitation in standard deviation distribution was applied, because of the kind variability that was researched, such as eclipsing binary or transiting planets, that are transiting phenomena that occur only in a small portion of the LC, leaving the most of the LC with a low standard deviation value.

The further selections in FAP and in the histogram of the number of LCs in function of the periodicity were applied to select the LCs with a good variability signal in each detection method. For the definition and more information about the FAP parameters used, see sections 3.2 for GLS algorithm, 3.3 for AoV algorithm and 3.4 for BLS algorithm.

The selection was done in three passages:

1. A first lower limit in FAP values was given at 97^{th} percentile of the FAP distribution, to exclude stars with low probability to be variables;

2. A second constrain was the maximum number of LCs with approximately the same period value (computing in the same way explained in section 4.3.3), to exclude all the periodicity due to systematic errors, such as instrumental and atmospheric artefacts;

3. A final step was the reinstatement of the LCs that were rejected with second constrain in histogram counts and that had a FAP at least 10 times higher than first lower limit in FAP, to consider LCs of stars with a very good spectral power inside the periodogram.

After having collect the final sample of LCs with good variability signals, a visual check was done. To pinpoint if a LC is variable or not, I used the 68.27^{th} percentile of the points distribution like benchmark: if the variability model has a Δmag between minimum and maximum equal to $\sim$1.5 times the σ dispersion, then this LC will be considered affected by intrinsic stellar activity. Only after a visual check of the phased LC, it was possible to say if the dispersion is due to real variability or due to noise.

5.4 Results

Using SuperWASP database, I analysed a catalogue of 2456 stars. The number of detected variable stars from this work were 68. Considering all the variables already discovered in literature, according to the catalogues of Drake et al. (2014), *General Catalogue of Variable Stars* (GCVS; Samus, Durlevich & et al. 2009), Mermilliod, Mayor & Udry (2009), *New Suspected Variables* (NVS; Samus, Durlevich & et al. 2009), Pribulla et al. (2009), and *AAVSO International Variable Star Index* (VSX; Watson 2006), I found that 22 are already discovered variables, whereas 46 are new. As in the case of M44, also for NGC 752 other variables from the literature were not detected by my analysis, due to a too low number of data points per some LCs, or being stars too bright or too faint for the SuperWASP dynamic range. In figure 5.1 the CMD of the studied stellar field is shown.

Among the different detected variables, many eclipsing binary and rotational variables were detected. In table 5.2 I show the exact numbers of each kind of detected variable.

Type of variable	All variables	NGC 752 variables	New variables
Eclipsing Binary	30	8	16 (1 in OC)
Rotational Var.	24	5	20 (1 in OC)
δScuti	6	2	4
Long Period Var.	7	1	5 (1 in OC)
Other Variables	1	0	1
Total Variables	68	16	46

Table 5.2: Summary of the detected variable stars, splitted in the different kind of variability that I identified during variable analysis by eye. The NGC 752 members are identified according to the catalogues of Daniel et al. (1994); Mermilliod, Mayor & Udry (2009); Bartašiūtė et al. (2011). The new variables are 46, and 3 are members of NGC 752. Also the total number of variables is indicated.

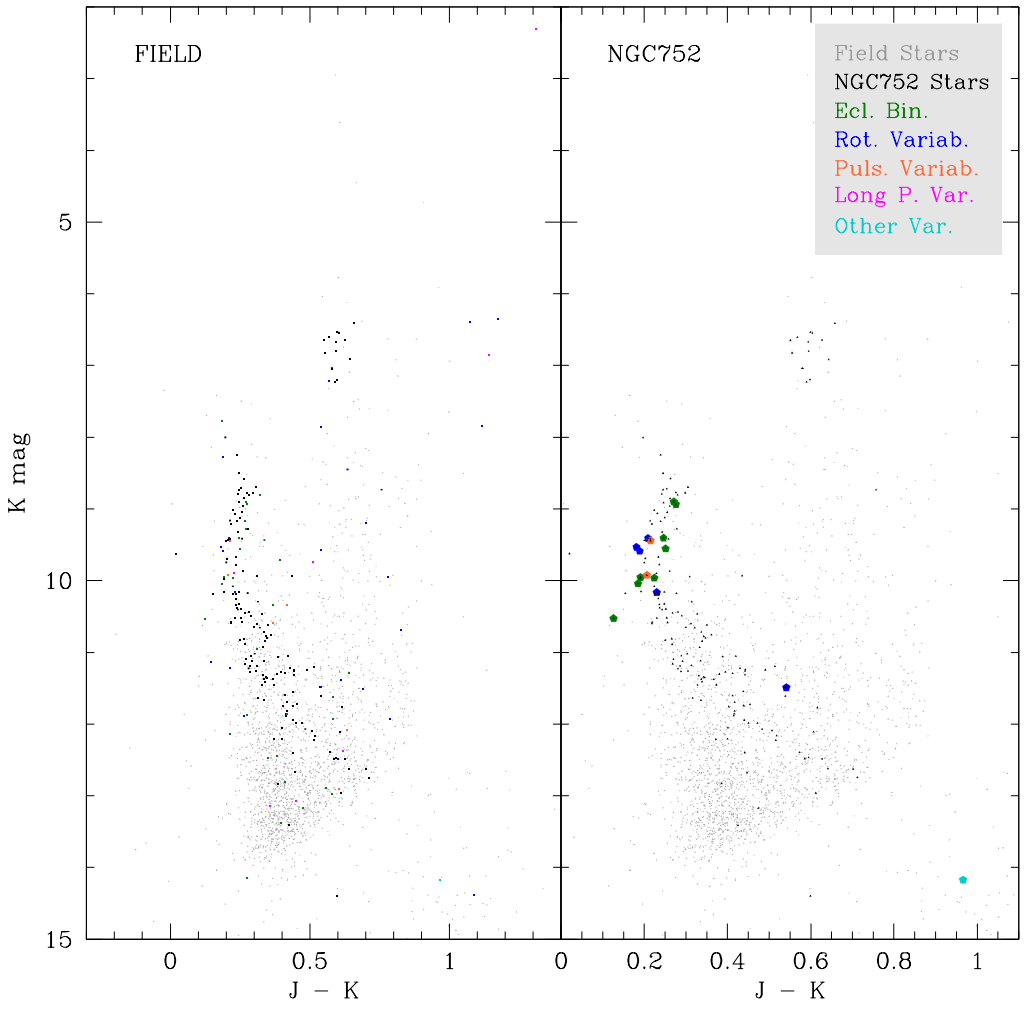

Figure 5.1: *Left panels*: Colour Magnitude Diagram (CMD) with all the stars in the different SuperWASP cameras.
Right panels: zoomed CMD on stars in NGC 752. Variable stars in this panel are only NGC 752 members (following catalogue of Kraus & Hillenbrand 2007).
All the colours are explained in the legend inside second panel. There are eclipsing binaries (in green), rotational variables (in blue), δScuti variables (in orange), long periodic variables (in magenta), and other kinds of variability (in marine).

5.4.1 NGC 752 members

According to the catalogues of Daniel et al. (1994); Mermilliod, Mayor & Udry (2009); Bartašiūtė et al. (2011), the number of NGC 752 stars in common with my master catalogue are 173. The detected variable stars inside NGC 752 were, instead, 16. Among these variable stars, 13 were already discovered in previous articles or projects and 3 stars are new. Some examples are shown in figure 5.2.

Due to the shortage of rotational variable inside the open cluster NGC 752 (only 5 detected), no gyrochronological analysis was carried out. The low number of rotational variable inside this OC will be explained by the fact that NGC 752 is a quite "ancient" open cluster and the stellar activities are less and less with the increase of the OC age.

5.4.2 Field stars

Considering only the field stars, the number of detected variables is 52. Among these variables, 9 are already discovered ones, and 43 are new detections. In figure 5.3 some new variables are shown as example.

5.5 Conclusions

A photometric variability study of NGC 752 was carried out using the SuperWASP public archive. A total of 2456 stars were analysed, using more than 10,000 light curves extracted with aperture photometry algorithms by SuperWASP team and splitted in the different SuperWASP cameras. As already done in M44 case, I used the same three different algorithms to detrend the LCs: SYSREM, TFA, and LTFA. Also for NGC 752 dataset, the LTFA performed better on most light curves.

After the detrend, I used three algorithms for the search for variability and transient: the Generalised Lomb Scargle (GLS), the Analysis of Variance (AoV) and the Box-fitting Least Squares (BLS) algorithms. Matching the results from all the SuperWASP cameras, I detected 68 variables: 22 are already discovered variables, the remaining 46 are previously unpublished variables. I detect 16 variables among the NGC 752 members: three of them are new variables. Overall, I detected: 30 eclipsing binary (16 are new), 24 rotational variables (20 are new), 6 δScuti variables (4 are new), 7 long period variables (5 are new), and 1 other kind of new variable.

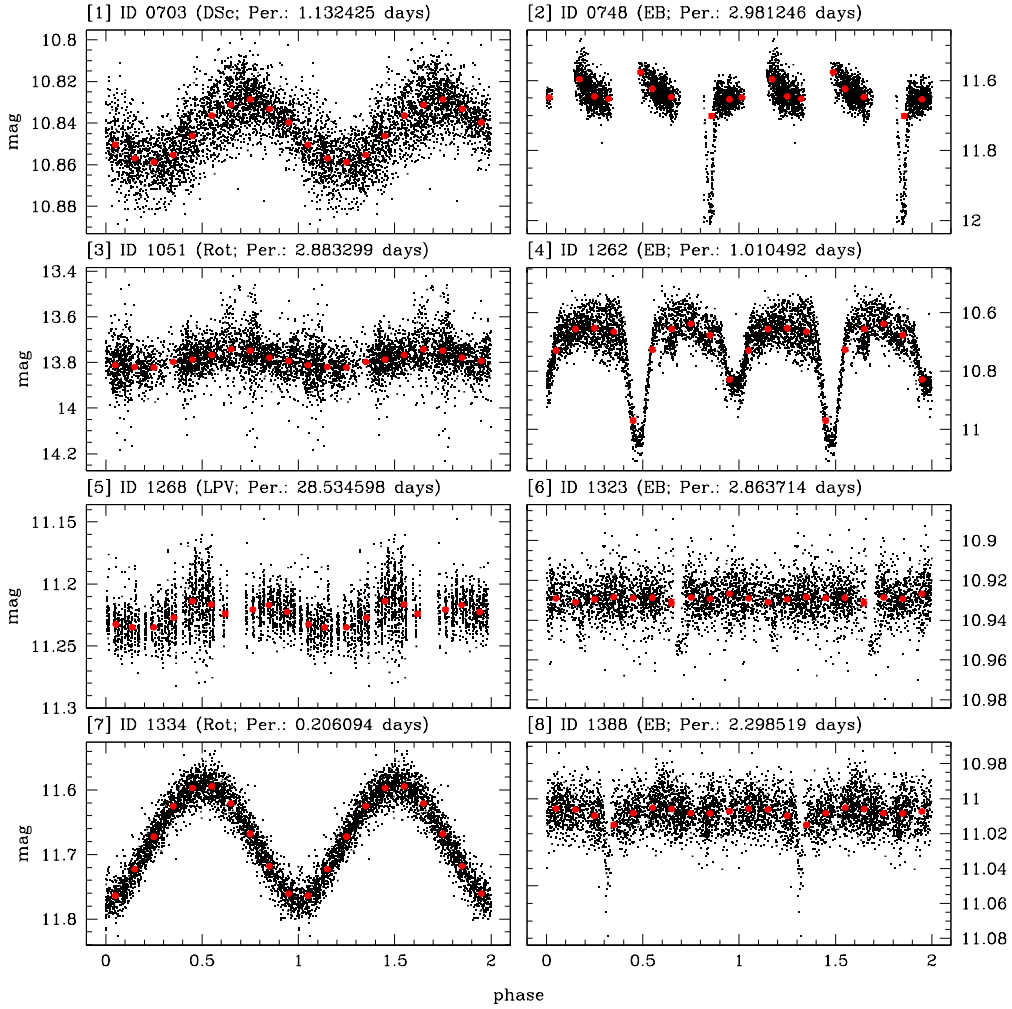

Figure 5.2: Phased LCs of some variable stars, known members of NGC 752. Light curves [3], [5] and [6] are the 3 new detected variables. The variability type and detected period are plotted.

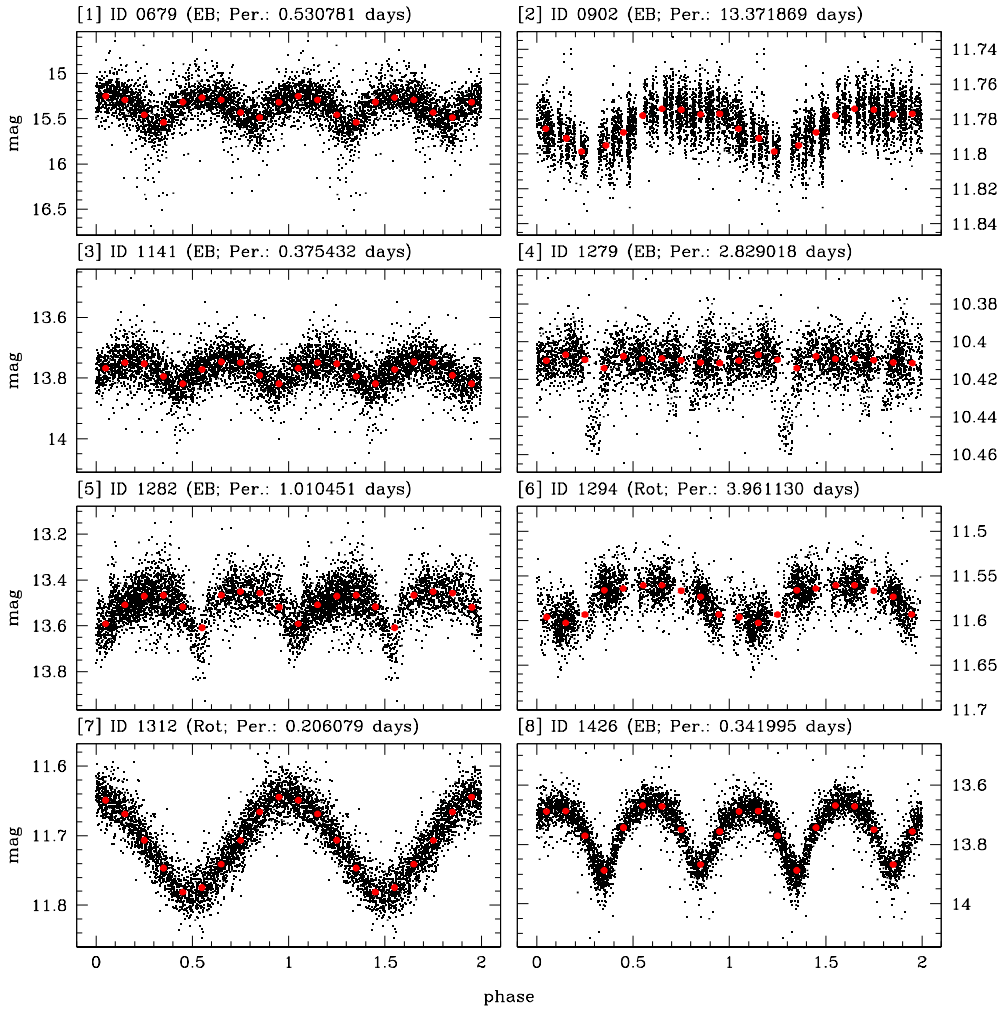

Figure 5.3: LCs in phase of some variable stars, not members of NGC 752 and new variability detection.

Chapter 6

Photometric observations in Open Clusters M35 (NGC 2168) & NGC 2158

The "Asiago Pathfinder for HARPS-N" (APHN) is a survey aimed at collecting high precision long duration multiband photometric series of stellar objects in 5 open clusters: M 35, NGC 2158, M 67, M 44 and NGC 752. The scope is to discover and characterise variable stars and transiting exoplanets in these open clusters. In this chapter, based on the work of Nardiello et al. (2015a) of which I am co-author, I introduce the APHN project, show the new tecniques for light curve extraction and processing, and report on the variability of the objects in the first two analysed open clusters: M 35 and NGC 2158.

6.1 Schmidt 67/92cm - Facilities and observations

All data used in this work come from the Asiago 67/92 cm Schmidt Telescope, located at 1370 m on Mt. Ekar (longitude 11°.5710 E, latitude 45°.8430 N); this facility belongs to the Astronomical Observatory of Padova (OAPD - Osservatorio Astronomico di Padova), which is part of the Istituto Nazionale di Astrofisica (INAF). The instrument mounted at the Schmidt focus is a SBIG STL-11000M camera, equipped with a 4050×2672 pixel Kodak KAI-11000M detector, having a pixel size of 9μm × 9μm, a pixel scale of 862 mas pixel^{-1} (resulting in a 58′×38′ field of view), electronic gain of 0.92 e$^-$/ADU, and a readout noise (RON) of 12 e$^-$/s. The detector is cooled with a thermoelectric Peltier stage, coadiuvated by a radiator with glicole that keeps the operating temperature between −30 and −20 °C.

Under the long-term observing programme "The Asiago Pathfinder for HARPS-N" (PI: Bedin) four fields were awarded with 80 nights per year, during 3 observing campaigns. Taking into account the weather losses, the number of nights statistically guarantees a minimum of ten nights per year in 3 observational campaigns.

The first observing season was a pilot program. We aimed to have the highest number of stars collected with as many photons as possible. Therefore data were collected in white light (hereafter indicated with filter N, for "None"). The unfiltered CCD throughput roughly peaks at ∼500 nm. The exposures were long 120 s, long enough to maximize the duty cycle, the cadence, and the dynamic range vs. sky brightness; in this way we were able to measure faint stars (down to $V \sim 20$) and to monitor more stars in this relatively low Galactic-plane field.

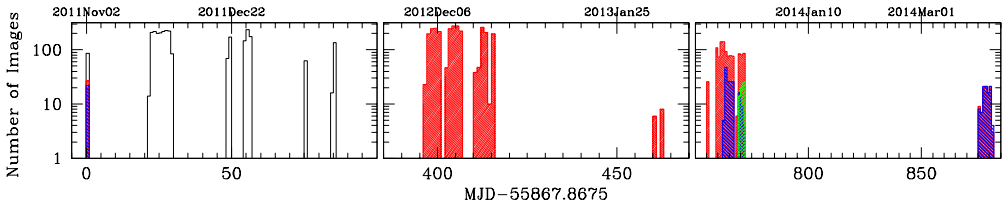

Figure 6.1: Histogram of the number of images per night collected during the first three campaigns of our programme. The white histogram refers to observations in white light, the red, blue and green histograms refer to observations in the R, B and V filters, respectively.

After analyzing season-one data, we realized that the number of stars was adequate, and that we would be able to follow the same stars in a more thoughtful pass-band, filter R, at the cost of slightly increased exposure times (180 s). This would allow better comparison with stellar models and at the same time suppress noise due to larger chromatic and sky-brightness effects. It was also clear from the pilot data-set that adding short exposures of 15 s would have extended the photometric monitoring to a non-negligible sample of saturated stars. There is an additional benefit in alternating short and long exposures besides the increased dynamic range. The use of short exposures means that unsaturated data will still result from the bulk of the stars in the case of extremely good seeing. Short exposures could not be shorter than 15 s because of the reliability on the shutter time. Therefore, when season two and three were accepted we decided to alternate between these short and long exposures in filter R only.

Preliminary results from first two seasons shown that we were able to find many new variables in the field (and 21 variables were found in the photometric series from short exposures, Sect. 6.3.1).

Once the variable stars are found, the natural follow up is to collect information about their spectral energy distribution (SED). Therefore, in the third season we collected long exposures alternating both B and R and occasionally we took exposures in V. Colour information is particularly important for the characterization of the components of binary systems, not only off-eclipse, but possibly also during the eclipses. Given the successful outcome of this project, additional observing time for follow-up observations in I-band has been allocated (unfortunately U is not doable from Asiago) for the M 35 and NGC 2158 field.

During the first year the fine pointing of the field was not optimal. There is an incomplete overlap between the N and $B\,R\,V$ photometric series, resulting in a $\sim$10% sky area not imaged through all the four filters.

Observations included standard calibration data (bias, dark, sky and dome flats) at the beginning and end of each night. In Table 6.1 we give a log of the observations. Figure 6.1 shows the histograms of the number of images gathered each night for a given filter during the three seasons.

For the other clusters of this survey we will adopt the following strategy: long + short R exposure in the first season, and multi-filter characterization in the following seasons. With our instrumentation this turns out to be a rather effective strategy, doubling the number of known variables in a relatively well-studied field such as that of M 35 and NGC 2158.[1]

[1]"A posteriori", knowing the characteristics of the M35 and NGC2158 field, it would have been better to have the variable finding campaign in the 3 seasons in short and long+short R, and colour information from B, and occasionally V and I.

Filter	# Images	Exp. Time (s)	FWHM (arcsec)	median FWHM (arcsec)
B	21	120	1.44–5.28	2.65
	258	180		
	1	240		
V	60	180	1.24–2.05	1.43
R	1385	15	1.35–6.34	2.75
	27	120		
	2552	180		
N	2692	120	1.67–7.05	2.85

Table 6.1: Log of observations.

6.2 Data reduction

6.2.1 Extraction LCs

For all our reductions we developed custom software tools written in `FORTRAN 77` or `Fortran 90/95`, adapted from the same software described in previous papers by some of the co-authors of this work (we will give in the following brief descriptions and references).

Pre-reduction

The first stage of our pipeline produces master biases, master darks and master flats for each night. Such master frames are clipped means of the individual calibration images gathered on each observing night. We almost always used dome flats, because they proved to be more accurate and stable than typical sky flats. Flats were bias-subtracted, while science images were dark-subtracted, the master dark being constructed from darks having the same exposure time as the photometric series. The dark-subtracted scientific images were then divided by the bias-subtracted flats of the corresponding filter. The correction was performed by using a custom master-flat field for each night.

Point Spread Functions

The point-spread function (PSF) of the Asiago Schmidt camera is almost always well sampled, with the exception of a few images collected in the best-seeing conditions. In these cases only the central part of the detector is affected by undersampled PSFs, in which the image quality, measured as the full width at half maximum (FHWM), is below 1.8 arcsec.

To compute the PSF models, we developed the software `img2psf_Sch` in which our PSF models are derived in a completely empirical fashion. This code follows a similar software developed for WFI@ESO/MPG 2.2m data, and described in depth in Anderson et al. (2006). The Asiago Schmidt's PSFs are modeled through an array of 201×201 grid points, which super-sample the PSF pixels by a factor of 4 with respect to the image pixels. A bicubic spline is then fitted to interpolate the value of the PSF in between these grid points. Furthermore, in order to model the considerable amount of spatial variations of the PSFs across the field of view of each individual image, we divided the detector in 9×5 regions, and empirically derived the PSFs independently within each of these subregions. A bilinear interpolation is then applied to obtain the best PSF model at any specific location on the detector. This interpolation is performed for every individual star on each frame (Anderson et al. 2006).

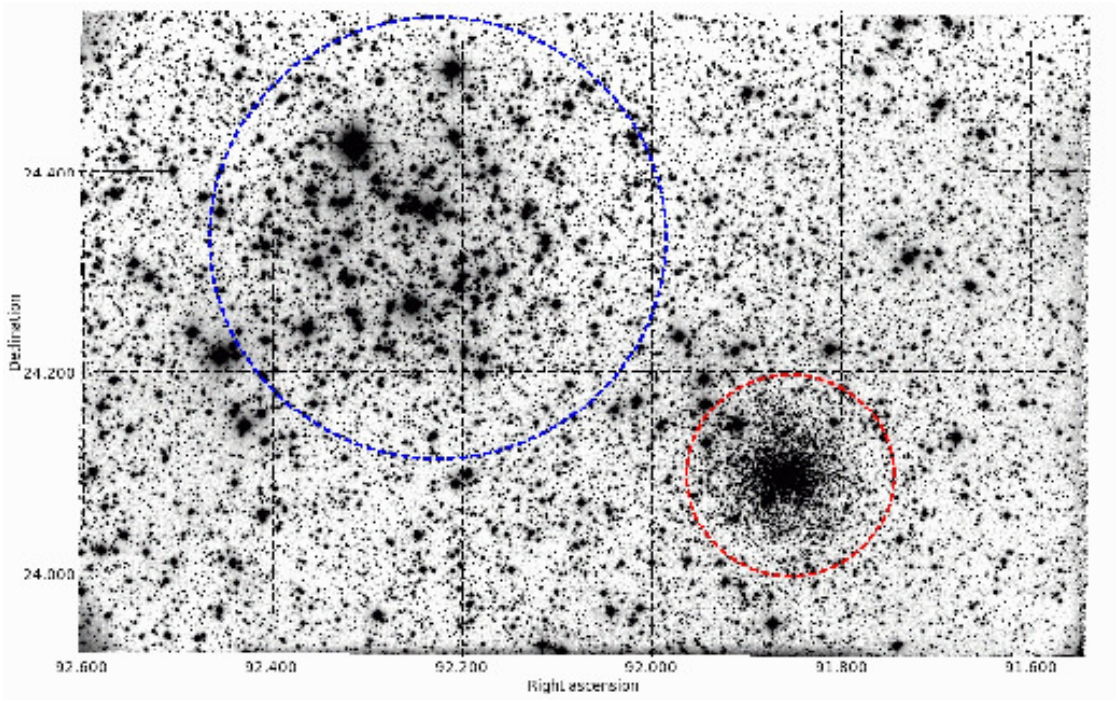

Figure 6.2: Stacked R-filter image from our data. The blue circle marks the M 35 region. The red circle marks the region of NGC 2158.

Astrometry

During the first and the third observing seasons, 25 images with both large and small dithers were collected with the purpose of solving for the geometric distortion of the Schmidt's camera. We carried out the same self-calibration procedure described in several of our previous works (for example: Libralato et al. 2014; Bellini & Bedin 2010; Bellini, Anderson & Bedin 2011; Anderson et al. 2006). The average geometric distortion is about 1 pixel from corner to the centre of the detector (i.e., $\sim$1 arcsec).

We applied this geometric distortion solution to the raw star positions obtained by fitting our empirical PSFs in each individual image. The distortion-corrected positions of each image were then transformed into a common distortion-corrected reference frame. We employed as reference frame the distortion-corrected positions of the image with the smallest airmass and the best seeing in R (the ID of this image is `SC23779`).

We considered the most-general linear transformations (six parameters, i.e., two shifts, rotation, a scale-factor, two skew terms), and derived through a linear least-square fit of the pairs of distortion-corrected coordinates of all (well-measured) stars in common between the two frames (the considered frame, and the reference frame). Such lists of pairs were saved in so-called transformation files.

The consistency of positions on the reference frame tells us how well we are able to transform the coordinate system of one image into another image taken at a different epoch. For the best stars (below saturation, isolated and measured with a high signal to noise ratio) we found a consistency in position of about 20 mas (i.e., $\sim$0.02 pixels). Not enough to determine accurate

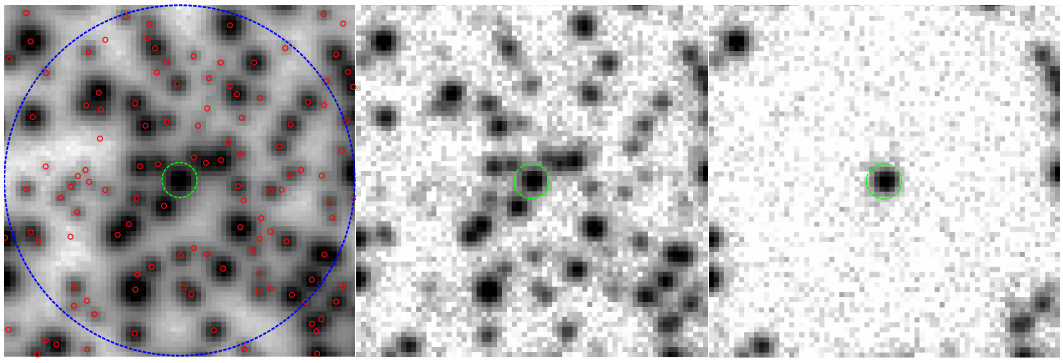

Figure 6.3: An example of neighbour subtraction. The left panel shows a typical subregion of the stacked image; all detected sources are marked with red circles. The middle panel shows the same for an individual image (`SC23893`); the target star is located at the centre of the panel (marked by a green circle). The right panel shows the same region after the subtraction of neighbours within a radius of 35 pixels.

proper motions for most stars with the available time baseline, but accurate enough to register time series photometry.

Stacked Images

The transformations from the distortion-corrected coordinates of each image into the reference frame were used to create a stacked, high-S/N image of the field for each filter. The "stack" provides a deeper view of our FOV. The stack for the filter R is shown in Fig. 6.2. We edited the header of each of these stacked images, adding World Coordinate System keywords, where the absolute astrometric solution was computed matching the 2MASS (Skrutskie et al. 2006) point source catalogue with our sources. The absolute astrometric accuracy of 2MASS is estimated to be about 200 mas.

As part of the material provided in this paper, we make electronically available the astrometrized stacked images for each filter.

The master star list

Stacked images contain much more information than individual exposures, having essentially a much higher S/N. In the case of the R and N stacks, images have integrated exposure times thousands of times longer than that of a single image. The increased depth means that we could extract more complete and unbiased star lists. Using the same software described in Sect. 6.2.1, we derived improved star lists from the R and N stacked images, i.e., the deepest ones. Our finding algorithm takes all the local maxima above the local sky with an integrated flux of at least 3 digital numbers (DNs), and isolated by at least 3 pixels from the nearest peak. Positions and fluxes on the stacked images were obtained by simultaneous PSF fitting of the target star and all of its neighbours, in an iterative fashion. The program that performs the finding and simultaneous iterative PSF fit, `img2xym_Sch`, is an adaptation of the code `img2xym_WFI` presented in Anderson et al. (2006) and thereby described in details. All the objects in the R star list were then transformed to the astrometric and photometric system of the reference image (ID

SC23779). For the N star list, the photometric reference system of image SC25458 was adopted, but coordinates were kept in the R astrometric reference frame.

The above mentioned star lists initially contained a large number of false detections, such as PSF artifacts, warm pixels, etc. We purged the star lists from artifacts and non-stellar objects as follows. Most of the background galaxies were discriminated using the qfit parameter, a diagnostic related to the quality of the PSF fit and described in Anderson et al. (2008). The artifacts of the PSFs are identified using the procedures described in Libralato et al. (2014).

The final N+R combined and purged star list contains 66 486 objects and constitutes the catalogue that will be used for the extraction of light curves throughout the following sections. We refer to this catalogue as Master Star List (hereafter, MSL).

Photometry with and without neighbours

To extract light curves, we developed a parallel code written in Fortran 90/95 which uses OpenMP, in order to run simultaneously on several CPU cores (32 on our workstation). The software takes as input *(i)* the MSL catalogue as defined in the previous section, *(ii)* the PSFs described in Sect. 6.2.1, and *(iii)* the lists of pairs of coordinates described in Sect. 6.2.1 (transformation files; stars in common between the MSL and each individual image). In this work we extracted the raw fluxes of all point source detected in the field (i.e., in the MSL) using both PSF and aperture photometry, keeping for the final stage of the analysis only the photometric reduction that minimizes the scatter in the extracted light curves (as we describe in the next sections). We already described the local PSF technique in Sect. 6.2.1, while aperture photometry is computed through a traditional approach, by running a software pipeline originally developed for the TASTE project (The Asiago Search for Transit time variations of Exoplanets; Nascimbeni et al. 2011). The underlying routines are explained in details in Nascimbeni et al. (2013).

For each target star in the MSL, light curves are extracted in two parallel versions. A first version from the original images, and a second one from images where the neighbours close to the target star were PSF-fitted and subtracted. The neighbour subtraction is done as follows. For each target star we computed 6-parameter local transformations between the MSL reference systems and the distortion-corrected coordinates of stars in the individual image, using the best measured bright, unsaturated and isolated stars located within 500 pixels of the target star. The magnitudes in the two reference systems are also used to register the fluxes in the two photometric systems. With these local transformations, magnitude shifts, and PSFs, the stars of the MSL located less than 35 pixels from the targets are modelled and subtracted from each individual image. Note that such modelling requires an inversion of the geometric distortion solution to obtain the coordinates on the raw image reference system. Figure 6.3 compares a patch of sky around a typical target star: 1) on the stacked image, 2) in an individual image before the subtraction of the neighbours, and 3) after the neighbour subtraction. After the subtraction procedure, the software performs four parallel reductions: aperture and PSF-fitting photometry of the target star, both on the original frames and on the images where the nearby stars are subtracted. The centroid used for aperture photometry of the target star is computed using the same local 6-parameters transformations described above.

We found that adopting a dynamical aperture, i.e., adapting the radius r of the circular photometric aperture to each image, provides the best photometry. From theoretical computations we know that in the case of a two-dimensional Gaussian PSF the optimum S/N ratio is provided by an aperture radius $r \approx 0.68 \times$ FWHM (see for example: Mighell 1999). About 72% of the total stellar flux is enclosed within this radius. However, we empirically found that larger apertures result in light curves of smaller scatter for objects at the bright end of our sample. As a compromise, we adopted $r = 1 \times$ FWHM, which improves aperture photometry for stars having

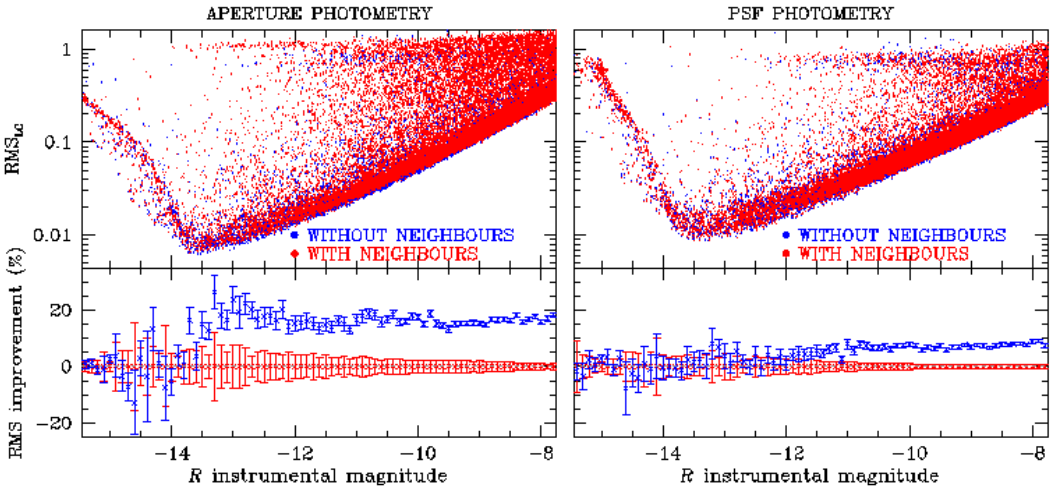

Figure 6.4: Photometric RMS derived from the original "long" R images (in red) compared to the RMS obtained from the same images after neighbour-subtraction (blue), for both aperture photometry (*left*) and PSF photometry (*right*). The lower panels show the percentage improvement of the neighbour-subtracted algorithm on the RMS, averaged over 0.1-mag bins. The error bars are given as the 68.27th percentile of the residuals around the median values.

instrumental magnitudes < -10.5, but at the cost of worsening the photometry of faintest stars.

The fitting radius of the PSFs was set to a constant value, equal to 2.65 pixels, as it proved to minimize the scatter of the light curves at all magnitudes.

For all the four reductions we computed the local value of the sky background within a circular annulus of inner radius $r_{\rm in} = 7.5\,\sigma$ and outer radius $r_{\rm out} = r_{\rm in} + 8$, where $\sigma = {\rm FWHM}/2.355$ is the standard deviation of the best-fit Gaussian PSF.

We found that photometry on images after neighbour subtraction performs –on average– better than that computed on original images. This is illustrated in Fig. 6.4: the top panels display the comparison between the photometric RMS (left panel in the case of aperture photometry, right panel in the case of PSF photometry) obtained from original images (red) and the photometric RMS after neighbour subtraction (blue); the lower panels show the improvement of the neighbour-subtracted algorithm regarding the photometric RMS, averaged over 0.1-mag bins. Therefore, in the following (unless otherwise quoted) we will make use of light curves derived from aperture and PSF photometry obtained from neighbour-subtracted images.

6.2.2 Detrend of the LCs: DeTrendy

To remove residual systematic errors from the light curves derived in the previous section we followed the procedure described in detail by Nascimbeni et al. (2014). For each target star we selected a group of reference stars, which are used to define the local photometric zero point of each target in all the individual images. These reference stars were empirically and iteratively weighted to minimize the scatter on the final differential light curve. A first list of candidate reference stars is selected by computing the median photometric scatter σ of the raw light curves as a function of magnitude, then binning over magnitude bins and discarding every source with a RMS 4σ larger than the median RMS of the corresponding magnitude bin.

A short description of the detrending algorithm follows. Let us consider the k-th target

star, the j-th reference star and the i-th epoch where both k and j stars are detected. First we computed the differential light curve $m_{i,k} - m_{i,j}$, its median magnitude and scatter σ_{jk}, which are then used to compute the initial weights $w_{jk} = 1/\sigma_{jk}^2$ for each reference star. The final weights are obtained multiplying w_{jk} by two additional factors: $W_{jk} = (1/\sigma_{jk}^2) \cdot D_{jk} \cdot M_{jk}$. The factor D_{jk} is an analytic function of the relative on-sky position (ρ_{jk}) between the reference star and the target star: it is zero within a radius $r_0 = 20$ pix to avoid blending and/or contamination, it is equal to one between r_0 and $r_{\rm in} = 200$ pix, and decreases exponentially with ρ_{jk} from one to zero with a $r_{\rm out} - r_{\rm in}$ scale radius, where $r_{\rm out} = 300$ pix. The weight M_{jk} is defined in a similar way, as a function of the magnitude difference $\phi_{jk} =\mid m_j - m_k \mid$ between the target and the reference star: it is equal to unity when this difference is less than $f_{\rm in} = 1.0$ mag, otherwise it decreases exponentially with ϕ_{jk} with $f_{\rm out} - f_{\rm in}$ scale radius and $f_{\rm out} = 1.75$ mag. The D_{jk} and M_{jk} factors assign a larger weight to reference stars which are closer to the target and of similar brightness, minimizing flux- and position-dependent systematics.

For comparison purposes, we computed two different zero-point corrections. A global zero point correction (GZP) τ_i, defined by the formula:

$$m'_{i,k} = m_{i,k} - \tau_i = m_{i,k} - \langle m_{i,j} - \langle m_{i,j} \rangle_i \rangle_j \tag{6.1}$$

where the notation $\langle x \rangle_y$ represents the averaging of x over the index y. The output of GZP is then a classical, unweighted differential photometry, where all the reference stars have unitary weight. The local zero point correction (LZP) τ' is computed with an expression equivalent to τ, but this time using the weighted mean of magnitudes of our set of reference stars, where the weights are assigned as W_{jk} and computed as above. Figure 6.5 compares the scatter of the light curves corrected using the GZP (red) and LZP (blue) detrending algorithms, both for aperture photometry (on the left panels) and for PSF-fitting photometry (on the right panels). The improvement obtained with the LZP correction is evident (10–20%), especially on the bright, non-saturated side of the sample. For this reason, only the LZP light curves are analyzed in the next sections.

Finally, the RMS of the neighbour-subtracted, LZP-detrended aperture vs. PSF-fitting photometry is compared in Fig. 6.6, for long exposures in the R filter. It appears that aperture photometry performs on average better than PSF-fitting photometry on bright stars (with instrumental magnitude < -10.5), while PSF-fitting photometry gives best results on fainter stars, as expected (see Sect. 6.2.1). From here on, for each target star in the MSL, only the light curve that provides the smallest overall scatter goes through the next stages of analysis.

6.3 Analysis of variability

6.3.1 Research of variability

We employed three different software tools to detect candidate variable stars in our dataset of LZP-corrected, neighbour-subtracted light curves. These are: the Lomb-Scargle (LS) periodogram (Lomb 1976; Scargle 1982), the Analysis of Variance (AoV) periodogram (Schwarzenberg-Czerny 1989) and the Box-fitting Least-Squares (BLS) periodogram (Kovács, Zucker & Mazeh 2002). All these tools are implemented within the code `VARTOOLS` v1.202, written by Hartman et al. (2008) and publicly available[2].

The LS algorithm is most effective in detecting sinusoidal or pseudo-sinusoidal periodic variables. It provides the formal false alarm probability (FAP) as a quantitative diagnostic to select stars with the highest probability to be genuine variables. We searched for more general types

[2] http://www.astro.princeton.edu/ jhartman/vartools.html

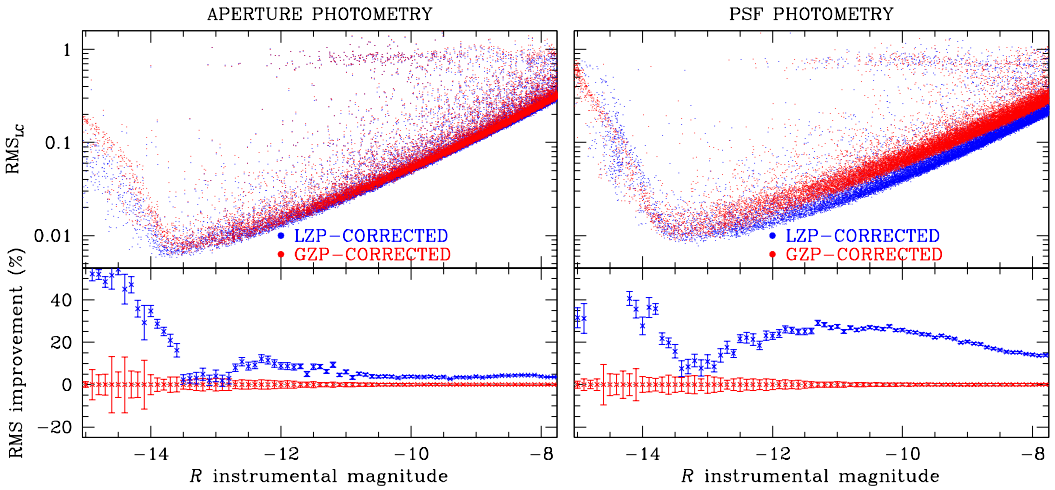

Figure 6.5: Photometric RMS, obtained from neighbours subtracted images, for GZP-corrected (red) and LZP-corrected light curves (blue). This is shown for both aperture photometry (*left*) and PSF photometry (*right*). As in Fig. 6.4, the bottom panels show the improvement of the LZP algorithm compared to the GZP one.

of periodic variables through the AoV algorithm, as it is based on variance minimization with phase binning, which is a more flexible approach. As for the LS method, we used the AoV FAP metric Θ to select stars that have a high probability to be variables. The BLS algorithm is particularly effective when searching for box-like dips in a otherwise flat or nearly flat light curve, such as those caused by detached eclipsing binaries and planetary transits. In order to select good candidates, we used the diagnostic parameter "signal-to-pink noise" (Pont, Zucker & Queloz 2006), as defined by Hartman et al. (2009). Before running the periodograms, we converted the temporal axis of all light curves from Modified Julian Date (MJD) to the Barycentric Julian Date (BJD) reference frame and Barycentric Dynamical Time (TDB) standard. This standard provides consistency and is much more reliable when comparing observations on very long baselines (Eastman, Siverd & Gaudi 2010).

We searched for variables independently on both the aperture- and the PSF-fitting light curves (LZP-detrended, from neighbour-subtracted images). These finding algorithms were also run independently on both the R and the N photometric series. On the R light curves we employed LS and AoV to search for variables with periods between 0.01 and 881 days, with a sampling of 0.0005 times the Nyquist one in the frequency space. The period interval set for the BLS algorithm is between 0.5 and 881 days. On the unfiltered light curves (N), LS and AOV were set to periods between 0.01–85.5 days (frequency sampling of 0.0005 times the Nyquist one), while BLS between 0.5–85.5 days.

6.3.2 Selection of the best periodical LCs

For all three finding methods (LS, AoV, BLS) we applied the procedure illustrated in Fig. 6.7 to identify the candidate variables. We first constructed the histogram of the detected periods for all the light curves (panel (a) of Fig. 6.7); spikes in the histogram at this stage are probably associated to spurious periods due to systematic errors, such as instrumental and atmospheric artifacts, which affect a significant fraction of light curves even after the LZP correction. We

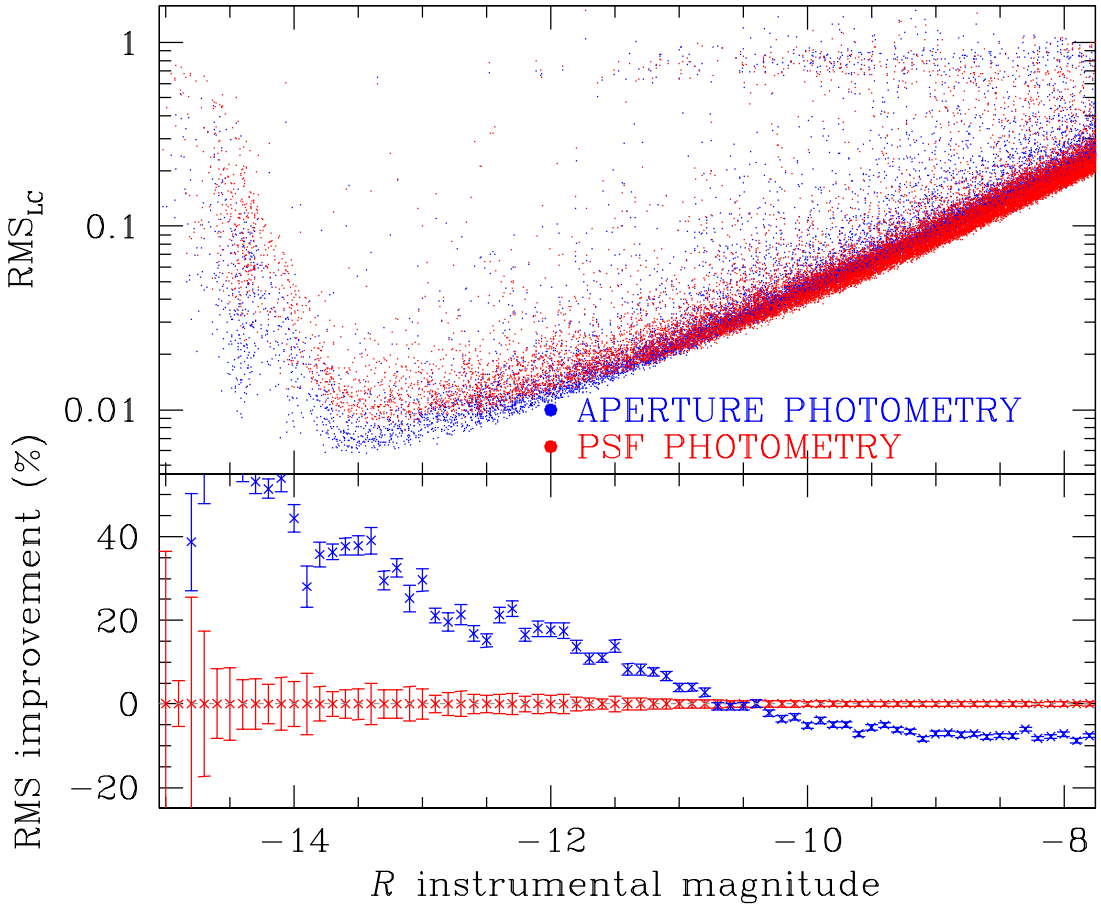

Figure 6.6: *Top panel*: photometric rms as function of R instrumental magnitude for PSF photometry (red) and for aperture photometry (blue). *Bottom panel*: percentage variation with respect to PSF-fitting photometry. This shows that for bright stars (instrumental $R < -10.5$) aperture photometry is better than PSF photometry.

removed from our catalogue those stars close to the spikes as follows: for each period P_0 of the histogram of Fig. 6.7a, we considered a region around it of radius equal to $50 \times \delta P$, where δP is the bin chosen to build the histogram. We computed the median of the counts of the considered bins, and we flagged P_0 as spike if the associated counts are 5σ above the median, where σ is the 68.27th percentile of the sorted residuals from the median value. For the periods associated to spikes, we kept the light curves with low FAP (or high AoV or signal-to-pink-noise), i.e. the light curves above the 99.5th percentile of the $-$FAP (or the AoV or signal-to-pink-noise – see panel (b) of Fig. 6.7). Panels (c) and (d) show the FAP as a function of the detected period, respectively before and after the spike subtraction. As a last step to select candidate variables, we divided the distribution of panel (d) in 25 period bins and selected only stars above the 97th percentile of $-$FAP.

Finally, we combined the lists of candidates obtained with the three aforementioned methods, and visually inspected each of them. We identified 519 real variables: $BVRN$ light curves are available for 442 of them, while for 37 objects only BVR light curves are available. Nineteen stars have only N light curves, and the remaining 21 have only short exposures in R. For the 442 variables in common between R and N, we refined their periods with the following recipe. For each star we normalized the R and the N light curves to zero by subtracting the median magnitude. Then we merged the two light curves. In this way we obtained a normalized light curve that spans three years. We ran the VARTOOLS algorithms LS, AoV, and BLS on this normalized light curve using the same parameters described above, to find the best period of the associated variable star. While no modelling can be carried out on such hybrid light curves, the uncertainty on the resulting period is clearly lowered.

6.4 Results

Amongst the 66 486 stars we found 519 variables, which appear to be point-like sources in the R and N stacked images: 246 of them are already known variable stars and 273 are new ones. The list of all variables is given in Table 6.2: we provide our identification number, position, period, magnitudes (when available) in $BVRJ_{\rm 2MASS}H_{\rm 2MASS}K_{\rm 2MASS}$, variable type[3] and the cross-identification with known variables.

Figure 6.8 shows the folded light curves of all the variables listed in Table 6.2 (all figures are available in the electronic version of the journal): each panel shows, from top to bottom, the light curves in white light N (black), in R (red), B (blue) and V (green) filters. For each filter the y-axis has the same extension in magnitude range. The identification number and the determined period are reported above each panel.

Figure 6.2 shows the stacked image in the R filter. For illustrative purposes we define two regions around the two clusters: the blue circle which should contain prevalently stars belonging to M 35 inside an arbitrary radius of about $13\farcm8$, while the red circle, with a radius of $6\farcm0$ should include mainly NGC 2158 stars. The B vs. $(B-V)$ color-magnitude diagram (CMD) of the stars within the blue circle is shown in the left panel of Fig. 6.9. The central panel shows the CMD of the stars within the red circle and in the right panel the CMD of the stars outside both regions. Clearly, the CMD of each region shows contamination by stars from the other two regions.

[3]The classification of variable stars was done by eye, and sometimes was difficult.

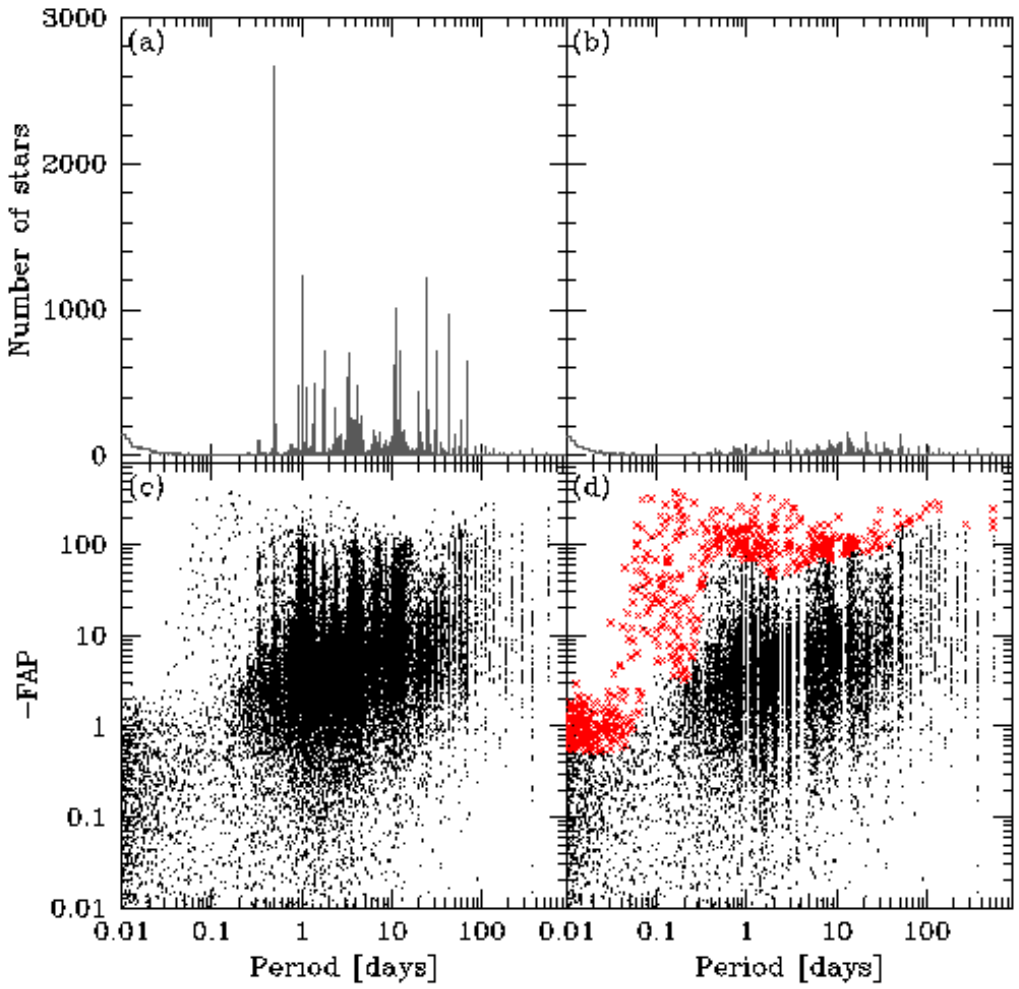

Figure 6.7: Example of the procedure followed for the extraction of candidate variables from the dataset of light curves in the case of LS algorithm. *Panel (a)*: distribution of the periods obtained from all the light curves; *panel (b)*: distribution of the periods after spikes suppression; *panel (c)*: periods of light curves as a function of FAP for all the stars; *panel (d)*: the same of panel (c) after spikes suppression. The suspected variables are displayed inn red. See text for details.

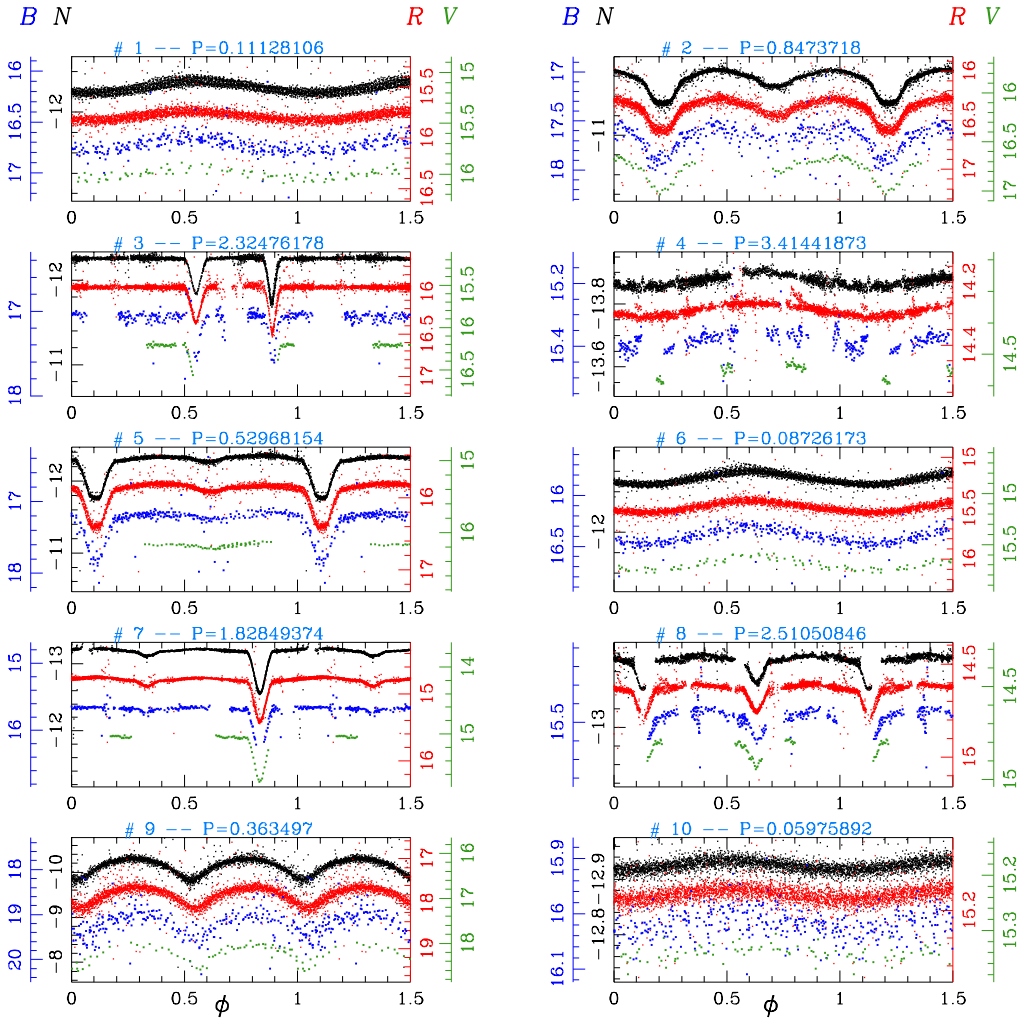

Figure 6.8: Light curves of the first 10 variables. For each variable star we show (when available) the N (black), R (red), B (blue) and V (green) light curves from top to bottom of each panel.

Table 6.2: First ten lines of the catalogue of variable stars.

N (1)	α(J2000) (2)	δ(J2000) (3)	P(days) (4)	B (5)	V (6)	R (7)	N (8)	J_{2MASS} (9)	H_{2MASS} (10)	K_{2MASS} (11)	Type (12)	MP'_{M35} (13)	$MP'_{NGC2158}$ (14)	Notes (15-20)
1	91.858422	+24.073243	0.11128106	16.72	15.99	15.78	-11.98	14.316	14.133	13.731	δSct	-99.999	62	V37[3]
2	92.561694	+24.006494	0.8473718	17.64	16.72	16.35	-11.32	14.749	14.420	14.230	EB	-99.999	-99.999	
3	92.488468	+24.058195	2.32476178	17.06	16.21	15.94	-11.77	14.546	14.286	14.066	EB	-99.999	-99.999	
4	91.858693	+24.43994	3.41441873	15.37	14.54	14.28	-13.44	12.974	12.562	12.478	Rot	-99.999	-99.999	
5	92.335142	+24.254324	0.52968154	17.20	16.17	15.85	-11.82	14.634	14.014	13.925	EB	96	-99.999	V7 [2]
6	92.350003	+24.314434	0.08726173	16.40	15.70	15.48	-12.30	14.197	13.888	13.862	δSct	0	-99.999	V16[5]
7	92.221929	+24.477042	1.82849374	15.67	15.05	14.79	-12.92	13.491	13.094	12.996	EB	94	-99.999	V15[5]
8	92.058242	+24.510734	2.51050846	15.47	14.81	14.62	-13.14	13.403	13.153	13.062	EB	96	-99.999	
9	91.919161	+24.084334	0.363497	19.16	18.17	17.77	-9.86	16.104	15.669	15.293	EB	-99.999	-99.999	V05[3], 25 [4]
10	92.106682	+24.257778	0.05975892	16.01	15.33	15.17	-12.63	14.081	13.897	13.718	δSct	95	-99.999	

Notes.
[1] Kim et al. (2004); [2] Hu et al. (2005); [3] Mochejska et al. (2006); [4] Meibom, Mathieu & Stassun (2009); [5] Jeon & Lee (2010); [6] GCVS
[7] Membership Probabilities for M 35 and NGC 2158 expressed in % : http://www.astro.iag.usp.br/ocdb/ (Dias et al. 2014)

6.4.1 Inside M35 and NGC 2158

We used the membership probabilities given by Dias et al. (2014) to verify the membership of the identified variable stars. We found 248 common stars between our catalogue and their M 35 catalogue; of these stars, 197 have a probability $\geq 50\%$ to belong to M 35. By matching our catalogue of variable stars with the NGC 2158 catalogue of Dias et al. (2014), we found only 9 stars in common, 5 of which have a membership probability $\geq 50\%$.

The membership probabilities for the two clusters are tabulated in columns 12 and 13 of Table 6.2.

6.4.2 Stars in the field of view

Eclipsing binaries

We extracted 97 light curves of eclipsing binaries (EBs): 41 of these were previously known, the others are new. Many of them are detached systems that, if cluster members, offer the potential for obtaining very precise cluster ages and distances and for testing stellar evolution models, e.g., along the lines of Brogaard et al. (2012). For 9 of these new EBs we have membership probabilities from Dias et al. (2014): we found that 8 of them have a high probability ($\geq 87\%$) to be members of M 35. They are V8, V149, V231, V271, V422, V513, V514 and V517. For NGC 2158 we have no membership information, but looking at Fig. 6.10 there is a good chance that a substantial fraction of the eclipsing systems in the field of NGC 2158 are members, since they are located along the cluster sequence in the CMD.

The period distribution of the identified EBs is likely to be significantly biased towards short periods and the periods for the longer period systems are uncertain as in common for ground based surveys (Rucinski, Kaluzny & Hilditch 1996). However, complementary observations from *K2* should alleviate these issues once analyzed.

Rotating Stars

We classify 284 of our variables as rotating stars, of which 122 are new discoveries. Their light curves show sinusoidal light variations, mainly due to the starspots that follow the surface rotation. We found that, for many of these stars, the shape of the light curves changes during the three years, but their period remained fairly unchanged (see V18 for an example). Other stars show a sinusoidal shape light curve in one observational run, but their light curve is flat in the other runs (for example V237). There are stars that changed their median magnitude from one year to another, such as V274 or V302.

Figure 6.11 shows the relation between the period of the variable stars and their $B - V$ (top panel) and $B - K_{\rm 2MASS}$ (bottom panel) colours: the variable stars are in grey, red circles represent the variable stars identified as rotating stars, while blue dots are rotating stars with a probability $\geq 50\%$ to be M 35 members.

Meibom, Mathieu & Stassun (2009) carried out a detailed analysis of the period-$(B - V)$ colour index relation using 310 stars members of M 35, of which 153 are in common with our catalogue.

δ Scuti and other variable stars

We identified 67 δ Scuti stars, 45 of which were previously unknown. In the CMDs, they are mainly located above the main-sequence turn-off of NGC 2158.

Finally, we found 69 variable stars that show long period variations or nonperiodic signals, 21 of these already known. We also found a δ Cep (V442, already known) and a RRLy (V492).

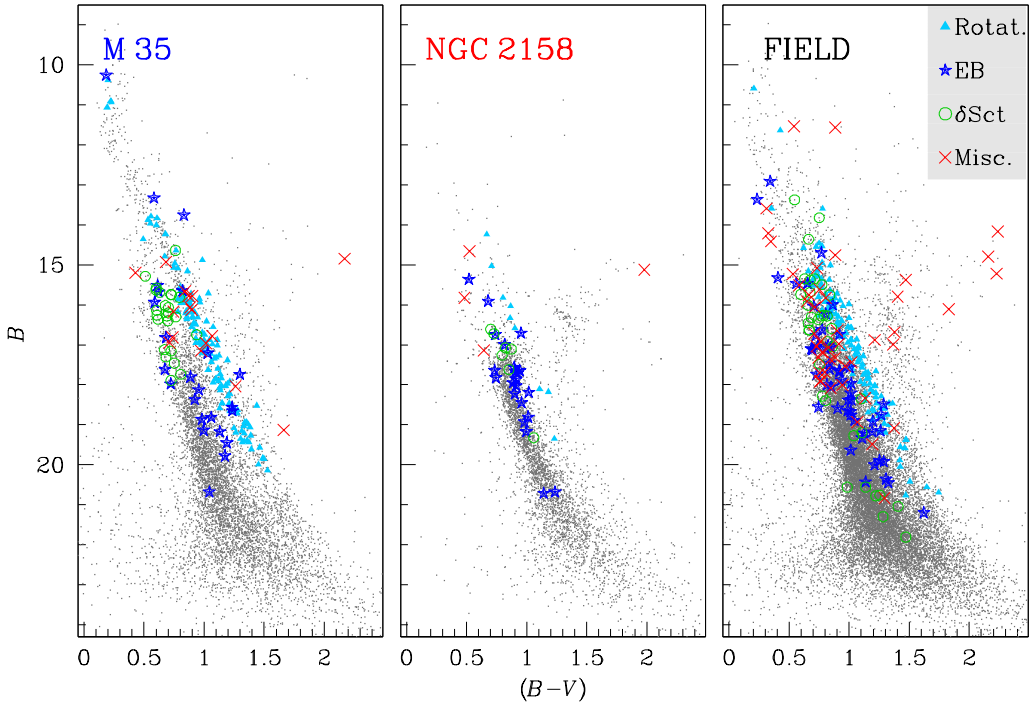

Figure 6.9: *Left panel*: stars inside the region delimited by the blue circle (M 35) in Fig. 6.2. *Central panel*: stars inside the region delimited by the red circle (NGC 2158) in Fig. 6.2. *Right panel*: stars outside the region delimited by the blue and red circles in Fig. 6.2. Different symbols represent different variable types: azure triangles for rotating stars, blue stars for eclipsing binaries, green open circle for δ Scuti and red crosses for the other variables.

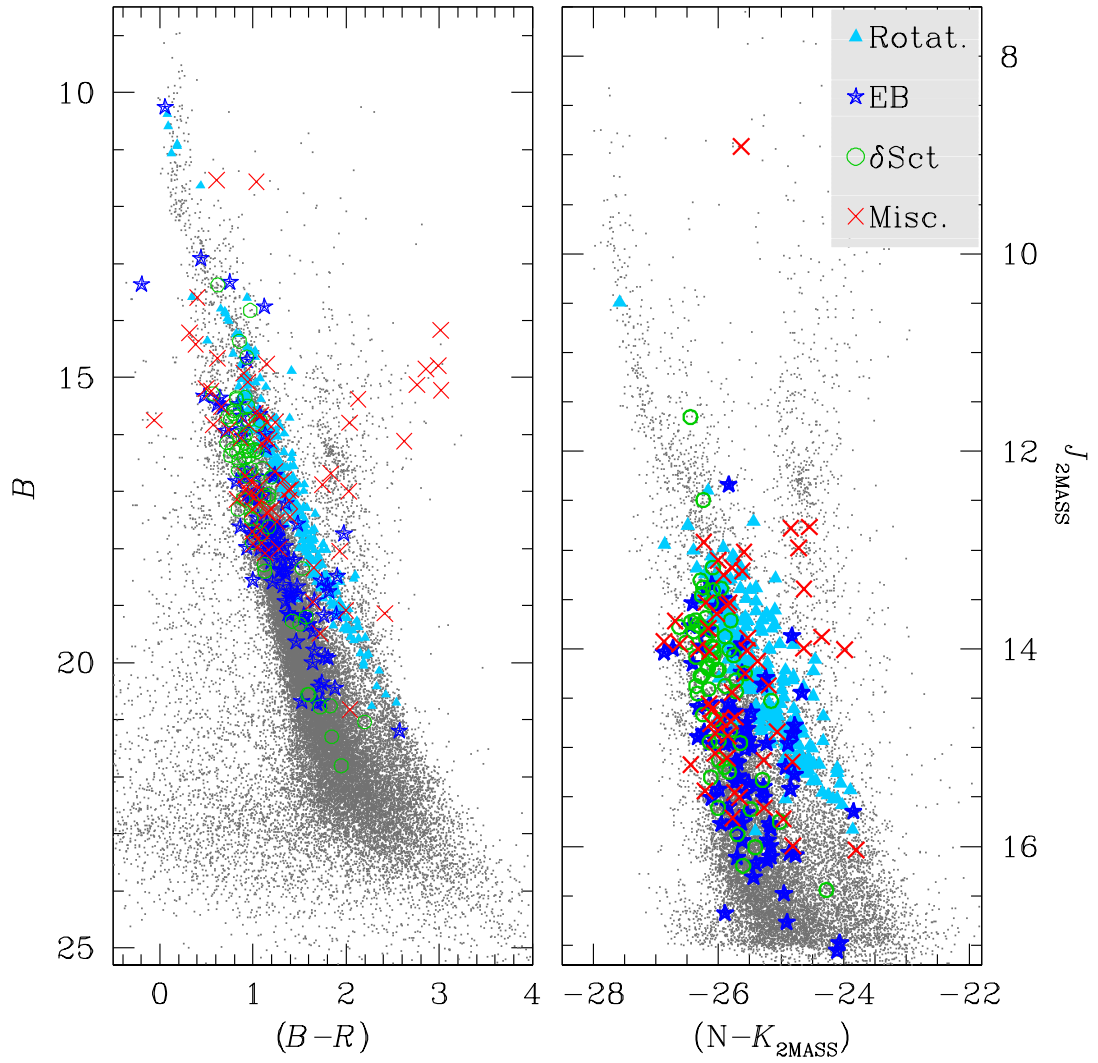

Figure 6.10: B vs. $(B{-}R)$ (*left panel*) and $J_{2\mathrm{MASS}}$ vs. $(N\text{-}K_{2\mathrm{MASS}})$ (*right panel*) CMDs. The variable stars are displayed as follows: azure triangles are rotational stars, blue stars are eclipsing binaries, green circles are δ Sct and red crosses are other variables such as long period, nonperiodic, etc.

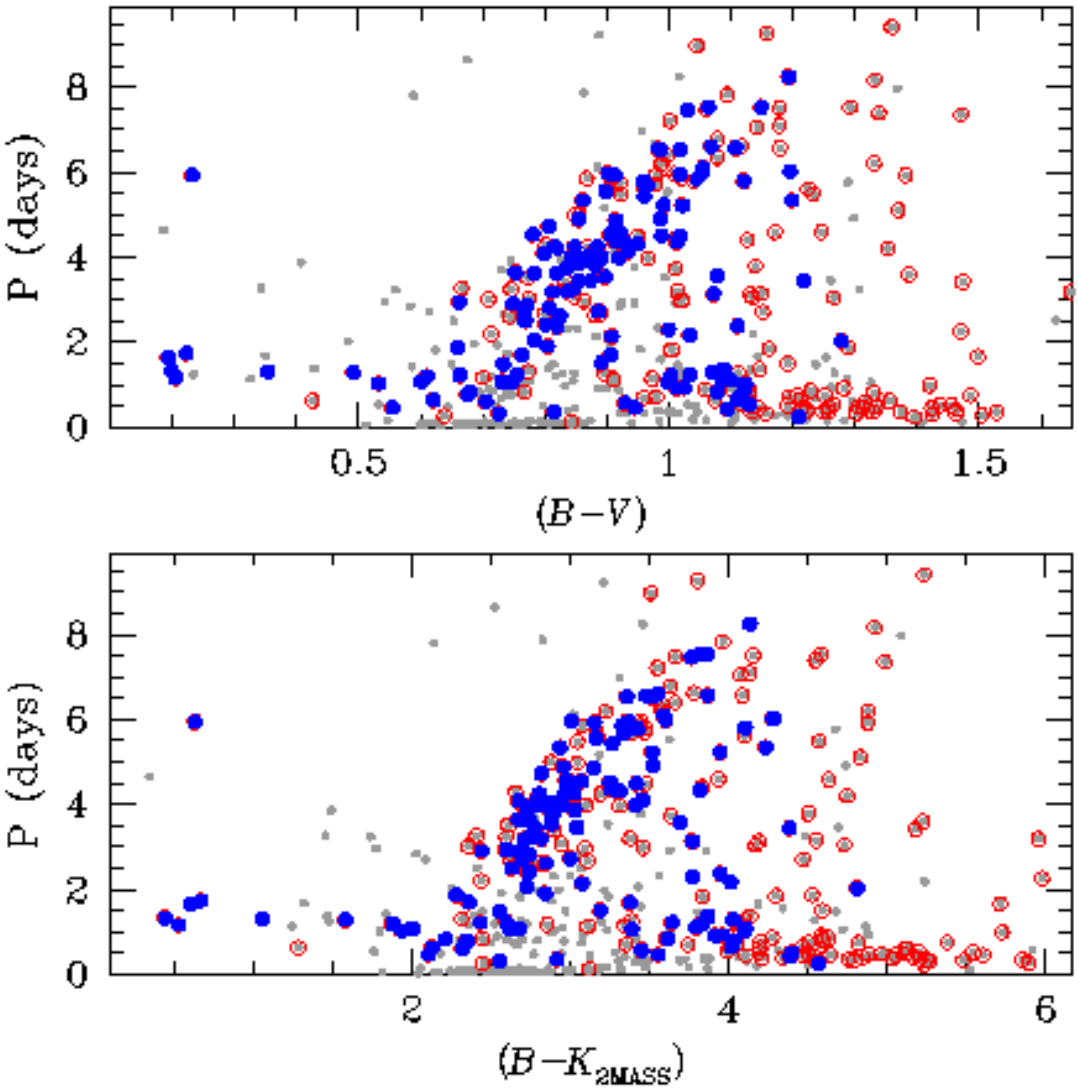

Figure 6.11: Period vs $(B-V)$ (*top panel*) and $(B\text{-}K_{2\mathrm{MASS}})$ (*bottom panel*) for all the variables (grey dots). Red circles mark the rotating stars, that define the colour-period relation for the stars of M 35. The rotating stars with a membership probability $\geq 50\%$ are displayed in blue.

6.4.3 The Electronic Material

The catalogue of all variable stars is available electronically (or upon request to the authors). The catalogue contains the following information: Col. (1) displays is the identification number of the variable in this work; Cols. (2) and (3) are the J2000 equatorial coordinates in decimal degrees; Col. (4) contains the period in days; Cols. (5) to (11) are the calibrated B V R, instrumental N and calibrated $J_{\rm 2MASS}$ $H_{\rm 2MASS}$ $K_{\rm 2MASS}$ magnitudes (when magnitudes are not available in a particular filter, they are denoted as 0.0); Col (12) provides the variable type; Col (13) and (14) give the membership probabilities for M 35 and NGC 2158 stars from Dias et al. (2014) (when the membership probability is not available, it is denoted as -99.999); Cols. (15)–(20) give the identification ID in other published catalogues, specifically: Kim et al. 2004, Hu et al. 2005, Mochejska et al. 2006, Meibom, Mathieu & Stassun 2009, Jeon & Lee 2010 and GCVS (in Table 6.2 we combined cols. (15)–(20) to best fit the table in the manuscript).

For each star in the catalogue we release an astrometrized $43\farcs1 \times 43\farcs1$ finding chart for each available filter.

A catalogue of all sources detected in N and R filters is also electronically available. In this catalogue, Cols. (1) and (2) are the J2000 equatorial coordinates in decimal degrees; Cols. (3)–(9) are the calibrated B V R $J_{\rm 2MASS}$ $H_{\rm 2MASS}$ $K_{\rm 2MASS}$ magnitudes and the instrumental N magnitudes. As mentioned in Sect. 6.2.1, the astrometrized stacks in $BVRN$ filters are also electronically available.

6.5 Conclusions

We present the first results of a long term photometric survey of OC stars conducted with the 67/92 cm Schmidt telescope at Cima Ekar, Asiago. In this paper, we focus on a field which includes the two open clusters M35 and NGC 2158. A total of 6996 58×38 arcmin^2 images in B, V, R, and white light (no filter) were collected over 2.4 years. We test four different approaches to the stellar photometry: aperture and PSF photometry on the original and neighbour-subtracted images. Aperture photometry on neighbour-subtracted images proves to be the most appropriate method to obtain light curves with the lowest photometric RMS. We also test different approaches to correct our photometry for systematic errors. Our final database includes 66 486 stars. We run different algorithms for the identification of variable stars: i) the Lomb-Scargle periodogram, ii) the Analysis of Variance periodogram, and iii) the Box-finding Least Square periodogram. We identify 519 variables: 97 eclipsing binaries (56 are new identifications), 284 rotational variables (122 new), 67 δ Scuti variables (45 are new), 69 long period or non periodic variables (50 of them are new), 1 RRLy and 1 δ Cep. Finally, we cross-correlate our variable star catalogue with previously published catalogues to obtain membership probabilities, and for cross-identification with already know variables. The catalogue with coordinates, B, V, R, 2MASS magnitudes, membership and cross-identification with known variables is made electronically available. The electronic material includes the B, V, R and white light stacked images. For each variable, a 43.1×43.1 arcsec^2 finding chart is also made available. M 35 and NGC 2158 are within the field of *Campaign-0* of the *Kepler 2 Mission*. Our survey will therefore complement —and extend in time— the light curves of variable (and not variable) stars covered by K2.

Chapter 7

Photometric observations in Open Cluster M67 (NGC 2682)

During the programme "The Asiago Pathfinder for HARPS-N" (see chapter 6), photometric series of stars in 5 open clusters were collected using the Asiago Schmidt 67/92 cm telescope. In this chapter I will show the results regarding stars belonging the solar-age, solar-metallicity open cluster M 67. The results are part of the work by Nardiello et al. (2016) of which I am co-author. We have analysed the light curves of the sources within this cluster, detecting 68 variables (of which 43 new detection). We derived also proper motions for a great number of stars, reaching astrometric precisions of $\sim 0.7\,\mathrm{mas\,yr^{-1}}$.

7.1 Schmidt 67/92cm - Facilities and observations

All images of the OC M 67 [(α, δ)=$(08^{\mathrm{h}}51^{\mathrm{m}}18^{\mathrm{s}}, +11°48'00'')$] were collected with the Asiago 67/92 cm Schmidt Telescope located on Mount Ekar (longitude 11.°5710 E, latitude 45.°8430 N, altitude 1370 m), that belongs to the Astronomical Observatory of Padova (OAPD), which is part of the Istituto Nazionale di Astrofisica (INAF). At the focus of the Schmidt telescope there is a SBIG STL-11000M camera, equipped with a Kodak KAI-11000M detector (4050 × 2672 pixel, field of view: $58 \times 38\,\mathrm{arcmin^2}$, pixel scale: $862.5\,\mathrm{mas\,pixel^{-1}}$). The characteristics of the telescope and the CCD are described in details in Paper I.

The OC M 67 is one of the four fields observed under the long-term observing programme APHN (PI: Bedin), aimed to characterise variable stars and transiting-exoplanet candidates in five OCs.

As in the case of M35 and NGC 2158 (Paper I), in the first observing season (2012) M 67 data were collected in white light (hereafter indicated with filter N, where N stands for 'None'), with exposure time of 120 s, and 60 s (during the almost-full moon nights); during the second (2013) and the third season (2014) we collected 180 s+15 s R-filter and 180 s B-filter images. Finally, during the fourth season (2015), the observations were carried out in I-band (240 s+15 s) and V-band (240 s). In table 7.1 we give a log of the observations, while in Fig. 7.1 we show the histograms of the number of images taken during all the observing seasons.

All images are stored in the INAF national archive in Trieste[1].

[1] http://ia2.oats.inaf.it/archives/asiago

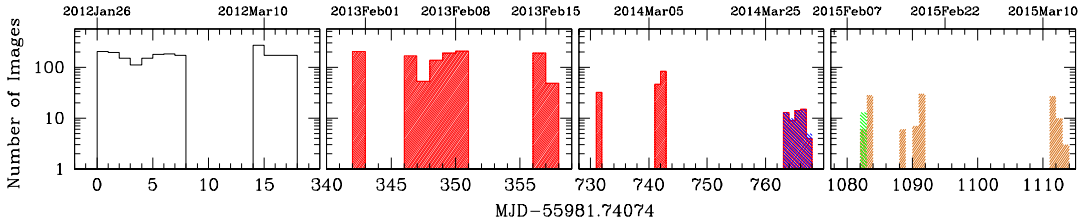

Figure 7.1: Histogram of the number of images per night collected during the four campaigns of our programme. The white histogram refers to observations in white light; the red, blue, green, and mango histograms refer to observations in the R, B, V, and I filters, respectively.

Filter	**# Images**	**Exp. Time** (s)	**FWHM** (arcsec)	**Median FWHM** (arcsec)
B	57	180	1.20–1.86	1.47
V	13	240	1.59–2.31	1.90
R	588	15	1.33–7.66	3.17
	822	180		
I	39	15	1.44–6.16	2.98
	78	240		
N	232	60	1.70–7.38	3.41
	1878	120		

Table 7.1: Log of observations.

7.2 Data reduction

7.2.1 Pre-reduction and Extraction LCs

For the data reduction, we used the software described in detail in Paper I. For each image we made a grid of 9×5 spatially-varying, empirical point spread functions (PSFs), one for each of the 45 regions in which we divided the field of view (FOV); the software is similar to that developed by Anderson et al. (2006) for the Wide Field Imager (WFI) mounted at the ESO / Max-Planck-Gesellschaft (MPG) 2.2m telescope.

For any location on the detector, the best PSF model is obtained by a bilinear interpolation of the four closest PSFs and it is used to measure the position and the flux of the stars in each image.

We transformed stellar positions in all the images into the reference frame of the best image[2] in filter N (ID `SC02906`). For each filter, we obtained the photometric zero-points between the single images and the best image in that filter (ID: `SC02906` for N-filter, `SC37438` for R-filter, `SC37437` for B-filter, `SC46181` for V-filter, `SC46722` for I-filter).

We created a stacked, high-signal-to-noise ratio (SNR) image ('stack') of the field for each filter. Using the N-filter stack, characterised by the highest SNR (Fig. 7.2), and the software used for single images, we derived an improved star list. We purged this star list from false detection using the `qfit` parameter (a diagnostic related to the quality of the PSF fit, Anderson et al. 2008) and the procedure described in Libralato et al. (2014). The purged star list contains 6905 sources, and we used it as the master star list (MSL) for the extraction of the light curves (LCs). The MSL contains stars with $V \lesssim 25$; faint enough to reach the magnitude of the faintest white dwarfs (WDs) detected along the cooling sequence of M 67 by Bellini et al. (2010). The three bottom panels of Fig. 7.2 are centred on the three WDs shown in Fig. 2 of Bellini et al. (2010). The bottom-right panel of Fig. 7.2 shows the faintest WD ($V \sim 24$) identified by the same authors. We extracted the $BVRI$-photometry of the 6905 sources in our catalogue by using the $BVRI$-stacked images. We calibrated the magnitudes by matching our catalogue to the Stetson Standard star catalogue (Stetson 2000). We derived calibration equations by means of least squares fitting of straight lines using magnitudes and colours.

For the LCs extraction, we used the software developed and described in details in Paper I. Briefly, by using (i) the MSL catalogue, (ii) the PSFs, and (iii) the six-parameters linear transformations between the MSL and the single-image catalogues, for each target star within the MSL, the software extracts LCs in two parallel versions: a first one from the original images, and a second one from images where the neighbours close to the target star were PSF-fitted and subtracted. In both versions, our tool extracts the flux of the target star using PSF fitting and aperture photometry. As in Paper I, for aperture photometry we adopted a dynamical aperture that depends on the Full Width Half Maximum (FWHM), with radius r=1.0 $\times$ FWHM. Therefore, for each star in the MSL, four light curves are generated: PSF with/without neighbour-subtracted and aperture with/without neighbour-subtracted.

7.2.2 Detrend of the LCs: DeTrendy

In order to remove residual systematic errors from the LCs, we followed the procedure used in Paper I and described in detail in Nascimbeni et al. (2014). For each target star in each image, our algorithm computes local, weighted photometric zero-points using selected reference stars (generally the stars with the best rms at a given magnitude). The weights are a function of the relative on-sky position and of the magnitude difference between the target and the reference

[2]The "best image" is characterised by the minimum of the product between airmass and seeing.

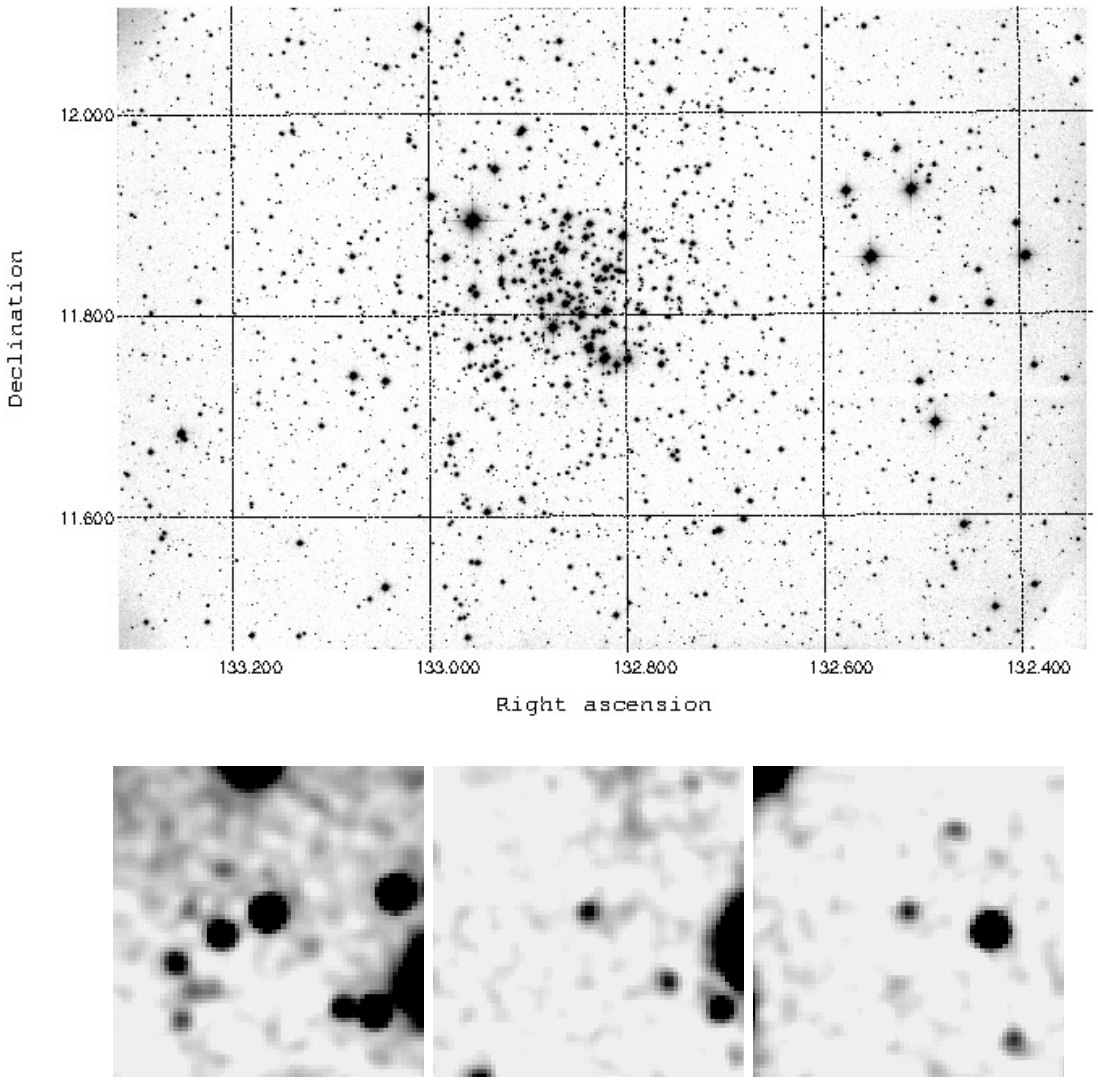

Figure 7.2: *Top:* N-filter stacked image of M 67 obtained with our data. *Bottom:* zoom-in of the N-filter stacked image centred on the three white dwarfs shown in Fig. 2 of Bellini et al. (2010).

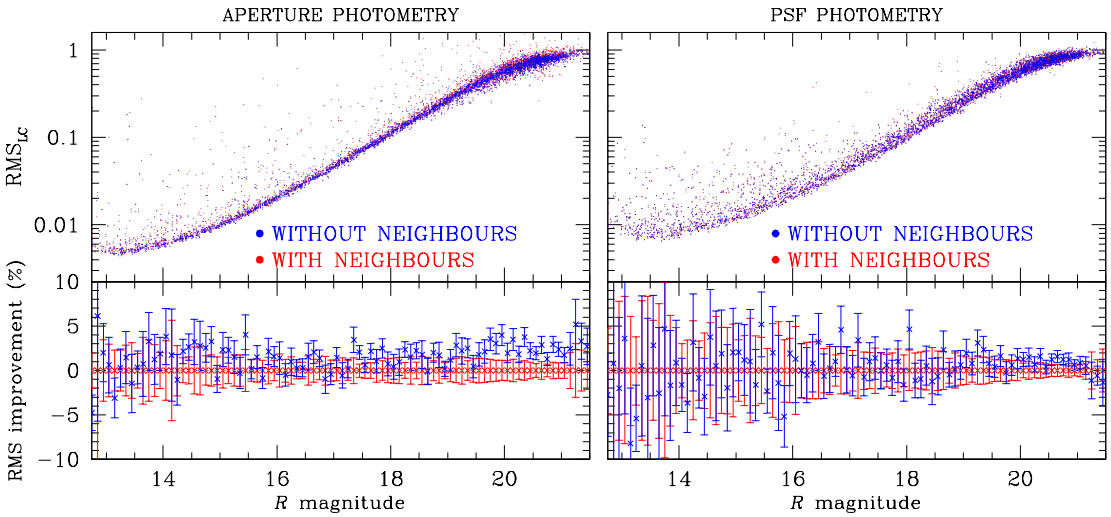

Figure 7.3: Photometric rms, obtained from original 180s R images (red) and from images after neighbour-subtraction (blue), for both aperture photometry (left) and PSF photometry (right). The lower panels show the percentage improvement of the neighbour-subtraction algorithm on the rms, averaged over 0.1-mag bins.

star. The software also computes a global zero-point correction, which – on average – provides worse residuals than the local zero-point correction, as also found in Paper I.

In Fig. 7.3 we show the photometric rms of the LCs derived from all the photometric methods (aperture with or without neighbours and PSF-fitting with or without neighbours). Even if the field of M 67 is relatively loose (if compared to the field analysed in Paper I) the photometry on images after neighbours subtraction is better than the photometry on original images, as the rms-scatter is lower and the rms-improvement is – on average – $\sim 3\%$ in the case of aperture photometry, and $\sim 1\%$ in the case of PSF-fitting photometry. Images were slightly de-focused to avoid saturation of main sequence (MS) turn off stars, therefore it was difficult to perfectly model the PSFs. This is also the reason why the rms PSF-fitting photometry is overall worse than the one associated to aperture photometry, as shown in Fig. 7.4.

7.3 Analysis of variability

In order to detect candidate variables in our field, we used three different algorithms: the Generalized Lomb-Scargle (GLS) periodogram (Zechmeister & Kürster 2009), suitable for sinusoidal signals; the Analysis of Variance (AoV) periodogram (Schwarzenberg-Czerny 1989), useful to detect all variable types; the Box-fitting Least-Squares (BLS) periodogram (Kovács, Zucker & Mazeh 2002), effective for searching box-like dips in an otherwise flat or nearly flat LC, such as eclipsing binaries (EBs) and planetary transits. All the algorithms are part of the publicly available code `VARTOOLS` v.1.32[3] (Hartman et al. 2008). We used the output parameters associated to each algorithm for excluding the sources in our catalogue that have low probabilities to be variable in our data. In order to isolate the candidate variable stars, we used the procedure

[3]http://www.astro.princeton.edu/∼jhartman/vartools.html

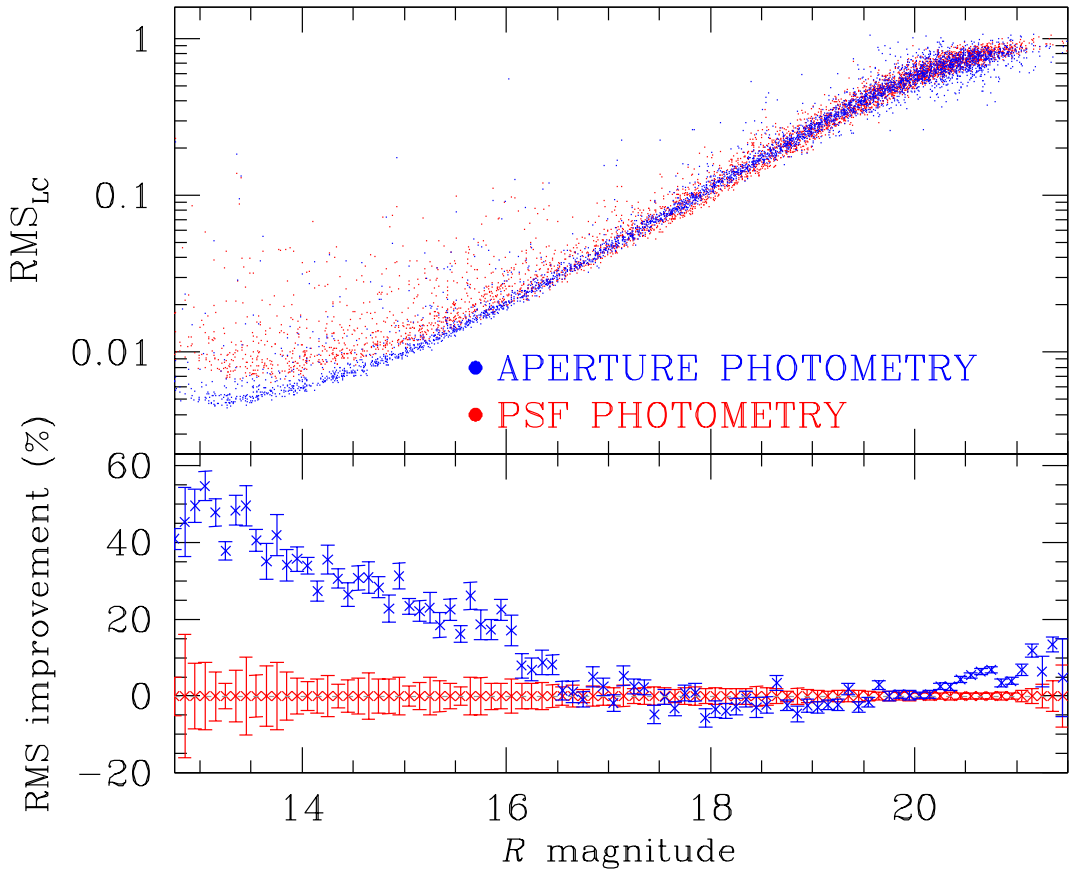

Figure 7.4: As in Fig. 7.3, but comparing aperture and PSF photometries on neighbour-subtracted images.

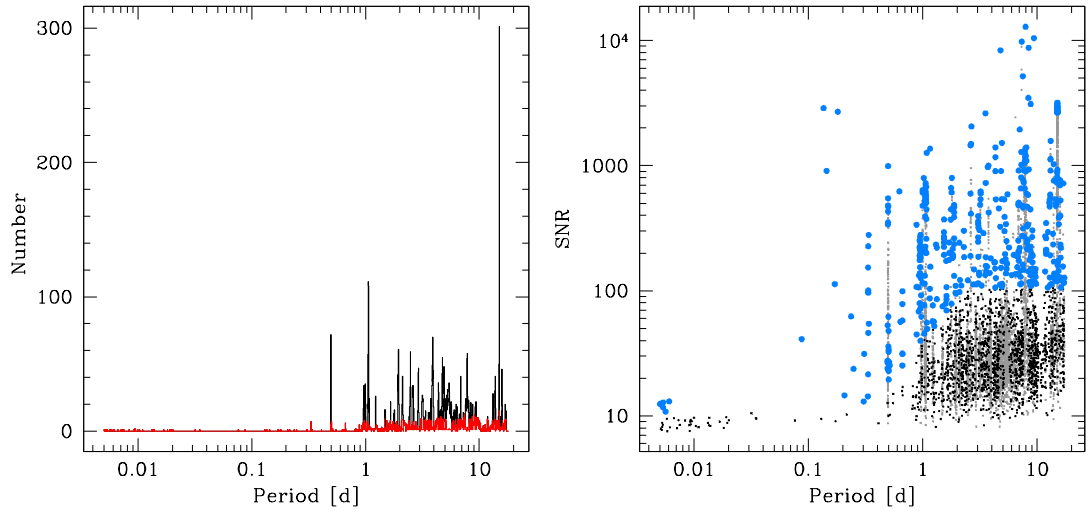

Figure 7.5: Procedure followed for the extraction of candidate variable stars. Left panel: distribution of the periods obtained from all the light curves before (black) and after (red) spikes suppression. Right panel:the AoV SNR as a function of the period of the light curves: in grey all the stars, in black the stars after spikes suppression, and in azure the suspected variables.

described in Paper I and summarised in Fig. 7.5.

From the histograms of the detected periods for all the LCs, we removed the spikes (saving the stars with high SNR, left panel of Fig. 7.5). The spikes are associated to spurious periods due to systematic effects, such as instrumental and atmospheric artefacts. In a second step, we selected by hand the candidate variables in the SNR versus period diagram (right panel of Fig. 7.5), and we visually inspected each of them.

We performed this procedure on neighbour-subtracted LCs, both for aperture and PSF photometries and for N and R LCs, identifying 68 real variable sources.

As in Paper I, we refined the periods using the following procedure: for each variable star, we normalised the R and N LC to zero, subtracting the 5σ-clipped median magnitude. Then, we merged the R and N normalised LCs, obtaining a LC with a temporal baseline of 764 days. We used again the `VARTOOLS` algorithms LS, AoV, and BLS to improve the period of the variable star. This procedure is useful only to improve the periods; it is not possible to extract any other scientific information from this normalised LC.

7.4 Results

In our catalogue there are 6905 sources that cover a field-of-view of ~ 0.612 degree^2 centred on M 67. In this catalogue we find 68 variables stars. All the variable stars are listed in Table 7.2; for each variable we provide the identification number (ID), the position, the period (if it is not irregular), and, when available, the magnitudes in N B V R I $J_{\rm 2MASS}$ $H_{\rm 2MASS}$ $K_{\rm 2MASS}$ bands, the membership probabilities as obtained in Sect. 7.4.1, and the radial velocities from Geller, Latham & Mathieu (2015).

Of these 68 variable stars, 25 variable stars have already been classified in other photometric works (Gilliland et al. 1991; Stassun et al. 2002; van den Berg et al. 2002; Sandquist & Shetrone

2003a,b; Stello et al. 2006, 2007; Bruntt et al. 2007; Pribulla et al. 2008; Yakut et al. 2009) and/or in the General Catalogue of Variable Stars (GCVS, Samus & Antipin 2013). Other variable stars listed in literature catalogues, but not found in our variable catalogue, are bright objects extremely saturated in our data (even in short exposures) or just outside the Schmidt FOV.

Table 7.2: First 10 lines of the catalogue of variable stars.

ID	α	δ	P	N	B	V	R	I	J_{2MASS}	H_{2MASS}	K_{2MASS}	P_μ	RV[a]
	(degree)	(degree)	(day)									(%)	($km\,s^{-1}$)
(1)	(2)	(3)	(4)	(5)	(6)	(7)	(8)	(9)	(10)	(11)	(12)	(13)	(14)
10	132.48057	11.470550	6.61403975	-13.4283	15.6986	15.8312	14.8366	14.7724	13.665	13.276	13.262	90.5418	30.29
37	132.72530	11.480997	1.82830531	-10.526	20.3047	18.5991	17.7994	15.9833	14.631	13.999	13.724	2.3146	-1000.00
101	133.03346	11.503185	0.61441096	-9.9831	19.6606	18.757	18.0689	17.6468	16.401	15.96	15.59	14.8792	-1000.00
142	132.54111	11.514107	0.33958032	-9.3075	19.7992	19.3732	18.9384	18.9665	-99.999	-99.999	-99.999	44.9397	-1000.00
144	132.68428	11.515616	8.07609064	-13.5201	15.783	14.9577	14.7485	14.6447	13.572	13.167	13.079	0.347	55.34
193	133.08555	11.534070	5.01456608	-11.7733	17.9946	16.8831	16.339	15.7722	14.592	13.965	13.791	97.3684	-1000.00
207	133.09478	11.541483	10.8060368	-9.0553	-99.999	18.7736	18.9221	18.3115	16.559	15.826	15.243	49.6983	-1000.00
211	132.54888	11.540289	19.1807153	-14.0378	15.3067	14.4544	14.146	13.971	12.883	12.444	12.341	0.0	35.69
236	132.46906	11.551604	2.86317050	-16.0982	13.3535	12.4298	12.0711	11.9546	10.725	10.269	10.18	0.0	-15.61
239	132.55463	11.552562	6.75840156	-13.0745	16.1264	15.4163	15.1784	15.0959	14.076	13.766	13.733	0.0	13.22

Notes. [a]Geller, Latham & Mathieu (2015).

7.4.1 Inside M67: Proper motions and Membership probabilities

We used stellar proper motions to separate cluster members and field stars. The approach adopted to compute stellar positional displacement is the same as in many other works, e.g., Bedin et al. (2003); Anderson et al. (2006); Yadav et al. (2008); Bellini et al. (2010); Nardiello et al. (2015b), and Libralato et al. (2015b). Using six-parameter local transformations and a sample of likely cluster members (for example MS stars), we computed the displacement between the stellar positions in two different epochs, after been transformed into a common reference system. As first epoch, we used M 67 V-filter observations collected with the WFI mounted at the ESO/MPG 2.2 m telescope, on February 16th, 2000 ($t_{\rm I}$=2000.1). As second epoch we used the best 100 Schmidt R-images collected during the 2013 observational run ($t_{\rm II}$ ≃2013.1). The time baseline for the proper motion measurements is ∼13.0 yr.

Since we used likely cluster members to compute the coefficients of the six-parameter linear transformations, the stellar displacements are computed *relative* to the cluster mean motion. Therefore, by construction, the cluster distribution in the vector-point diagram (VPD) is centred around (0,0), while field stars, that have a different motion relative to that of the cluster, lie in a different region of the VPD (see Fig. 7.6).

The membership probabilities (MPs) of the stars in the M 67 FOV have already been calculated using both astrometry (e.g. Sanders 1977; Girard et al. 1989; Zhao et al. 1993; Yadav et al. 2008) and radial velocities (e.g Yadav et al. 2008; Pasquini et al. 2011; Geller, Latham & Mathieu 2015). Our final catalogue supplements the other works; we extracted the MPs in an homogeneous way for stars with $V \lesssim 19.5$ in a region of $58 \times 38\,\mathrm{arcmin}^2$.

There are different methods to derive stellar MPs. We chose that described by Balaguer-Núnez, Tian & Zhao (1998). Briefly, we derived the frequency function for both cluster (Φ_c) and field stars (Φ_f). We assumed that cluster distribution is centred at ($\mu_{\alpha\cos\delta,c}$,$\mu_{\delta,c}$) = (0.00,0.00) mas yr^{-1} with an intrinsic dispersion[4] of ($\sigma_{\mu_{\alpha\cos\delta,c}}$,$\sigma_{\mu_{\delta,c}}$) = (0.65,0.71) mas yr^{-1}. For field stars, we have ($\mu_{\alpha\cos\delta,f}$,$\mu_{\delta,f}$) = (9.34,−1.10) mas yr^{-1} and a dispersion of ($\sigma_{\mu_{\alpha\cos\delta,f}}$,$\sigma_{\mu_{\delta,f}}$) = (4.19,6.19) mas yr^{-1}. We ignored the spatial distribution of the two components and assumed that there is not a correlation between them (correlation coefficient γ is set to 0). We excluded from our calculation poorly-measured-proper-motion stars. The membership probability is then computed as:

$$P_\mu = \frac{\Phi_c}{\Phi_c + \Phi_f} \ .$$

Panel (a) of Fig. 7.6 shows the available MPs P_μ as a function of the magnitude V. The figure shows that we measured reliable MPs for stars with $V \lesssim 19.5$.

7.4.2 Colour-magnitude diagrams and light curves

In panel (b) of Fig. 7.6 we show the B versus $(B-I)$ CMD of M 67. In panels (a) and (b), we plot in black the likely cluster member stars, selected according to their proper motions (i.e. the stars inside the red circles in the VPD of panels c), in azure the stars rejected and those are likely field stars, and with green dots the variable stars found in this work. In panel (d), using the same colour-code, we plot the positions of the stars in our MSL field of view.

In panels (e) there are four examples of variable stars with $P_\mu > 97\%$. The LCs are normalised to the median magnitude. We plot in black the LC in N-filter and in red that in R-filter.

[4]The intrinsic dispersion is dominated by the positional errors and do not reflect the true intrinsic cluster dispersion.

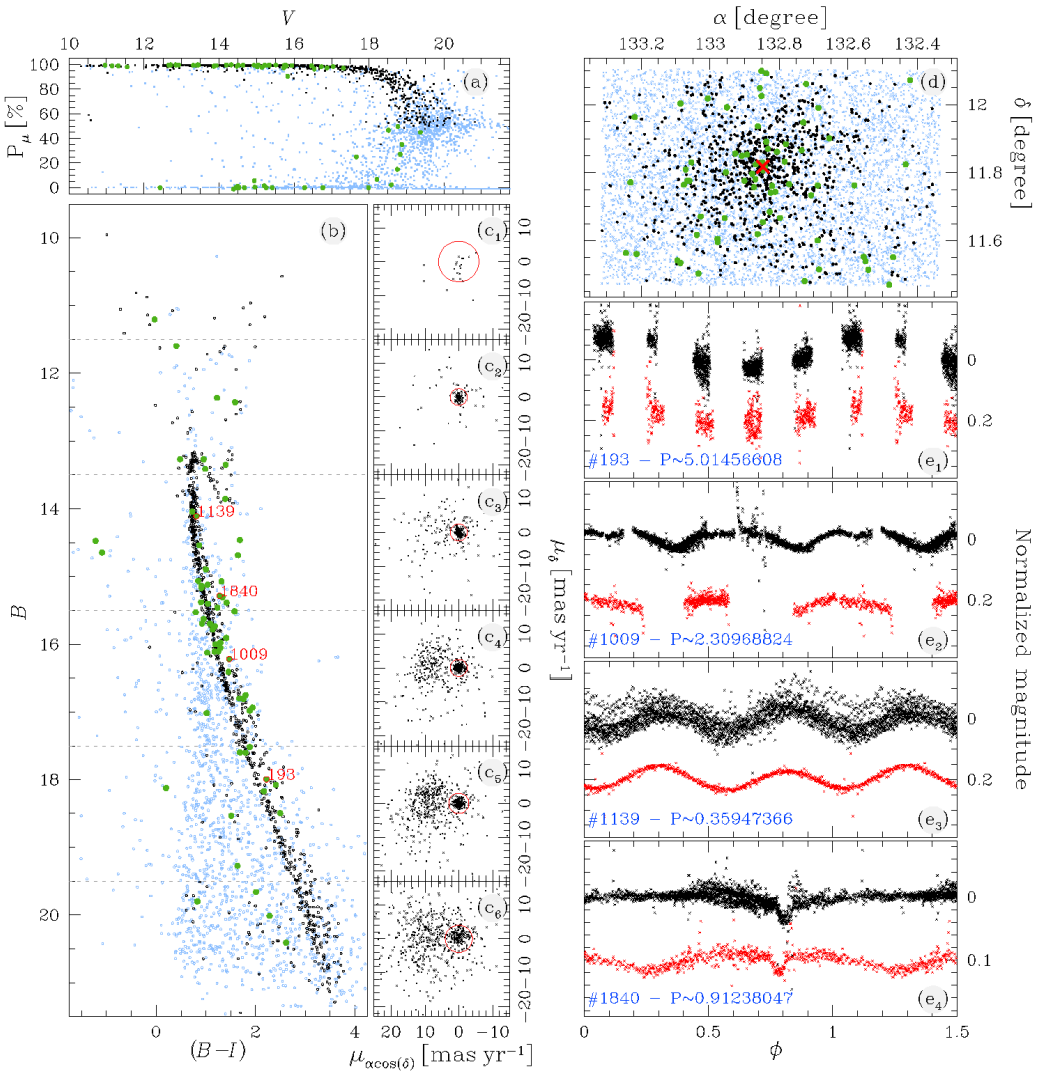

Figure 7.6: Panel (a): membership probabilities P_μ as a function of the V magnitude; panel (b): CMD B versus $(B-I)$ of M 67 stars in the MSL; panels (c): vector-point diagrams for the same stars as in panel (b) in the corresponding magnitude intervals. The cluster star proper motion distribution is centred around (0,0) ; panel (d): positions (α,δ) for all the stars in the Schmidt MSL. The red cross indicates the cluster centre (Yadav et al. 2008); panels (e): four examples of median-magnitude normalised LCs in filter N (black) and R (red). The four stars have $P_\mu > 97\%$. In panels (a), (b), and (d), we plot in black the likely cluster members, i.e. the stars inside the red circles in panels (c), in azure the likely field stars, and in green the variable stars found in this work. In panel (b) we highlight the variable stars shown in panels (e).

Panel (e_4) shows an eclipsing binary (ID #1840) that has never been photometrically observed, but that is in the sample of Geller, Latham & Mathieu (2015). From spectroscopic observations, they found that this is a double lined (SB2) eclipsing binary and also a X-ray source (X35 in the *ROSAT* catalogue, Belloni, Verbunt & Mathieu 1998). In our data, we probably observe only the primary eclipse, that has a box-like shape with a depth of 0.02 mag.

7.4.3 The Electronic Material

The catalogue of all the sources in our MSL is electronically available. The catalogue contains the following information: Cols (1) and (2) are the J2000.0 equatorial coordinates in decimal degrees; Cols (3) and (4) the positions in pixel on the N-filter stack; Cols (5)-(12) are the instrumental N, and the calibrated B V R I $J_{\rm 2MASS}$ $H_{\rm 2MASS}$ $K_{\rm 2MASS}$ magnitudes (when the magnitude is not available, it is flagged with -99.999); Col. (13) is the identification number (ID) of the star; Cols. (14) and (15) give the relative proper motions in mas yr^{-1} along ($\alpha \cos\delta, \delta$) direction (when it is not available, it is flagged with -999.9999); Col. (16) gives the membership probabilities P_μ (when it is not available, it is flagged with -1).

Along with the MSL, we release the catalogue of all variable stars found in this work. An example of the catalogue is Table 7.2: Col. (1) is the identification number (ID) of the variable star in our MSL; Cols (2) and (3) are the J2000.0 equatorial coordinates in decimal degree; Col. (4) contains the periods in day (when the star is irregular, the period is -99); Cols (5)-(12) are the instrumental N, and the calibrated B V R I $J_{\rm 2MASS}$ $H_{\rm 2MASS}$ $K_{\rm 2MASS}$ magnitudes (when the magnitude is not available, it is flagged with -99.999); Col. (13) gives the membership probabilities P_μ (when it is not available, it is flagged with -1); Col. (14) are the radial velocities measured by Geller, Latham & Mathieu (2015) (when the radial velocity measurement is not available, it is denoted as -1000). For each variable star, we also release the B R I N LCs.

Finally, we make the astrometrized stacks in B V R I N filters electronically available.

7.5 Conclusions

In this work we present the photometric results for the third target (M 67) of the photometric survey of OC stars conducted with the 67/92 cm Schmidt telescope at Mount Ekar, Asiago. We analysed a total of 3707 images in B, V, R, I and white light (no filter), collected over 3.1 years. We used the algorithms described in Nardiello et al. (2015a) to obtain a complete list of stars (6905 sources with magnitude $V \lesssim 25$) and to extract, detrend, and analyse the corresponding LCs. We identify 68 variable stars (43 of which are new). Combining Schmidt best data with WFI@2.2m MPG/ESO images (collected on 2000), we derived the relative proper motions and the membership probabilities for a great number of stars in our MSL. We release two electronic catalogues: the catalogue of variable stars, (containing coordinates, periods B, V, R, I, N, 2MASS magnitudes, membership probabilities, radial velocities) and the catalogue of all the sources in the Schmidt FOV (containing positions, B, V, R, I, N, 2MASS magnitudes, proper motions, membership probabilities). The electronic material includes the B, V, R, I, and white light stacked images and light curves of the identified variable stars.

The OC M 67 is in the field of the *K2 Mission-Campaign-5*. The released catalogue of M 67 sources will be an excellent input-list for the extraction of LCs from *K2* images. In this sense, our survey is preparatory to the analysis of *K2* data, and complements (and extends in time) the light curves of the stars covered by *K2*.

Chapter 8

Conclusions

In this thesis the principal focus was the photometric analysis of stellar light curves (LCs), to search variables and transiting planets. The study was carried out on crowded fields of five open clusters: M44, NGC 752, M35, NGC 2158, and M67.

All the results obtained was part of the photometric preparatory survey "The Asiago Pathfinder for HARPS-N" (APHN; PI: Bedin) aimed at characterising OCs, to be observed with the High Accuracy Radial velocity Planet Searcher for the Northern hemisphere (HARPS-N), mounted at the Telescopio Nazionale Galileo (TNG), or at creating astro-photometric master input catalogues for high-precision photometry of *Kepler* and *K2* data.

Starting from the extracted raw LCs, I applied different existing algorithms or I implemented new algorithms for detrending light curves, affected by systematic errors ("red noise"). I applied SYSREM algorithm and the Trending Filter Algorithm (TFA), from which I extracted a new algorithm, the Local Trending Filter Algorithm (LTFA). Also, I used the "DeTrendy" algorithm, created by my searching group.

After the detrending phase, I implemented the steps for the detection of variability. I used three different algorithms: the Generalised Lomb Scargle (GLS), the Analysis of Variance (AoV) and the Box-fitting Least Squares (BLS) algorithms. I used these three algorithms in synergy, in order to detect any kind of variability signal, from boxy signal of transiting phenomena of eclipsing binaries or extrasolar planets, to sinusoidal signal created by rotational variability, taken into account pulsating variables, eruptive variables and long periodical signals.

First of all, I analysed M44 field, using SuperWASP archive and own observations carried out at STELLA1 telescope, at Tenerife. From 31604 stars analysed, 484 variables were detected, 61 in the OC. No variables inside M44 are new. Instead, 299 new variables were detected in the field, principally eclipsing binaries and rotational variables.

A second analysis was done in NGC 752 field, using again the SuperWASP archive. Inside the OC, 3 new variables were detected, and 43 new variables are in the field.

Another photometric analysis was carried out in a unique field including M35 and NGC2158. The observations were carried out at 67/92cm Schmidt Telescope at Asiago Cima Ekar. From 66486 stars, 519 variables are detected and 273 are new variables. Inside M35 were detected 248 variables, and in NGC 2158 were detected 9 variables.

At least, M67 was analysed, using again observations at Schmidt Telescope. From 6905 stars, 68 variables were detected, and 43 are new variables.

In the future, this analysis of LC detrending and variability detection could significantly improve. Next steps will be the analysis of other OCs, such as NGC6791, NGC6811, NGC6819, NGC6866, M45 (Pleiades), and Hyades, interesting because studied also with *Kepler* and *K2*

missions; these analyses are carried on in order to characterise the stellar clusters for follow-up, for example, with HARPS-N at Telescopio Nazionale Galileo (TNG).

Bibliography

Agol E., Steffen J., Sari R., Clarkson W., 2005, MNRAS, 359, 567

Agüeros M. A. et al., 2011, ApJ, 740, 110

Anderson J., Bedin L. R., Piotto G., Yadav R. S., Bellini A., 2006, A&A, 454, 1029

Anderson J. et al., 2008, AJ, 135, 2114

Auvergne M. et al., 2009, A&A, 506, 411

Bakos G., Noyes R. W., Kovács G., Stanek K. Z., Sasselov D. D., Domsa I., 2004, PASP, 116, 266

Bakos G. Á. et al., 2007, ApJ, 656, 552

Bakos G. Á. et al., 2009, in IAU Symposium, Vol. 253, IAU Symposium, Pont F., Sasselov D., Holman M. J., eds., pp. 21–27

Balaguer-Núnez L., Tian K. P., Zhao J. L., 1998, A&AS, 133, 387

Bartašiūtė S., Janusz R., Boyle R. P., Philip A. G. D., 2011, Baltic Astronomy, 20, 27

Bedin L. R., Piotto G., King I. R., Anderson J., 2003, AJ, 126, 247

Bellini A., Anderson J., Bedin L. R., 2011, PASP, 123, 622

Bellini A., Bedin L. R., 2010, A&A, 517, A34

Bellini A. et al., 2010, A&A, 513, A50

Belloni T., Verbunt F., Mathieu R. D., 1998, A&A, 339, 431

Bertin E., Arnouts S., 1996, A&AS, 117, 393

Bond I. A. et al., 2001, MNRAS, 327, 868

Bond I. A. et al., 2004, ApJ, 606, L155

Borucki W. et al., 2008, in IAU Symposium, Vol. 249, IAU Symposium, Sun Y.-S., Ferraz-Mello S., Zhou J.-L., eds., pp. 17–24

Borucki W. et al., 2004, in ESA Special Publication, Vol. 538, Stellar Structure and Habitable Planet Finding, Favata F., Aigrain S., Wilson A., eds., pp. 177–182

Borucki W. J. et al., 2010, Science, 327, 977

Bouchy F., Sophie Team, 2006, in Tenth Anniversary of 51 Peg-b: Status of and prospects for hot Jupiter studies, Arnold L., Bouchy F., Moutou C., eds., pp. 319–325

Broeg C. et al., 2013, in European Physical Journal Web of Conferences, Vol. 47, European Physical Journal Web of Conferences, p. 03005

Brogaard K. et al., 2012, A&A, 543, A106

Brown T. M., 2008, in Extrasolar Planets, Deeg H., Belmonte J. A., Aparicio A., eds., p. 65

Brown T. M., Latham D. W., Everett M. E., Esquerdo G. A., 2011, AJ, 142, 112

Brucalassi A. et al., 2014, A&A, 561, L9

Bruntt H. et al., 2007, MNRAS, 378, 1371

Butters O. W. et al., 2010, A&A, 520, L10

Chatterjee S., Ford E. B., Geller A. M., Rasio F. A., 2012, MNRAS, 427, 1587

Chauvin G., Lagrange A.-M., Dumas C., Zuckerman B., Mouillet D., Song I., Beuzit J.-L., Lowrance P., 2004, A&A, 425, L29

Collier Cameron A. et al., 2007, MNRAS, 380, 1230

Cosentino R. et al., 2014, in Society of Photo-Optical Instrumentation Engineers (SPIE) Conference Series, Vol. 9147, Society of Photo-Optical Instrumentation Engineers (SPIE) Conference Series, p. 91478C

Cosentino R. et al., 2012, in Society of Photo-Optical Instrumentation Engineers (SPIE) Conference Series, Vol. 8446, Society of Photo-Optical Instrumentation Engineers (SPIE) Conference Series, p. 84461V

Covino E. et al., 2013, A&A, 554, A28

Cumming A., Butler R. P., Marcy G. W., Vogt S. S., Wright J. T., Fischer D. A., 2008, PASP, 120, 531

Daniel S. A., Latham D. W., Mathieu R. D., Twarog B. A., 1994, PASP, 106, 281

de Bruijne J. H. J., 2012, Ap&SS, 341, 31

Deeg H., 1998, in Astronomical Society of the Pacific Conference Series, Vol. 134, Brown Dwarfs and Extrasolar Planets, Rebolo R., Martin E. L., Zapatero Osorio M. R., eds., p. 216

Deeming T. J., 1975, Ap&SS, 36, 137

Delorme P., Collier Cameron A., Hebb L., Rostron J., Lister T. A., Norton A. J., Pollacco D., West R. G., 2011, MNRAS, 413, 2218

Devor J., 2005, ApJ, 628, 411

Dias W. S., Monteiro H., Caetano T. C., Lépine J. R. D., Assafin M., Oliveira A. F., 2014, A&A, 564, A79

Díaz R. F. et al., 2015, ArXiv e-prints

Douglas S. T. et al., 2014, ApJ, 795, 161

Doyle L. R., 2008, in Extrasolar Planets, Deeg H., Belmonte J. A., Aparicio A., eds., p. 1

Drake A. J. et al., 2014, ApJS, 213, 9

Ducourant C., Teixeira R., Chauvin G., Daigne G., Le Campion J.-F., Song I., Zuckerman B., 2008, A&A, 477, L1

Dumusque X. et al., 2015, ApJ, 814, L21

Eastman J., Siverd R., Gaudi B. S., 2010, PASP, 122, 935

Fischer D. A., Valenti J., 2005, ApJ, 622, 1102

Fortier A., Beck T., Benz W., Broeg C., Cessa V., Ehrenreich D., Thomas N., 2014, in Proc. SPIE, Vol. 9143, Space Telescopes and Instrumentation 2014: Optical, Infrared, and Millimeter Wave, p. 91432J

Geller A. M., Latham D. W., Mathieu R. D., 2015, AJ, 150, 97

Gilliland R. L., Baliunas S. L., 1987, ApJ, 314, 766

Gilliland R. L. et al., 1991, AJ, 101, 541

Girard T. M., Grundy W. M., Lopez C. E., van Altena W. F., 1989, AJ, 98, 227

Hartman J. D., Gaudi B. S., Holman M. J., McLeod B. A., Stanek K. Z., Barranco J. A., Pinsonneault M. H., Kalirai J. S., 2008, ApJ, 675, 1254

Hartman J. D. et al., 2009, ApJ, 695, 336

Hearnshaw J. B. et al., 2006, in The 9th Asian-Pacific Regional IAU Meeting, Sutantyo W., Premadi P. W., Mahasena P., Hidayat T., Mineshige S., eds., p. 272

Holman M. J., Murray N. W., 2005, Science, 307, 1288

Horne J. H., Baliunas S. L., 1986, ApJ, 302, 757

Howell S. B. et al., 2014, PASP, 126, 398

Hu J.-H., Ip W.-H., Zhang X.-B., Jiang Z.-J., Ma J., Zhou X., 2005, Chinese J. Astron. Astrophys., 5, 356

Irwin A. W., Campbell B., Morbey C. L., Walker G. A. H., Yang S., 1989, PASP, 101, 147

Janes K., 1996, J. Geophys. Res., 101, 14853

Jeon Y.-B., Lee H.-R., 2010, Publication of Korean Astronomical Society, 25, 167

Kane S. R., Collier Cameron A., Horne K., James D., Lister T. A., Pollacco D. L., Street R. A., Tsapras Y., 2004, MNRAS, 353, 689

Khalaj P., Baumgardt H., 2013, MNRAS, 434, 3236

Kharchenko N. V., Piskunov A. E., Schilbach E., Röser S., Scholz R.-D., 2013, A&A, 558, A53

Kholopov P. et al., 1985a, General Catalogue of Variable Stars, Vol. 1

Kholopov P. et al., 1985b, General Catalogue of Variable Stars, Vol. 2

Kholopov P., Samus' N., Durlevich O., Kazarovets E., Kireeva N., Tsvetkova T., 1990, General Catalogue of Variable Stars, Vol. 4

Kholopov P. et al., 1987, General Catalogue of Variable Stars, Vol. 3

Kim H.-J., Park H.-S., Kim S.-L., Jeon Y.-B., Lee H., 2004, Information Bulletin on Variable Stars, 5558, 1

Kipping D. M., 2009, MNRAS, 392, 181

Koch D. G. et al., 2010, ApJ, 713, L79

Korhonen H., Strassmeier K. G., Granzer T., Weber M., Staude A., Schwope A. D., Andersen M. I., Järvinen A. S., 2007, in Astronomical Society of the Pacific Conference Series, Vol. 366, Transiting Extrapolar Planets Workshop, Afonso C., Weldrake D., Henning T., eds., p. 93

Kovács G., Bakos G., Noyes R. W., 2005, MNRAS, 356, 557

Kovács G. et al., 2014, MNRAS, 442, 2081

Kovács G., Zucker S., Mazeh T., 2002, A&A, 391, 369

Kraus A. L., Hillenbrand L. A., 2007, AJ, 134, 2340

Latham D. W., Stefanik R. P., Mazeh T., Mayor M., Burki G., 1989, Nature, 339, 38

Léger A. et al., 2009, A&A, 506, 287

Libralato M., Bedin L. R., Nardiello D., Piotto G., 2015a, ArXiv e-prints

Libralato M. et al., 2015b, MNRAS, 450, 1664

Libralato M., Bellini A., Bedin L. R., Piotto G., Platais I., Kissler-Patig M., Milone A. P., 2014, A&A, 563, A80

Lomb N. R., 1976, Ap&SS, 39, 447

Lovis C., Mayor M., 2007, A&A, 472, 657

Malavolta L. et al., 2016

Mancini L., 2013, in Protostars and Planets VI Posters

Marvasti F., ed., 2001, Nonuniform Sampling, Theory and Practice, 1st edn. Springer US

Mayor M. et al., 2003, The Messenger, 114, 20

Mayor M., Queloz D., 1995, Nature, 378, 355

Meibom S., Kepler Team, 2013, in American Astronomical Society Meeting Abstracts, Vol. 221, American Astronomical Society Meeting Abstracts #221, p. #231.04

Meibom S., Mathieu R. D., Stassun K. G., 2009, ApJ, 695, 679

Mermilliod J.-C., Mayor M., Udry S., 2009, A&A, 498, 949

Mighell K. J., 1999, in Astronomical Society of the Pacific Conference Series, Vol. 189, Precision CCD Photometry, Craine E. R., Crawford D. L., Tucker R. A., eds., p. 50

Mochejska B. J. et al., 2006, AJ, 131, 1090

Mortier A. et al., 2015, ArXiv e-prints

Moutou C., Deleuil M., 2015, ArXiv e-prints

Murray C. D., Dermott S. F., 1999, Solar system dynamics

Muterspaugh M. W. et al., 2010, AJ, 140, 1657

Nardiello D. et al., 2015a, MNRAS, 447, 3536

Nardiello D., Libralato M., Bedin L. R., Piotto G., Ochner P., Cunial A., Borsato L., Granata V., 2016, MNRAS, 455, 2337

Nardiello D., Milone A. P., Piotto G., Marino A. F., Bellini A., Cassisi S., 2015b, A&A, 573, A70

Nascimbeni V. et al., 2014, MNRAS, 442, 2381

Nascimbeni V. et al., 2013, A&A, 549, A30

Nascimbeni V., Piotto G., Bedin L. R., Damasso M., 2011, A&A, 527, A85

Pasquini L., Melo C., Chavero C., Dravins D., Ludwig H.-G., Bonifacio P., de La Reza R., 2011, A&A, 526, A127

Pepe F. et al., 2002, The Messenger, 110, 9

Pepper J., Stanek K. Z., Pogge R. W., Latham D. W., DePoy D. L., Siverd R., Poindexter S., Sivakoff G. R., 2008, AJ, 135, 907

Perryman M., Hartman J., Bakos G. Á., Lindegren L., 2014, ApJ, 797, 14

Perryman M. A. C., 2000, Reports on Progress in Physics, 63, 1209

Piskunov A. E., Schilbach E., Kharchenko N. V., Röser S., Scholz R.-D., 2007, A&A, 468, 151

Pojmański G., 2003, Acta Astron., 53, 341

Pollacco D. L. et al., 2006, PASP, 118, 1407

Pont F., Zucker S., Queloz D., 2006, MNRAS, 373, 231

Press W. H., Rybicki G. B., 1989, ApJ, 338, 277

Press W. H., Teukolsky S. A., Vetterling W. T., Flannery B. P., 1992, Numerical recipes in FORTRAN. The art of scientific computing

Pribulla T. et al., 2008, MNRAS, 391, 343

Pribulla T., Rucinski S. M., Kuschnig R., Ogłoza W., Pilecki B., 2009, MNRAS, 392, 847

Queloz D. et al., 2009, A&A, 506, 303

Queloz D., Mayor M., Naef D., Santos N., Udry S., Burnet M., Confino B., 2000, in From Extrasolar Planets to Cosmology: The VLT Opening Symposium, Bergeron J., Renzini A., eds., p. 548

Quinn S. N. et al., 2012, ApJ, 756, L33

Quinn S. N. et al., 2014, ApJ, 787, 27

Rauer H. et al., 2014, Experimental Astronomy, 38, 249

Ricker G. R. et al., 2014, in Proc. SPIE, Vol. 9143, Space Telescopes and Instrumentation 2014: Optical, Infrared, and Millimeter Wave, p. 914320

Rucinski S. M., Kaluzny J., Hilditch R. W., 1996, MNRAS, 282, 705

Sako T. et al., 2008, Experimental Astronomy, 22, 51

Samus N. N., Antipin S. V., 2013, Astronomical and Astrophysical Transactions, 28, 49

Samus N. N., Durlevich O. V., et al., 2009, VizieR Online Data Catalog, 1

Sanders W. L., 1977, A&AS, 27, 89

Sandquist E. L., Shetrone M. D., 2003a, AJ, 126, 2954

Sandquist E. L., Shetrone M. D., 2003b, AJ, 125, 2173

Sato B. et al., 2007, ApJ, 661, 527

Scargle J. D., 1982, ApJ, 263, 835

Scholz A., Irwin J., Bouvier J., Sipőcz B. M., Hodgkin S., Eislöffel J., 2011, MNRAS, 413, 2595

Schwarzenberg-Czerny A., 1989, MNRAS, 241, 153

Skrutskie M. F. et al., 2006, AJ, 131, 1163

Smith A. M. S., WASP Consortium, 2014, Contributions of the Astronomical Observatory Skalnate Pleso, 43, 500

Song I., Schneider G., Zuckerman B., Farihi J., Becklin E. E., Bessell M. S., Lowrance P., Macintosh B. A., 2006, ApJ, 652, 724

Soszyński I. et al., 2014, Acta Astron., 64, 177

Sozzetti A., 2013, in European Physical Journal Web of Conferences, Vol. 47, European Physical Journal Web of Conferences, p. 15005

Stassun K. G., van den Berg M., Mathieu R. D., Verbunt F., 2002, A&A, 382, 899

Stello D. et al., 2006, MNRAS, 373, 1141

Stello D. et al., 2007, MNRAS, 377, 584

Sterken C., Jaschek C., 2005, Light Curves of Variable Stars

Stetson P. B., 2000, PASP, 112, 925

Struve O., 1952, The Observatory, 72, 199

Sumi T. et al., 2003, ApJ, 591, 204

Tamuz O., Mazeh T., Zucker S., 2005, MNRAS, 356, 1466

Tull R. G., 1998, in Society of Photo-Optical Instrumentation Engineers (SPIE) Conference Series, Vol. 3355, Optical Astronomical Instrumentation, D'Odorico S., ed., pp. 387–398

Udalski A., Kubiak M., Szymanski M., Kaluzny J., Mateo M., Krzeminski W., 1994, Acta Astron., 44, 317

Udalski A., Szymanski M., Kaluzny J., Kubiak M., Krzeminski W., Mateo M., Preston G. W., Paczynski B., 1993, Acta Astron., 43, 289

Udalski A., Szymanski M., Kaluzny J., Kubiak M., Mateo M., 1992, Acta Astron., 42, 253

Udalski A., Szymanski M., Kubiak M., Pietrzynski G., Wozniak P., Zebrun K., 1998, Acta Astron., 48, 147

Udalski A., Szymański M. K., Szymański G., 2015, Acta Astron., 65, 1

van den Berg M., Stassun K. G., Verbunt F., Mathieu R. D., 2002, A&A, 382, 888

van Leeuwen F., 2009, A&A, 497, 209

van Saders J. L., Gaudi B. S., 2011, ApJ, 729, 63

Watson C. L., 2006, Society for Astronomical Sciences Annual Symposium, 25, 47

Weber M., Granzer T., Strassmeier K. G., 2012, in Society of Photo-Optical Instrumentation Engineers (SPIE) Conference Series, Vol. 8451, Society of Photo-Optical Instrumentation Engineers (SPIE) Conference Series, p. 0

Wolszczan A., Frail D. A., 1992, Nature, 355, 145

Yadav R. K. S. et al., 2008, A&A, 484, 609

Yakut K. et al., 2009, A&A, 503, 165

Zechmeister M., Kürster M., 2009, A&A, 496, 577

Zhao J. L., Tian K. P., Pan R. S., He Y. P., Shi H. M., 1993, A&AS, 100, 243